

VIBRATION ISOLATION ACTIVE CONTROL TECHNIQUES AND TESTING IN A
MICRO-GRAVITY ENVIRONMENT

By

Jason Boulet

B.Sc.E.E. University of Manitoba, 1994

A THESIS SUBMITTED IN PARTIAL FULFILLMENT OF
THE REQUIREMENTS FOR THE DEGREE OF
MASTER OF APPLIED SCIENCE

in

THE FACULTY OF GRADUATE STUDIES
ELECTRICAL ENGINEERING

We accept this thesis as conforming
to the required standard

THE UNIVERSITY OF BRITISH COLUMBIA

April 1997

© Jason Boulet, 1997.

In presenting this thesis in partial fulfilment of the requirements for an advanced degree at the University of British Columbia, I agree that the Library shall make it freely available for reference and study. I further agree that permission for extensive copying of this thesis for scholarly purposes may be granted by the head of my department or by his or her representatives. It is understood that copying or publication of this thesis for financial gain shall not be allowed without my written permission.

Electrical Engineering
The University of British Columbia
2075 Wesbrook Place
Vancouver, Canada
V6T 1W5

Date:

April 29/1997

Abstract

Since orbiting space stations do not provide a perfect micro-gravity environment, vibration isolation techniques must be employed for sensitive experiments, such as crystal growing. A non-contact approach using magnetic levitation for active vibration isolation has been developed previously that can be used in all micro-gravity situations. Using advanced controller techniques, it should be possible to lower the stiffness of the magnetic coupling below levels achievable by PID control.

This thesis examines controlling magnetic levitation (MAGLEV) for improved vibration isolation on Earth and in a micro-gravity environment. Lorentz forces are used to levitate a large platform holding the application in an experimental system using this MAGLEV technology. This technology is described and two designs of its application are presented. Vibration control techniques are investigated, with H_∞ and Q -parameterization algorithms explained and employed in active control in a normal gravity environment. A smaller magnetically levitated wrist device is then described and employed in a coarse-fine approach to isolating acceleration disturbances in the micro-gravity environment provided by NASA's DC-9 performing parabolic flights. Results of the testing done on the flight is given and analyzed.

Table of Contents

Abstract	ii
List of Figures	vii
Acknowledgments	x
1 Introduction	1
1.1 Vibration Isolation	1
1.2 Contact vs. Non-Contact	2
1.3 Control	4
1.4 Magnetic Levitation Large Motion Isolation Mount	6
1.5 Micro-Gravity Testing	6
1.5.1 Two Stage System	8
1.6 Thesis Overview	8
2 Motion Isolation Mount Modeling	10
2.1 MAGLEV LMIM	10
2.1.1 Actuation	12
2.1.2 Sensing	13
2.2 Model	14
2.3 Effect of Filters	17
2.4 Destabilizing Feedback	19
2.5 Plant Identification $Y(s)$	23

2.5.1	Position Plant	24
2.5.2	Acceleration Plant	29
3	H_∞ Controller	33
3.1	Design Objectives	33
3.2	Theory	34
3.2.1	Plant and Design	34
3.2.2	Weights	37
3.2.3	Restrictions	37
3.2.4	γ -Optimization	38
3.2.5	SISO Simplification	39
3.3	Position Controller	40
3.3.1	Weight Selection	40
3.3.2	Simple Plant	42
3.3.3	Destabilizing Feedback	44
3.3.4	MATLAB Code	47
3.3.5	Implementation	47
3.3.6	Impulse Response	49
3.3.7	The Sensitivity Problem	49
3.4	Acceleration Feedback	51
3.4.1	Controller Design Considerations	52
3.4.2	Acceleration Controller	57
3.4.3	Force Rejection	61
3.4.4	Acceleration Controller Implementation	61
3.5	Conclusions	61

4	The Coarse-Fine System	64
4.1	Hardware and Software	64
4.1.1	Hardware	64
4.1.2	Software	66
4.2	Model Development	67
4.3	Open Loop System Analysis	71
4.4	Closed Loop System Analysis	72
4.5	Simulink Simulations	74
5	Micro-Gravity Testing	79
5.1	Installation and Testing	79
5.2	Results	81
5.3	Analysis	83
5.4	Recommendations for Future Study	86
6	Conclusions	89
	Bibliography	91
A	H_{∞} Theory Notes	95
A.1	Augmented Plant	95
A.2	Stabilizable and Detectable	96
A.3	Plant Transformations	96
A.3.1	Axis Shifting	96
A.3.2	Bilinear Transform	97
B	Nomenclature	99

C	H_∞ Controller Design Code	102
C.1	Main design file: design.m	102
C.2	Position weight generation: weights_x.m	104
C.3	Acceleration weight generation: weights_a.m	105
C.4	Bilinear transform: hinf_bilin.m	105
C.5	State space system: msys.m	106
C.6	Plotting summary: pltsum.m	106
D	Coarse-Fine Tracker Software Particulars	109
D.1	Coarse-Fine Software Algorithm	109
D.2	Coarse Stage Control Signal	112
D.3	Coarse Stage Code Variables	112
E	Data Plots	114

List of Figures

2.1	Simple schematic of the MAGLEV LMIM system.	11
2.2	Freebody diagram of one DOF of the LMIM.	12
2.3	A simple representation of the LMIM platform.	15
2.4	Bode plot of double integrator plant $G(s) = \frac{1}{ms^2}$	18
2.5	Simple LMIM model.	18
2.6	Effect of filters.	20
2.7	Effect of filters.	21
2.8	Model of plant with unstable feedback.	22
2.9	Bode plot of position plant with unstable feedback of 500 N/m.	22
2.10	Closed loop system used for plant identification.	23
2.11	Spectral analysis of position plant.	25
2.12	Position plant identification.	28
2.13	Bode plot of $Y_p(s)$	29
2.14	Spectral analysis of acceleration plant.	30
2.15	Acceleration plant identification.	32
3.16	The classic feedback loop for control systems.	34
3.17	The unique model representation for H_∞ control theory.	35
3.18	Standard form for the H_∞ control problem.	35
3.19	The position of the weights in the classic feedback model.	37
3.20	Augmented Plant.	41
3.21	Model for H_∞ design - simple double integrator plant.	43

3.22	H_∞ controller	45
3.23	Characteristics of the designed system with unstable force feedback.	46
3.24	Theory and data comparison.	48
3.25	Plot to evaluate the area of the sensitivity function.	50
3.26	The acceleration plant with an inner closed-loop position feedback.	53
3.27	Bode plot for acceleration plant $G_{ax}(s)$	54
3.28	General shape of the weights for acceleration controller design.	55
3.29	The complete position plant with acceleration feedback.	56
3.30	A position transfer function with acceleration feedback.	59
3.31	Position transfer function with acceleration feedback.	60
3.32	Force disturbance rejection	62
4.33	Diagram of the 1 DOF coarse-fine tracker.	65
4.34	Freebody diagram of the coarse fine coupled system.	67
4.35	Nyquist plots showing open loop stability of the system to airplane vibrations.	73
4.36	Bode plots showing closed loop response of the system to airplane vibrations.	74
4.37	Model of the coarse-fine control system.	75
4.38	Plots showing the simulation response to a sample vibration signal with $K_p = 1200, K_v = 15$	77
4.39	Plots showing the simulation response to a sample vibration signal with $K_p = 1200, K_v = 0$	78
5.40	Typical parabola cycle.	80
5.41	Simulation compared to actual data.	82
5.42	Data plots for a parabola.	84

5.43 Comparison of data and simulation with low frequency mode for the timing belt and static friction for the sliding car.	87
A.44 Special form of the bilinear transform that maps the jw -axis to a circle.	98
B.45 Closed loop position system with acceleration feedback.	99
D.46 State switching algorithm	111
E.47 Parabolic data plot 1.	115
E.48 Parabolic data plot 2.	116
E.49 Parabolic data plot 3.	117
E.50 Parabolic data plot 4.	118
E.51 Parabolic data plot 5.	119
E.52 Parabolic data plot 6.	120
E.53 Parabolic data plot 7.	121
E.54 Parabolic data plot 8.	122

Acknowledgments

I wish to extend my gratitude to many individuals who assisted me over the course of my research here at the University of British Columbia. First I would like to thank Tim Salcudean for his guidance during my project and for introducing me to this exciting field and interesting technology he has developed. I am greatly appreciative to him for the opportunity to ride the DC-9 in Cleveland, which was the experience of a lifetime. I would also like to thank Niall Parker for all his help in setting up and coding the system and making my work so much easier. The people in Cleveland were very helpful as well, especially Bill Stewart and Bjarni Tryggvason of the Canadian Space Agency who gave up a good chunk of their time to assist me in overcoming some bugs with the hardware and software. I arrived in Vancouver knowing no one, and I thank all the peers and colleagues I met who gave me positive experiences and memories. And finally I thank my family, my Mom and Dad for being always supportive and always believing in my abilities, and my daughter Ashley for always bringing a smile to my face.

Chapter 1

Introduction

1.1 Vibration Isolation

Things vibrate and cause vibrations - it is a fact. Whether sitting in a car at the rail crossing as the freight train rumbles by or riding in an airplane while the engines cause the seat to “tingle”, vibrations are felt. Or to take an extreme example, doing a delicate experiment when suddenly the whole table moves as a mild earthquake shakes the area and ruins the work.

However vibrations affect life, there are certainly instances when it is preferred not to be concerned with them. That plane ride would be much better if the ride was smooth, and that experiment will have to be started all over again. Enter vibration isolation techniques. These are aimed at reducing the effects of the source (that which causes the vibrations) on the application (that which is sensitive to the vibrations).

In a normal gravity environment, vibration isolation is used in many applications. Scanning tunnel microscopy depends on reliable control of tip-to-sample distance and is degraded if noise is present. Other precise measuring applications require isolation from noise. In delicate fabrication and assembly procedures, reliable position and orientation is required. Vibration noise in normal environment can be quite large, with high power machines bolted to floors or large vehicles driving around.

Vibration isolation is important in micro-gravity experiments, such as crystal growth research and other chemical experiments. Vibrations cause disturbance motions, and

therefore disturbance accelerations. The purpose of micro-gravity is to have net accelerations on the experiment to be zero, and vibrations degrade this result. This has become a large concern for orbiting laboratories and needs to be addressed. Two places to achieve a micro-gravity environment are in orbit and in a plane performing parabolic flights. In both cases, high frequency vibration is caused by the engines and other disturbances are caused by the movement of personnel in the craft.

There are two types of control available: passive and active. Passive techniques have been used extensively in many applications utilizing fluidics and dampers and springs. Active techniques are newer and include vibration cancellation and feed forward designs.

Cancellation is the method by which the vibrations from the source are countered before getting to the ambient surroundings. This method works well for a large generator to be isolated from the factory floor. The success of cancellation depends on the knowledge of the vibrations caused by the source, whether by design or measurement, and tends to be less successful for random vibrations (noise). [6] makes use of the idea that the best way to reduce ground vibrations is to not let it get to ground in the first place. The authors mount vibration causing equipment (motors, circular saws) on rigid supports with electro-hydraulic servo mechanisms. The vibrations of the isolated system are measured and fed-forward to a controller that has been determined in a parameter optimization-like procedure.

1.2 Contact vs. Non-Contact

The term *contact* is used to express the idea that the application is attached in some way to the ambient surroundings by some sort of rigid support - table legs, shock absorbers, and the like. It is reasonable to expect that the application be mechanically linked to the ground in this manner and many people have investigated isolation using this set up.

The use of a Stewart Platform is investigated in [9]. The Stewart Platform used is an innovative design and the authors look specifically at the 6 degree of freedom case. By controlling the hydraulics of the system in a specific manner, a spring-damper connection to the ground is achieved to attenuate vibrations.

A method to rigidly mount the experimental platform to a space structure is presented in [5]. The legs of the platform are connected to the hull of the lab through piezo-ceramic mounts, which contract and expand with electric currents. The amount of movement is very limited and the piezo-ceramic materials might be subject to breakage.

Of course the biggest problem with any contact system is exactly that - it is actually touching the ambient surroundings and therefore some vibrations are bound to be transmitted to the application. The best solution would be a non-contact system - one that does not physically touch the surroundings at all, except perhaps through an umbilical cord that supplies power and measurements to a controller. Since the application is not in contact with the surroundings, only its own vibrations affect it. A simple analogy would be flying in a plane during an earthquake.

[4] takes this idea to the extreme and proposes that the application (an experiment platform) be free floating. This assumes that the isolation system be located in space of course. An umbilical cord must be attached between the platform and hull for power and measurements and such, but otherwise the system is completely isolated. However, due to trajectory changes and corrections, the platform is bound to not stay centered in the research space. The authors address this with the use of air jets to keep the platform centered. They are careful to find the range of linear force for the air jets. This system has limited application on the ground and also limited centering control.

An option that works for earth based systems as well as micro-gravity is magnetic levitation, and much has been reported on its use in various applications, mostly in transportation. Levitated car seats and levitated high velocity trains are some of the

ideas for levitation. It can also be used in vibration isolation to gain some of the benefits of a non-contact system while allowing better control than the complete non-contact system; [11] uses magnetic bearing levitation for fine vibration isolation. There is still no direct contact, but better control can be achieved. The platform is levitated above a Stewart platform which controls the coarse motion of the platform. The platform controller tends to return to the center of the Stewart platform, which in turn tends to the center of the research space.

This idea is expanded in [15], which looks at optimizing the hardware for ease of controller design. Given the properties of the plate levitated by magnetic bearings, the paper looks into determining the best position and number of sensors and actuators required. Theorems supporting their results plus the instability of magnetic bearings are presented, and addresses very briefly the magnetic non-linearity.

A system closer in design to what is presently being worked with is given in [8] - the magnetic levitation is different than in previous papers. The platform is levitated on a coarse motion stage (a robot arm) attached to the wall of the craft which tends to the center of the space. The actuator and sensor locations are fixed so hardware optimization is not possible. The platform remains unconnected to the surroundings and can be moved large displacements (slowly) with the coarse stage while the fine stage levitation isolates the platform from the entire system.

1.3 Control

After hardware has been chosen, a controller must be designed. Some papers are hardware non-specific and show the effect popular control algorithms on the vibration isolation problem. These designs assume linear plants and knowledge of system dynamics for the most part. PD or PID control can be used, but other techniques can be used to improve

the system response.

[7] compares two types of active control - the usual cooperative optimization technique *vs.* the authors' non-cooperative technique. A numerical example is provided for a simple plant and indicates that the non-cooperative technique has better isolation while remaining just as robust as the cooperative technique.

Another paper of note is [10] which actively controls vibrations by cancelling the vibration nodes of the system. This of course requires knowledge of the vibration nodes before design. Another controller examined is one designed by using LQG theory. Simulations of these are also positive.

A general control scheme for linear forces is presented in [12]. Using a quadratic performance index, a robust controller is designed based on one of five possible representations of the system. The controller has an LQR feedback loop and a constant gain feedforward loop.

An LQG controller which is designed based on the predicted disturbances of the system and also depends on knowledge of the response of the flexible structure to the vibrations is employed in [5] to control the electric currents for the piezo-ceramic mounts.

The system to be used may be non-linear and attempts can be made to linearize it. [19] directly addresses the magnetic non-linearity by putting a feedback PD loop around the actuator. [18] uses this tool to remove the negative stiffness of their novel actuator for their isolation technique. With the accelerometers on the base of the system, the authors use PID as their control algorithm. The gains are adjustable, and are changed until the desired response is obtained.

A lot of the controllers depend on knowledge of the system dynamics and vibration nodes that exist. One option is as in [9] where the authors use adaptive control since the specific dynamics of the system are unknown, plus the controller then becomes much more flexible in possible applications.

1.4 Magnetic Levitation Large Motion Isolation Mount

The Large Motion Isolation Mount uses magnetic levitation technology (MAGLEV) [38] and is developed in [17], [14]. The hardware was designed and built under contract [29] [30] [31] at the University of British Columbia for the Canadian Space Agency. The CSA was looking to use long magnetic bearing rods for vibration isolation in space and approached Tim Salcudean. Dr. Salcudean suggested a coarse-fine approach to give the same workspace while using Lorentz forces to control the fine stage. In this approach, force is not proportional to the position.

A fine stage only design was sent up on the Space Station MIR and has provided vibration isolation reliably for over six months. The control for this MIM was provided by Tim Salcudean and Niall Parker after several control techniques were studied [16]. A PID controller yielded acceptable response controllers but it was thought other techniques would be better. Slotine and Li methods had slow convergence and a recursive least squares method did not converge satisfactorily at all. Q -parameter methods were investigated and found to have good responses and were easy to design.

1.5 Micro-Gravity Testing

There are two popular methods of simulating micro-gravity conditions in normal gravity. The first method of micro-gravity simulation is the use of a drop tower - a very tall structure with a padded vertical shaft that usually extends into the ground. The experiment is released from a drop tower where the experiment then accelerates toward a soft landing area. This method has excellent micro-gravity characteristics but has the disadvantage of the sudden stop at the end, which might not be desirable for some of the more delicate experiments.

The second and cheaper way to conduct micro-gravity experiments is to use an aircraft

performing parabolic flights, such as NASA Lewis Research Center's DC-9. The airplane follows a parabolic trajectory that gives a period of micro-gravity conditions. First the plane pulls up steeply, increasing the gravity to almost twice normal. Then the plane begins to decrease in pitch lowering the effect of the acceleration due to gravity on the plane. At the top of the parabola, as the pitch angle changes to negative, the occupants of the plane experience free fall conditions and continue to do so until the plane pulls up level with the horizon again. Further information on the flight can be obtained from NASA's DC-9 World Wide Web site at <http://zeta.lerc.nasa.gov/jpw/cover.htm> or [13].

Parabolic flights provide approximately 20 seconds of noisy micro-gravity. The noise comes in the form of high frequency vibrations caused by the aircraft engines and air turbulence and low frequency motion from trajectory errors and corrections. Due to this noise, to obtain a clean micro-gravity environment the experiment is usually conducted as a *free float*. A *free float* experiment is released by the experimenter during the zero gravity phase of the parabola and is allowed to drift around the aircraft until it hits the wall. This is not optimal because the motion of the free float is unconstrained and could be a hazard to other experiments, plus when releasing the experiment it is impossible not to impart initial conditions. Free floats are used because any experiment bolted to the aircraft frame experiences all the vibrations and noise that the frame does.

The noise problems associated with the parabolic flights can be rectified by using a magnetic levitation approach. A magnetically levitated platform will isolate the experiment from the high frequency vibrations and will slowly move the platform to the center of the rattle space to correct the low frequency errors. The platform is attached to the aircraft, so there will be some noise transmission to the experiment, but it will be considerably less than if no magnetic levitation was used.

One problem with free floats is uncontrollable initial conditions. With a magnetically levitated platform, initial conditions can be set to desired values.

1.5.1 Two Stage System

On the parabolic flights the low frequency errors are large in magnitude and will cause the platform to reach the limits of its workspace quickly if the control bandwidth is small. What is required, if the bandwidth of the platform is to be kept low, is for the stator to move as well. This means there are two systems working together to isolate the system: a coarse stage and a fine stage. The anticipated problem with this setup would be having two systems trying to work together while at the same time reacting against each other.

The fine stage is a version of the magnetically levitated platform and reduces high frequency noise. The coarse stage follows low frequency errors and would be a robot arm of some type, such as a six degree of freedom PUMA. Thus as the fine stage is left to drift freely, the coarse stage tracks the flotor, keeping it in the rattle space. See [38], [37], [36]. The motion of the coarse stage is limited by the workspace of the airplane, but the combined workspace will be much larger than the fine stage alone. Another benefit of the coarse-fine approach is the bandwidth of the fine stage can be lowered further since less centering force is required.

1.6 Thesis Overview

Vibrations are a problem that need to be considered. The goal is to have an isolation system that is effective against all disturbance vibrations, both high frequency and low frequency.

The system used in this thesis consists of two stages. A fine stage isolates the system from small high frequency disturbances and a coarse stage cancels large low frequency disturbances. This increases the workspace during isolation procedures. The two stage approach gives better isolation characteristics than a one stage system.

The fine stage uses magnetic levitation technology [17], which isolates the system from

high frequency disturbances, instead of cancelling disturbances. With the MAGLEV technology, a lower stiffness should be achievable. Other benefits of using Lorentz forces are the force is not proportional to position so the actuators are more linear, and there is no positioning backlash with the actuators. Actuator control is developed using H_∞ theory. This should provide better robustness in the presence of model uncertainties and provide good closed-loop shaping.

This thesis provides some background information on the MAGLEV system and develops H_∞ control theory for use on an actual MAGLEV apparatus. The effectiveness of the coarse-fine approach in a micro-gravity environment is evaluated using a one degree of freedom set-up tested on a DC-9 performing parabolic flights. A one degree of freedom system has less of the dynamic considerations necessary for a full six degree of freedom system and should prove the concept works.

The first chapter looks at the system to be used and explains how it works. Next H_∞ control theory is explained and used to attempt design of a robust controller that uses the available position data. Experimental data was studied to determine the success or failure of the system after the controller is tested in simulation. The next chapter explains the smaller version of the magnetically levitated platform and its coarse stage tracker. The system is modeled and simulated in the next chapter. The subsequent chapter describes the testing on the DC-9 and analyzes the data collected. The final chapter draws conclusions and presents ideas for future work.

Chapter 2

Motion Isolation Mount Modeling

This chapter looks at the Large Motion Isolation Mount used in normal gravity. A description of the system is presented, including a brief overview of the hardware. The system is modeled as a rigid body and the development of this model is presented. Some plant identification is performed and the benefits of using different plants is discussed.

2.1 MAGLEV LMIM

The Large Motion Isolation Mount (LMIM) is a hardware intensive system, and a simple schematic is shown in Figure 2.1. A magnetically levitated (MAGLEV) system has two distinct parts: the *flotor* and the *stator*. The *flotor* is called flotor because it is levitated, or floats, above the base. In the case of the LMIM, the flotor weighs 22 kg. The *stator* is the base of the system. The only connection between the flotor and stator is an umbilical cord that provides power for the flotor sensing devices and transmits the signal data from these devices. A one degree of freedom freebody diagram of the system is presented in Figure 2.2. The actuator couples the flotor and stator, with the actuator applying f_{act} to the flotor. The umbilical cord physically couples the flotor to the stator, and its force effect is included in f_{dist} . The vibrations that act on the stator are those from which the flotor is to be isolated.

The main actuation and sensing components are shown in Figure 2.1.

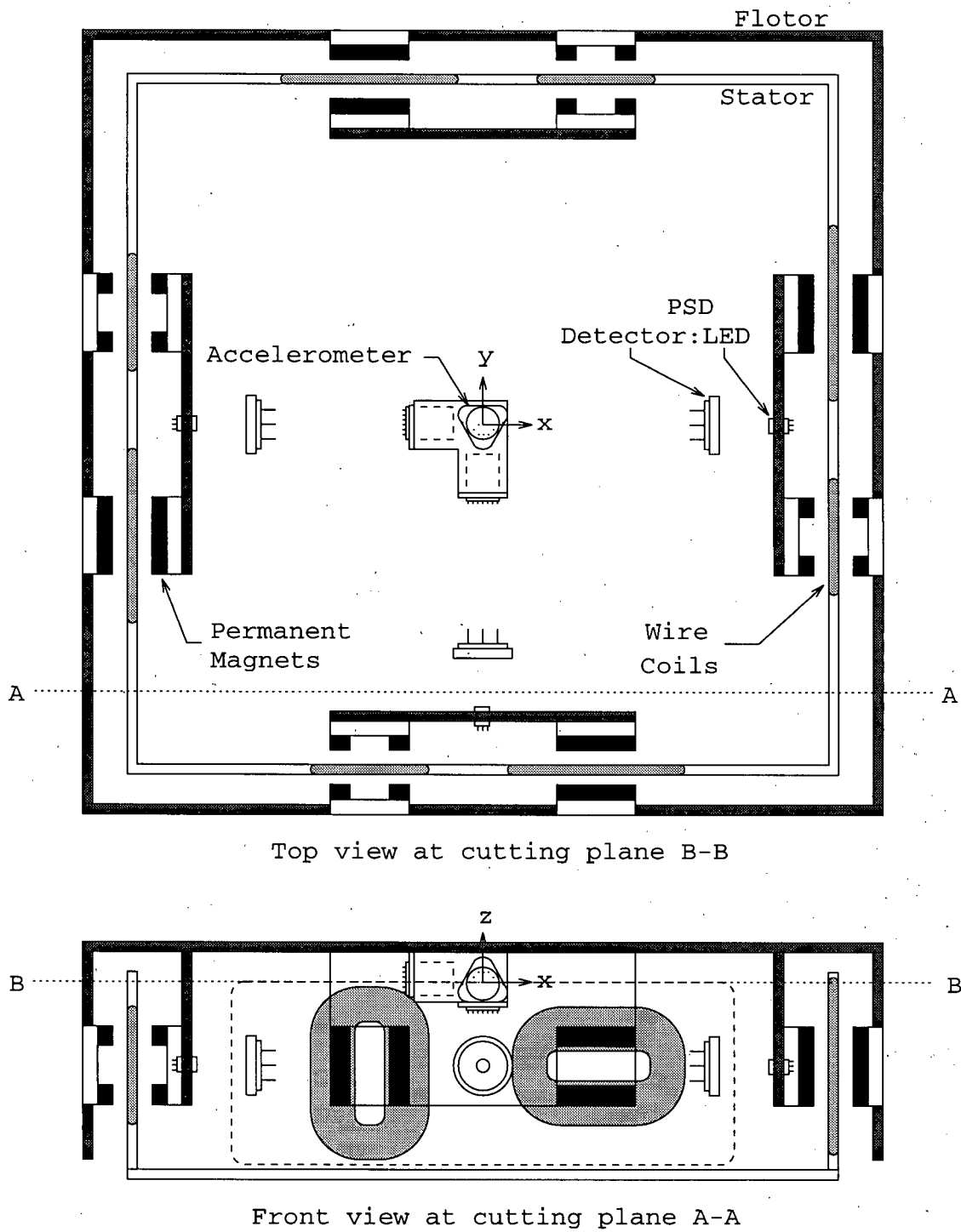


Figure 2.1: Simple schematic of the MAGLEV LMIM system.

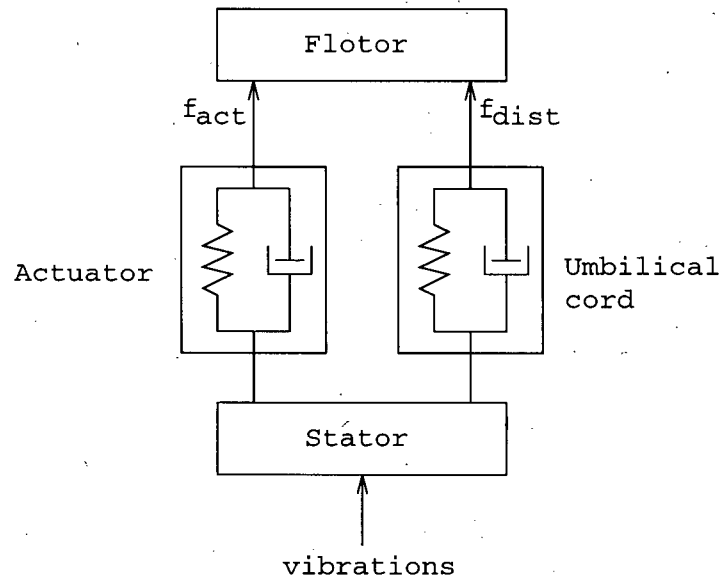


Figure 2.2: Freebody diagram of one DOF of the LMIM.

2.1.1 Actuation

The flotor has eight pairs of permanent magnets in a square configuration that create the magnetic field necessary for operation. The stator has eight wire coils, each one fitting between a pair of the permanent magnets on the flotor.

Lorentz forces are used to levitate the flotor above the stator by controlling a current through the wire coils in the stator in the magnetic field produced by the magnets in the flotor. The force is

$$\mathbf{F} = I \int_L (d\mathbf{l} \times \mathbf{B}) \quad (2.1)$$

where I is the current through the coil, \mathbf{B} is the magnetic field produced by the magnets and $d\mathbf{l}$ is a differential length of wire in the direction of the current. Lorentz levitation has the benefit of frictionless motion with no backlash, so it is ideal for fine positioning applications. The advantage for vibration isolation is instead of actively cancelling high frequency noise, as is the case for contact technology, magnetic levitation cannot follow the high frequency noise above the system bandwidth. This is an advantage because it

should allow the bandwidth to be decreased significantly resulting in a lower stiffness coupling which will isolate better against noise.

Using Lorentz forces also creates problems. The magnetic field strength is not constant over the entire space between the permanent magnets. Non-linearities grow as the gap between the magnets increases - the flux *fringes* to a greater extent - and the magnetic field weakens. This then becomes a tradeoff between flotor motion range (rattle space) and controllability. The flotor can only move as much as the gap between its magnets so a larger gap means a greater rattle space, but also means less linearity for control.

The LMIM has a gap of ± 1.5 mm in the x direction and ± 2 mm in the y direction. Design specifications were for a ± 4 mm air gap, but sloppy tolerances on the flotor construction prevents it from achieving the full workspace.

2.1.2 Sensing

Position and orientation of the flotor is determined by Position Sensing Diodes (PSD). Three narrow beam LED's on the flotor project onto a detector attached to the stator. The hardware, calibration, and signal conditioning for the PSD's is given in [39], and the matrix manipulations required to give flotor position and orientation are supplied in [33]. The acceleration of the flotor and stator in each of the axes x , y , and z are measured by accelerometers.

The signals are conditioned by Butterworth filters located in the stator. The filters are low pass with cut off frequency at 100 Hz. The acceleration filters are second order and the position filters are fourth order.

2.2 Model

The LMIM is obviously a very complicated system with many different components. To obtain a model that will be easy to work with some assumptions are made.

First, it is assumed the flotor behaves as a rigid body and any flexible modes are either small or high enough in frequency to be negligible. This allows the flotor to be represented as a simple rigid body.

The actuators, as mentioned earlier, are non-linear. The transformation from currents to wrenches is location-dependent and there will be some eddy current coupling. For the actuator model, linearity and negligible eddy currents are assumed.

The sensors have a very high resolution and are subject to small deformities. The slightest concave curvature of the sensor could push the flotor to the side and limit the lowest frequency available in normal gravity. All sensors are assumed to be linear.

The filters are assumed to be all identical and precise.

Using these assumptions, a model of the LMIM platform is shown in Figure 2.3. The sensed signals are position (x) and acceleration (a). The position vector has both translation and rotation components while the acceleration vector has only three translation components, as angular accelerations are not measured. In Figure 2.3, the wrench vector is applied to the flotor. I maps the six element wrench vector to three translational and three rotational acceleration elements and then $G(s)$ converts the accelerations to position elements. The force-torque transformation for a rigid body of a point not at the center of mass is

$$\bar{f} = m\ddot{o} + m\dot{\bar{w}} \times (\tilde{c} - \tilde{o}) + m(\bar{w} \times)^2(\tilde{c} - \tilde{o}) \quad (2.2)$$

$$\bar{\tau}_o = (\tilde{c} - \tilde{o}) \times m\ddot{o} + \bar{J}_o\dot{\bar{w}} + \bar{w} \times \bar{J}_o\bar{w} \quad (2.3)$$

where \bar{f} and $\bar{\tau}$ are the force and torque applied to the flotor, m and \bar{J} are the mass and

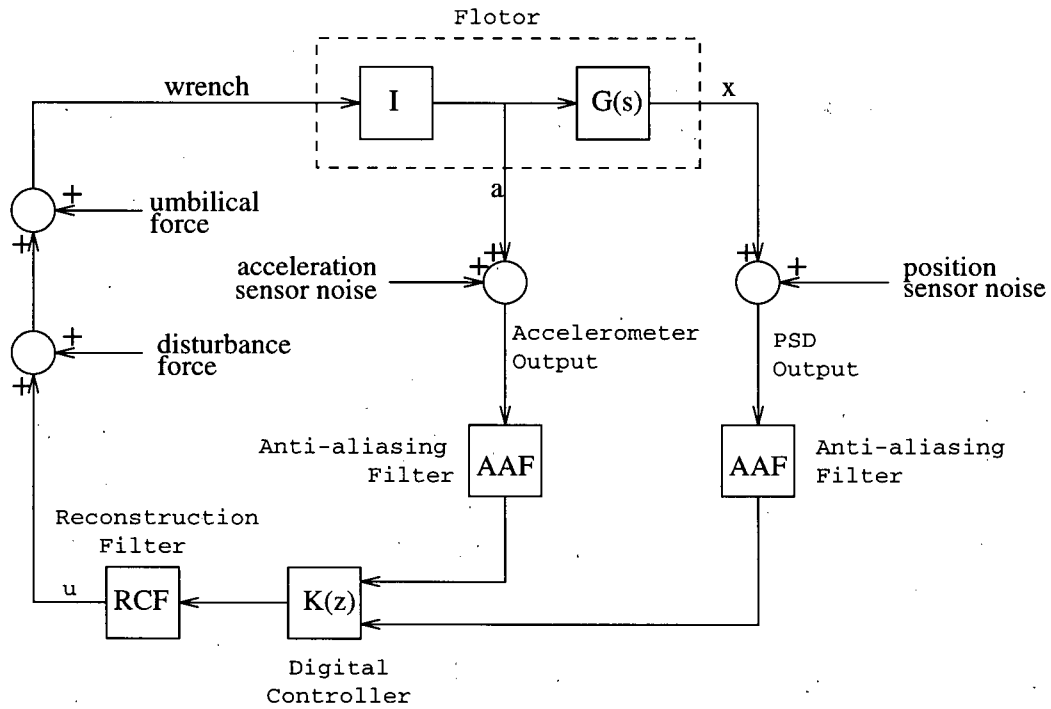


Figure 2.3: A simple representation of the LMIM platform.

inertia matrix, $\ddot{\tilde{o}}$ is the linear acceleration of the point, $\dot{\tilde{w}}$ is the angular acceleration, and \tilde{c} is the center of mass point. If we assume the second order terms are small, the quadratics can be neglected, giving

$$\bar{f} = m\ddot{\tilde{o}} + m\dot{\tilde{w}} \times (\tilde{c} - \tilde{o}) \quad (2.4)$$

$$\bar{\tau}_o = (\tilde{c} - \tilde{o}) \times m\ddot{\tilde{o}} + \bar{J}_{\tilde{o}}\dot{\tilde{w}}. \quad (2.5)$$

When the point is the center of mass,

$$\bar{\tau}_c = \bar{J}_{\tilde{c}}\dot{\tilde{w}}. \quad (2.6)$$

Applying the wrench

$$\begin{bmatrix} \bar{\tau}_{\tilde{f}} \\ \bar{f} \end{bmatrix} = \begin{bmatrix} \bar{\tau}_c + (\tilde{c} - \tilde{f}) \times \bar{f} \\ \bar{f} \end{bmatrix} \quad (2.7)$$

$$= \begin{bmatrix} \bar{J}_{\tilde{c}} \dot{\tilde{w}} + \bar{r}_{cf} \times (m \ddot{\tilde{o}} + m \dot{\tilde{w}} \times \bar{r}_{cf}) \\ m \ddot{\tilde{o}} + m \dot{\tilde{w}} \times \bar{r}_{cf} \end{bmatrix} \quad (2.8)$$

$$= \begin{bmatrix} \bar{J}_{\tilde{c}} \dot{\tilde{w}} + \bar{r}_{cf} \times m \ddot{\tilde{f}} \\ m \ddot{\tilde{f}} + m \dot{\tilde{w}} \times \bar{r}_{cf} \end{bmatrix} \quad (2.9)$$

$$(2.10)$$

we get the force-torque transformation

$$\begin{bmatrix} \bar{f} \\ \bar{\tau}_{\tilde{f}} \end{bmatrix} = \begin{bmatrix} mI & m\bar{r}_{cf} \times \\ m\bar{r}_{cf} \times & \bar{J}_{\tilde{c}} \end{bmatrix} \begin{bmatrix} \ddot{\tilde{f}} \\ \dot{\tilde{w}} \end{bmatrix} \quad (2.11)$$

where \bar{r}_{cf} is the vector from \tilde{c} to the center of the flotor \tilde{f} .

When the center of the flotor coincides with the sensor center and the center of mass, the diagonals of the force-torque transformation reduce to zero, and the matrix I is the inverse of this transformation

$$I = \begin{bmatrix} \frac{1}{m} I_3 & 0 \\ 0 & \bar{J}_{\tilde{c}}^{-1} \end{bmatrix} \quad (2.12)$$

where I_3 is the 3x3 identity matrix.

Continuing with Figure 2.3, $G(s)$ transforms the accelerations to position and is a 6x6 matrix of transfer functions. $K(z)$ models the digital controller plus the digital-to-analog and analog-to-digital converters. The response of the digital controller $K(z)$ approaches the response of the continuous controller $K(s)$ at sufficiently high sampling rate. The inputs to the computer are the three translational accelerations of the flotor with added accelerometer noise and the six element position and orientation of the flotor with added PSD noise. [1] identifies this noise to be white with magnitude of $2.5 \mu\text{m}$.

AAF is the anti-aliasing filter for the input signals. The signals are filtered by low pass Butterworth filters of cut off frequency 100 Hz and order four for position and order

two for acceleration. RCF is the reconstruction filter and is the filter for the output signal. The filter is a low pass fourth order Butterworth with cut off frequency 100 Hz. The AAF will also be referred to as the A/D filter, and the RCF will also be referred to as the DAC filter.

The output of the computer is conditioned by the DAC filter and is the six element wrench command. This wrench command is affected by any disturbance forces such as changing acceleration levels and the umbilical force. The umbilical cord acts as a spring-damper connection with positive spring constant between the flotor and stator and the umbilical force is dependent on the position of the flotor.

This six degree of freedom model is very cumbersome with large matrices and six element vectors. For ease of controller design, the model will be reduced to a one degree of freedom approximation using the afore mentioned assumptions and assuming all degrees of freedom behave identically. The rotational elements are ignored and the design will be done for an axis in the horizontal plane so the force due to gravity does not need to be considered.

In one degree of motion, the mass transform I is $\frac{1}{m}$ and $G(s)$ is $\frac{1}{s^2}$. This model is shown in Figure 2.5 and the Bode plot of $\frac{1}{ms^2}$ is shown in Figure 2.4. $K(s)$ is made up of two controllers, position ($C_p(s)$) and acceleration ($C_a(s)$).

2.3 Effect of Filters

Figure 2.5 shows a model with the conversion filters and the plant as simply $\frac{1}{ms^2}$. The model would be of much lower order if the filters could be disregarded, since the filters are up to fourth order. The effect of the filters near the bandwidth must be investigated.

A simple test can be done to determine if the filters need to be included in the model.

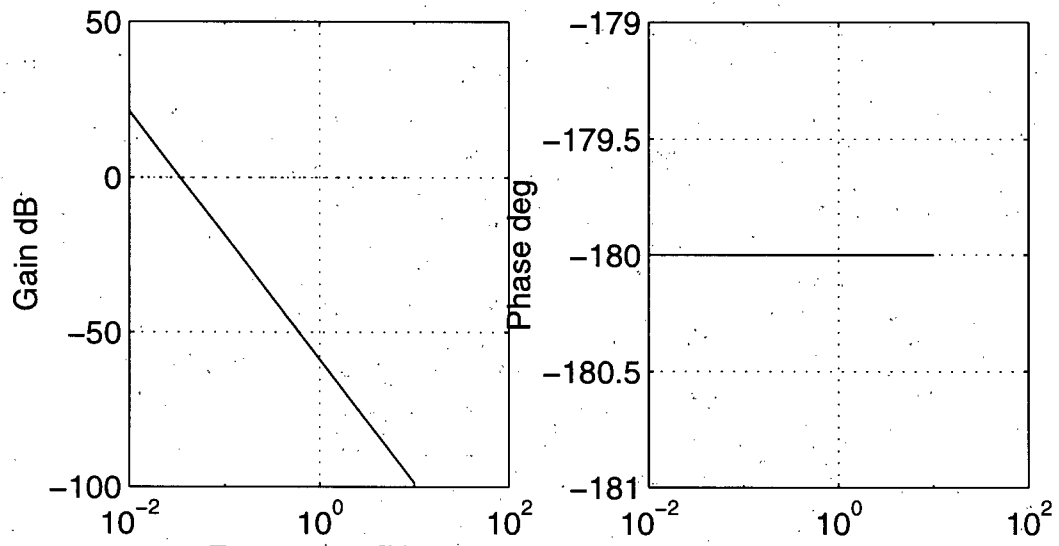


Figure 2.4: Bode plot of double integrator plant $G(s) = \frac{1}{ms^2}$.

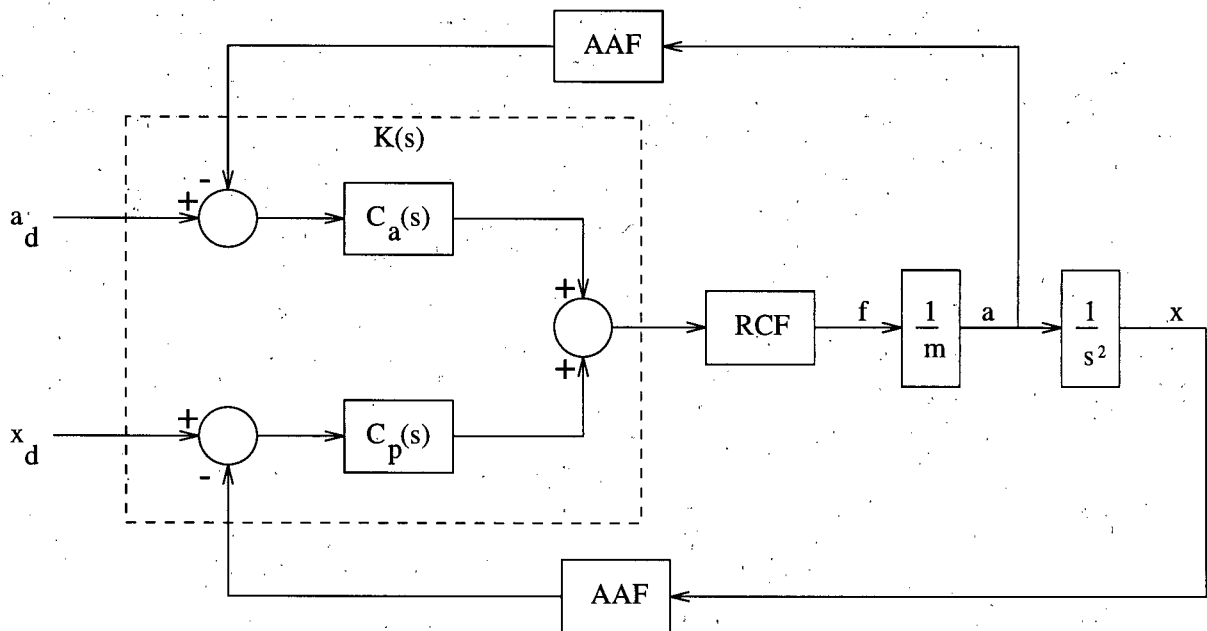


Figure 2.5: Simple LMIM model.

Using a simple PD controller to force the closed loop response bandwidth to be around 10 Hz (very high), the difference in response with different filters can be determined. Figure 2.6 shows the effect on the system for a second order reconstruction filter at 30 Hz and a fourth order anti-aliasing filter at 250 Hz. The effect of the reconstruction filter is the most pronounced and alters the system by creating a 6 dB resonant peak. Figure 2.7 changes the filters slightly to fourth order at 100 Hz for the RCF and fourth order at 200 Hz for the AAF. The effect of these filters are insubstantial at this bandwidth, so as long as the filter bandwidth is large enough, at least 100 Hz, and the bandwidth of the closed-loop system is less than 10 Hz, the filters can be ignored in the model.

2.4 Destabilizing Feedback

There is a destabilizing force on the flotor that varies as a function of position, similar to an inverted pendulum [28]. An increasing force causes the flotor to reach the edge of the workspace, and the controller is not able to counter this force. There are two probable causes of this - actuator non-linearity and PSD detector curvature. Since the flotor tends to go to one side more often, it is likely PSD detector curvature causes the position measurement center to not coincide with the center of the magnetic gap. And once off-center, the inverted pendulum effect occurs.

Figure 2.8 is a model of this actuator non-linearity. $K(s)$ is the controller, and the new plant $G_p(s)$ is

$$G_p(s) = \frac{1}{ms^2 - H} \quad (2.13)$$

where m is the mass of the flotor and H is the positive linear force feedback. The Bode plot of this transfer function is shown in Figure 2.9.

A value for H was determined indirectly. Initial measurements were done with a force meter. A more accurate method involved changing the steady state force acting on the

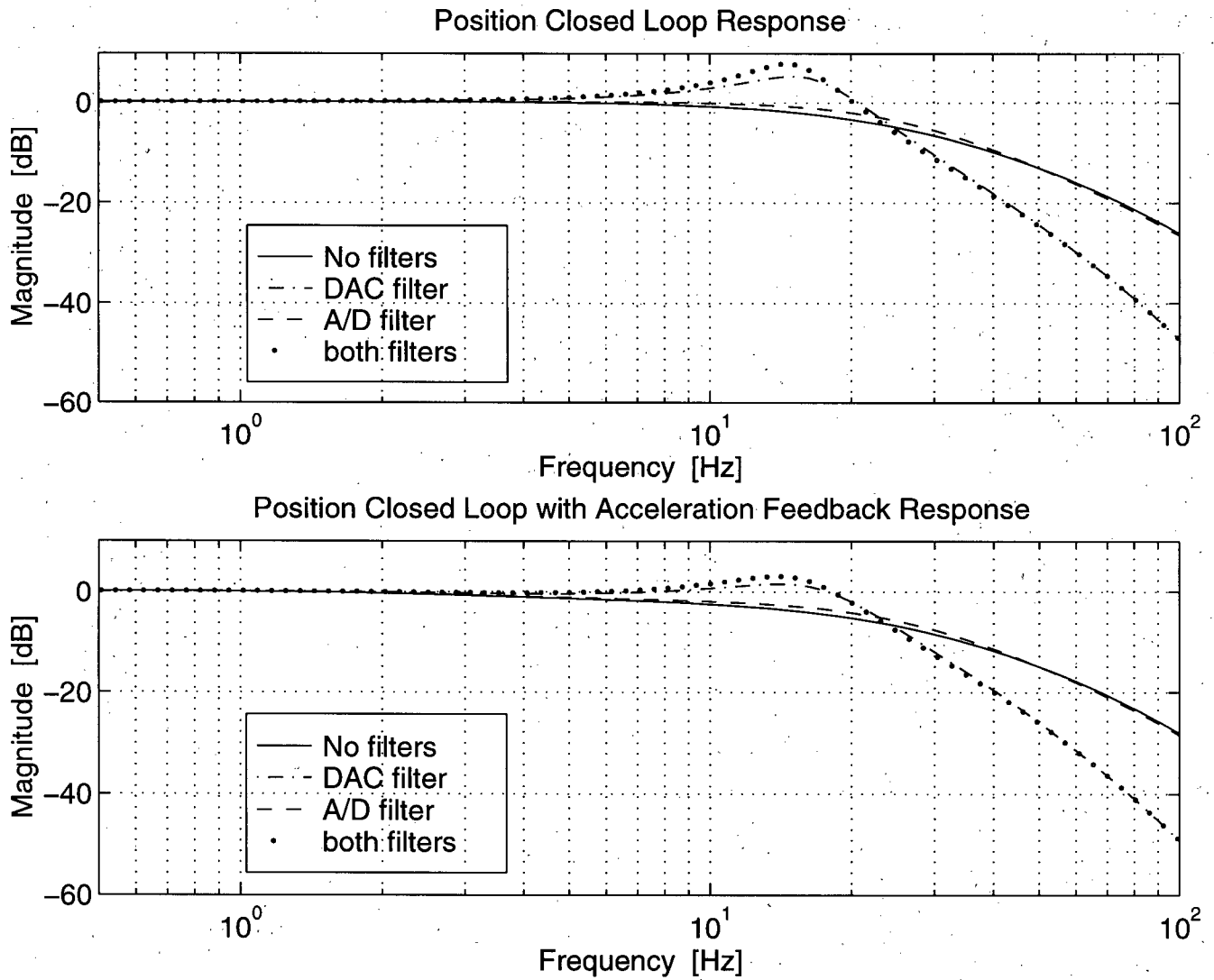


Figure 2.6: Effect of filters on closed loop system under PD control. Second order reconstruction filter at 30 Hz and fourth order anti-aliasing filter at 250 Hz.

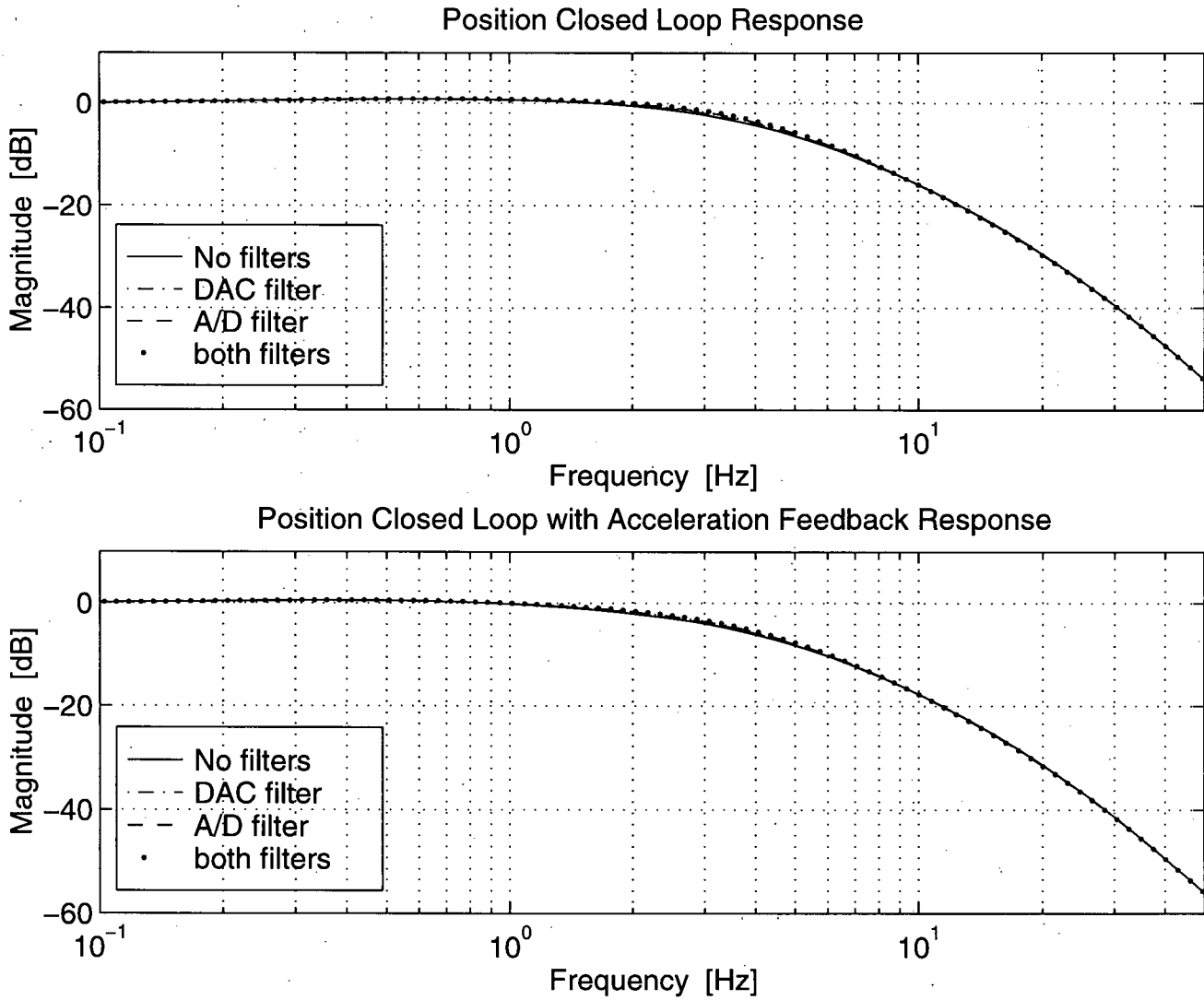


Figure 2.7: Effect of filters on closed loop system under PD control. Fourth order reconstruction filter at 100 Hz and fourth order anti-aliasing filter at 200 Hz.

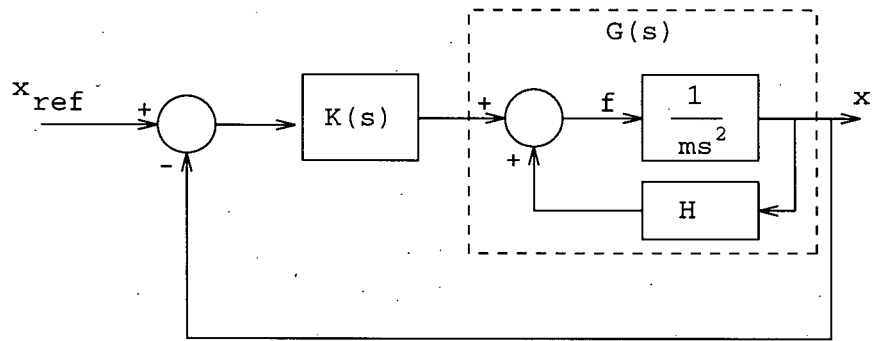


Figure 2.8: Model of plant with unstable feedback.

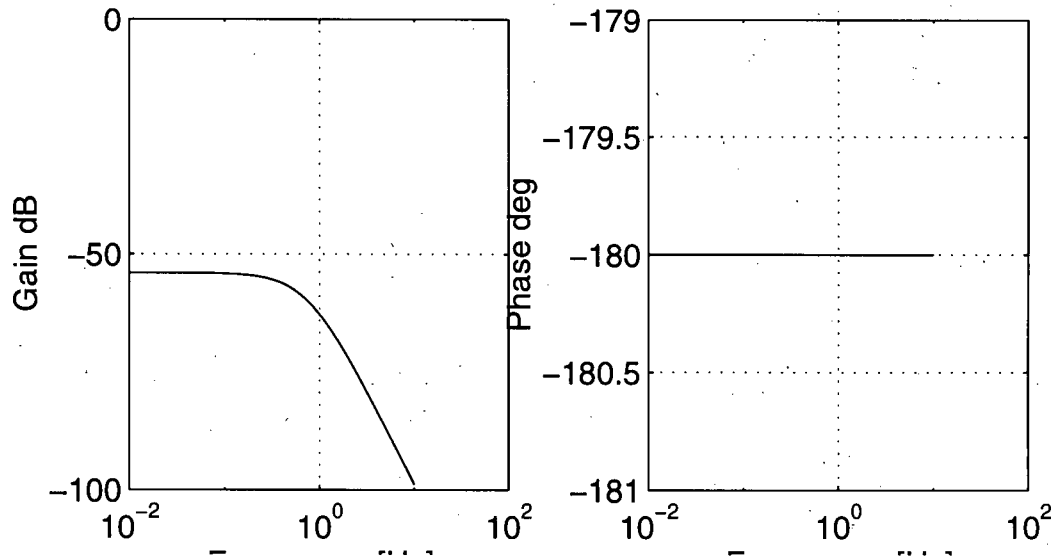


Figure 2.9: Bode plot of position plant with unstable feedback of 500 N/m.

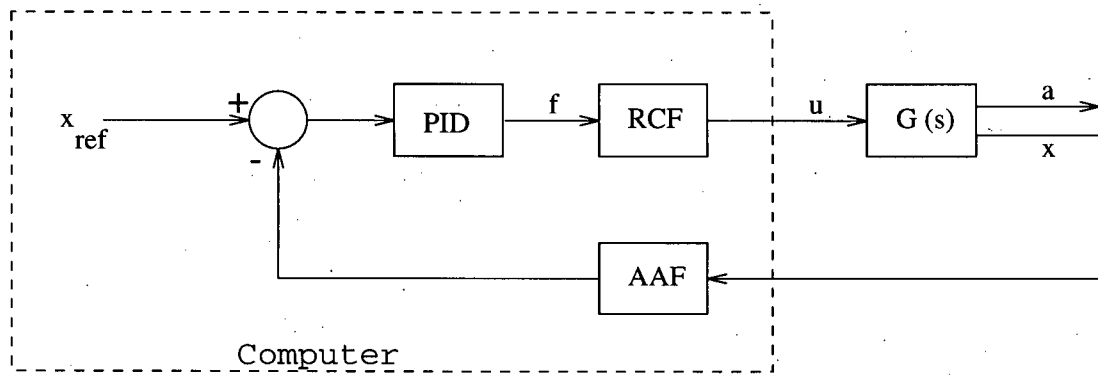


Figure 2.10: Closed loop system used for plant identification.

flotor when the controller stiffness was too low to center the flotor. The steady state force was increased from zero until the flotor moved off the edge of the work space and hit the other side. The strength of the force required to move the flotor away from the edge of the workspace was approximately 0.5 N. With workspace limit of about 1.5 mm, H becomes 333 N/m.

The expression “falls to the side” may be used in discussion of the LMIM. The instability comes from the position and force non-linearity of the system and amounts to an inverted pendulum mode [28]. When the flotor is centered any displacement will add increasing force and the flotor will hit the edge of the workspace, as an inverted pendulum that is displaced will fall due to the force of gravity. Thus the term “falls to the side”.

2.5 Plant Identification $Y(s)$

In an attempt to get a more accurate model some simple identification was performed. Figure 2.10 is the closed loop system used and defines the unknown plant from the RCF output u to position and acceleration to be $G(s)$. The controller is simple proportional-plus-integral-plus-derivative and stabilizes the flotor in the workspace with no exceptional isolation characteristics. The output of the PID controller is f and is more readily

available than u . As a consequence, the plant that will be identified is $G(s)$ plus the reconstruction Butterworth filters. This plant will be called $Y(s)$ and is

$$\begin{bmatrix} a \\ x \end{bmatrix} = Y(s) f \quad (2.14)$$

$$\begin{bmatrix} a \\ x \end{bmatrix} = \begin{bmatrix} Y_a(s) \\ Y_p(s) \end{bmatrix} f. \quad (2.15)$$

Ideally, to get a good measure of the output response of a system, the input signal is white noise. It is not possible to set f to this because the system would be open loop and unstable. Instead, x_{ref} is driven by an approximation of white noise which results in a noisy signal f as the PID controller attempts to follow the reference position. By performing spectral analyses on f to x and a , the plant can be approximated.

Data signals f , x , and a were collected for 30 minutes as the flotor position was driven by the noise. More data points give better representation of all frequencies and a better spectral analysis.

2.5.1 Position Plant

The analysis of the force and position data is shown in Figure 2.11. The first plot shows the power spectral density of the Control Input to the plant and the second shows the power spectral density of the Flotor Position. Note the units are inconsistent. Based on these power spectral densities the transfer function from f to x is represented graphically in the *Tf fcn mag* plot of Figure 2.11. The coherence of this transfer function is shown in the last plot and shows confidence between 0.2 Hz and 10 Hz:

Coherence is a measure of the correlation between the input signal and the output signal, and has a value between one and zero. A coherence of one indicates that the signals are a linear transformation of each other, and a low coherence indicates non-linear

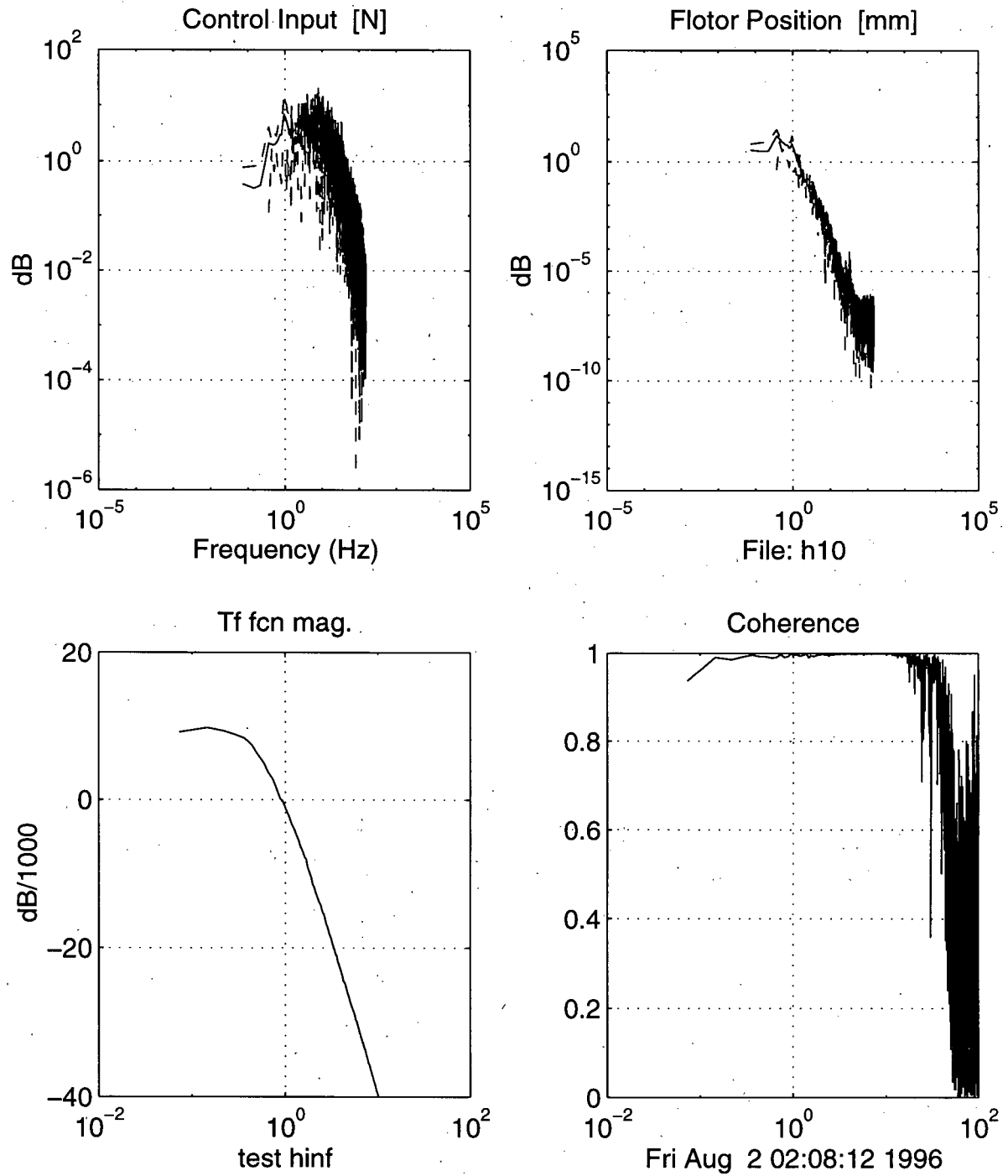


Figure 2.11: Spectral analysis of controller output to flotor position. The Control Input is f , the Flotor Position is x , and the Tf fcn mag is $\frac{\hat{x}}{\hat{f}}$.

terms and noise in the output signal.

The next step in this simple identification attempt is to fit a transfer function in the Laplace domain to the shape shown in the *Tf fcn mag* plot of Figure 2.11. The low frequency gain of *Tf fcn mag* appears to be constant near 9 dB, keeping in mind position units are mm. The DC response is approximately

$$|Y_p(2\pi f)| \approx 2.6, f < 0.1. \quad (2.16)$$

After the roll off the data plot has a slope of -40 dB/decade for a time. As the frequency increases past 9 or 10 Hz, the plot rolls off at a greater rate. The new rate cannot be determined due to the bad coherence of the data past 10 Hz. The first part of the roll off can be expressed as

$$|Y_p(2\pi f)| \approx \frac{45}{(2\pi f)^2}, 2 < f < 9 \quad (2.17)$$

and then the denominator order increases.

Although the phase of the transfer function is not plotted separately, it can be seen in Figure 2.12. In this instance, the phase starts at -180° and increases slightly to -170° before decreasing at 1 Hz. The low frequency phase being negative with a constant magnitude gain implies a right half plane pole, and the slight increase in phase is indicative of a small positive damping in a second order function.

Using these points, the transfer function $Y_p(s)$ is at least third order in the denominator and zero order in the numerator. For this simple identification, the denominator will be chosen as third order with a first order and a second order factor. The second order factor is chosen because of the damping required to fit the phase data. The general form for the transfer function between f and x is defined as

$$Y_p(s) = \frac{\alpha w_1^2}{\left(\frac{s}{w_2} + 1\right)(s^2 + 2\zeta w_1 s - w_1^2)} \quad (2.18)$$

where α is the DC gain, w_1 is the first corner frequency, w_2 is the second corner frequency, and ζ is the damping ratio of the plant. Both frequencies w_i are in rad/s. From (2.16)

$$Y_p(0) = \alpha = 2.6 \quad (2.19)$$

and from (2.17)

$$\alpha w_1^2 = 45 \rightarrow w_1 \approx 4.16. \quad (2.20)$$

After iterating the values of ζ from 0.05 to 0.5 and w_2 from 50 rad/s to 300 rad/s, the best fit was obtained when

$$\zeta = 0.15 \quad (2.21)$$

$$w_2 = 140. \quad (2.22)$$

Putting all these values into (2.18),

$$Y_p(s) = \frac{0.045}{\left(\frac{s}{140} + 1\right)(s^2 + 2(0.15)(4.16)s - 4.16^2)} \quad (2.23)$$

where the numerator has been divided by 1000 to convert units from mm to m. Figure 2.12 compares the shape of this transfer function to the data in Figure 2.11. The closed loop response of the system is also presented for comparison. In Figure 2.12, the open loop plant magnitude is very close and the phase is off by 5° by 5 Hz. The closed loop matching is very good, much better than the simple double integrator plant provides.

The effect of a second order model in the form $\frac{1}{ms^2 + bs - k}$ is better understood, and a good approximation of $Y_p(s)$ is

$$Y_p'(s) = \frac{1}{22.2s^2 + 27.735s - 384.615} \quad (2.24)$$

This approximates the mass of the flotor as 22.2 kg, very close to the actual mass. The Bode plot of this function is shown in Figure 2.13.

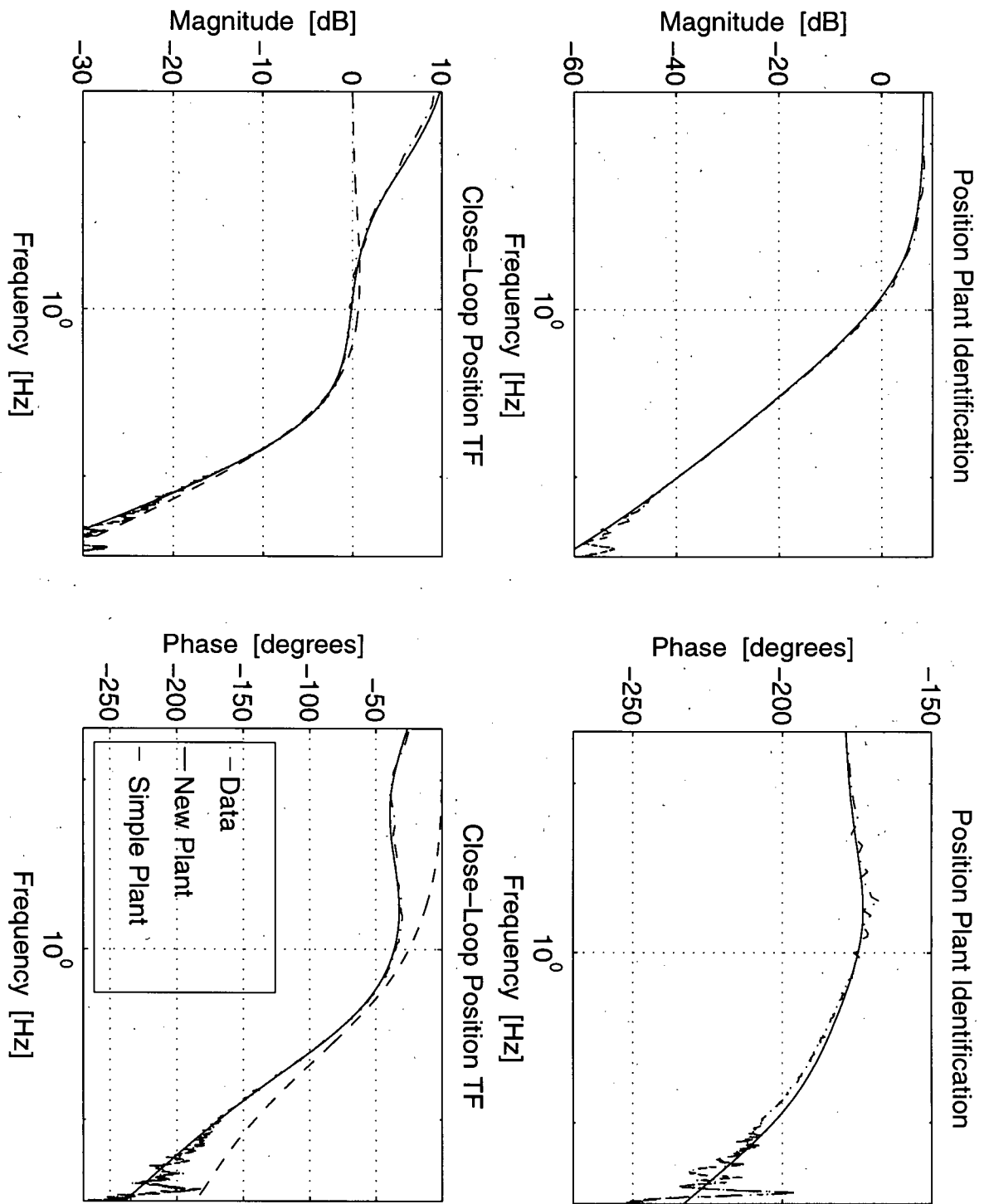
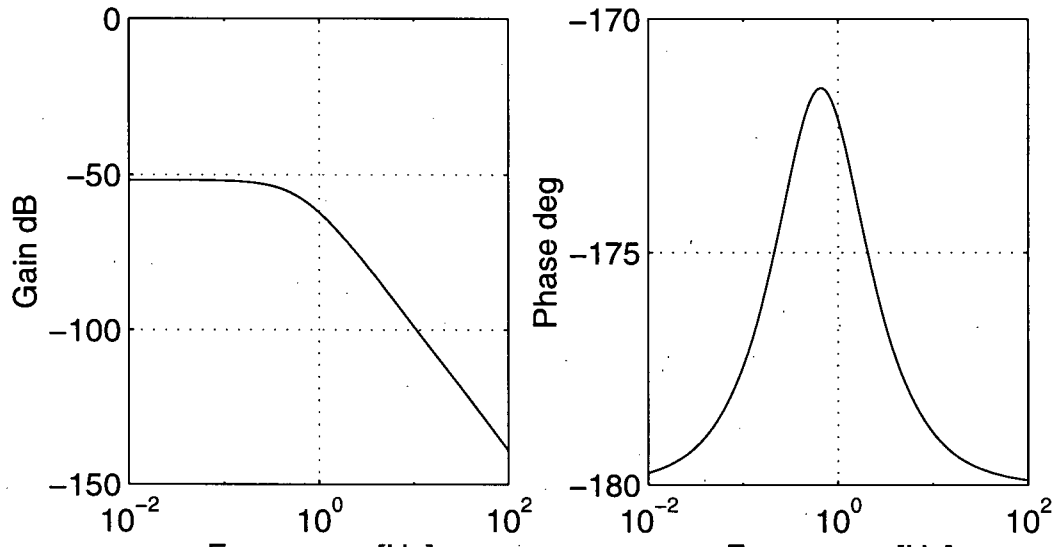


Figure 2.12: Position plant identification. Note position is measured in mm.

Figure 2.13: Bode plot of $Y_p(s)$.

2.5.2 Acceleration Plant

The acceleration plant can be estimated in the same fashion by collecting controller output and flotor acceleration data and using spectral analysis to find the transfer function $\frac{\hat{a}}{\hat{f}} = Y_a(s)$. Figure 2.14 shows the power spectral densities of the input to the system and of the flotor acceleration. These units are consistent. The transfer function and coherence functions are also given. The coherence becomes jumpy below 1 Hz and the transfer function plot below this frequency becomes suspect. Possible reasons for this are low magnitude low frequency components from the input signal and the output magnitude being at the same scale as the noise of the system.

Examining the transfer function in Figure 2.14 it is difficult to get an accurate low frequency response of the plant since the coherence is bad and the plant rolls off at low frequency. The flat magnitude band is about -27 dB, which is approximately 0.045. The bandwidth is quite high, almost 50 Hz, so it can be expected that the filters will play a role.

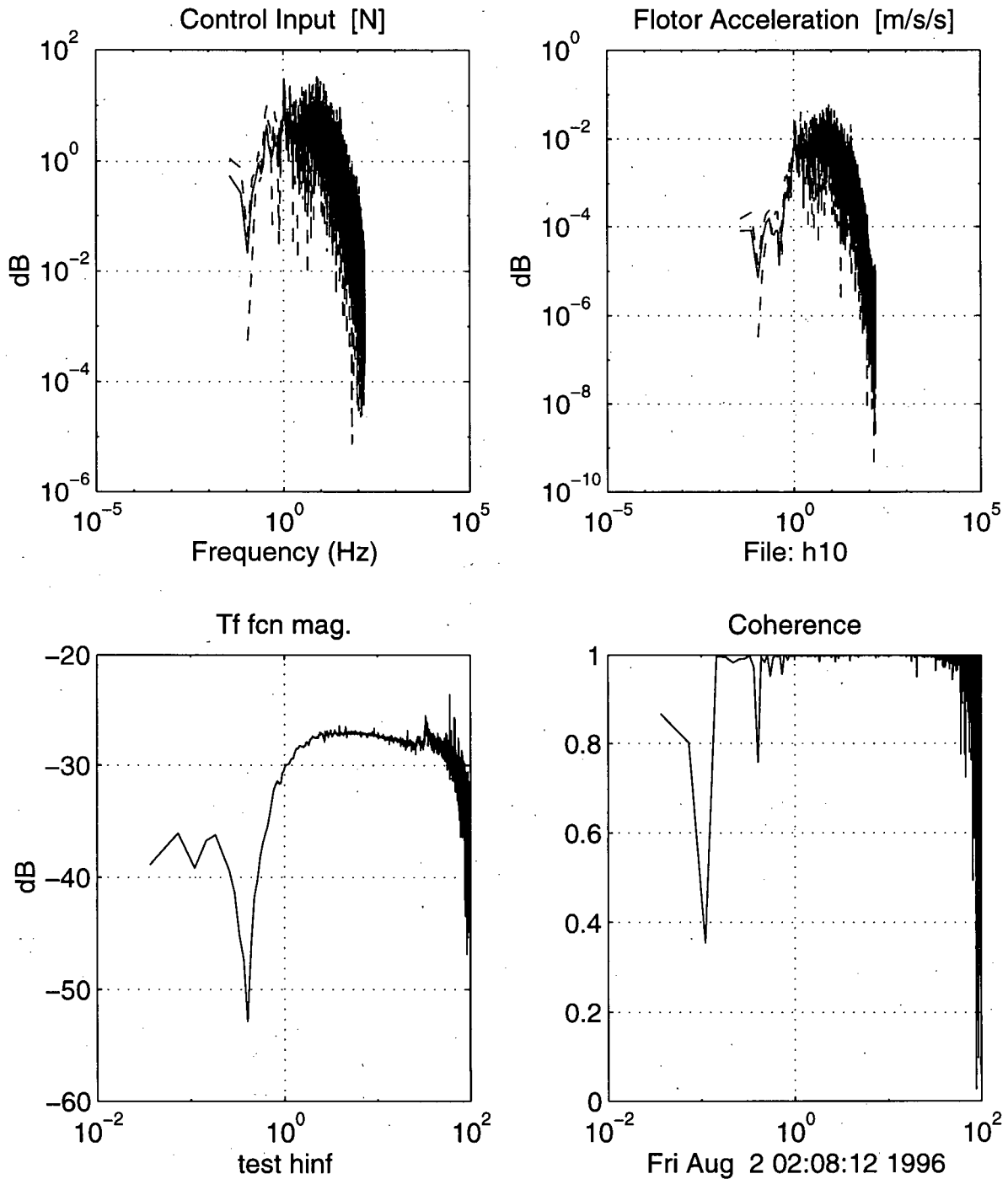


Figure 2.14: Spectral analysis of controller output to flotor acceleration. The Control Input is f , the Flotor Acceleration is a , and the Tf fcn mag is $\frac{\hat{a}}{\hat{f}}$.

The starting guess for the transfer function $Y_a(s)$ will be $s^2 Y_p(s)$. This transfer function fits the low frequency data well but does not roll off at 60 Hz. Since this is getting close to the filter corner frequency, a fourth order low pass Butterworth with corner frequency 30 Hz was added. The transfer function had the correct shape but rolled off much too early. By increasing the filter frequency to 325 rad/s a better fit was obtained.

The acceleration plant is defined as

$$Y_a(s) = \frac{0.045s^2}{\left(\frac{s}{140} + 1\right)(s^2 + 2(0.15)(4.16)s - 4.16^2)} * \text{Butter}(4, 325) \quad (2.25)$$

where $\text{Butter}(4, 325)$ is a fourth order Butterworth filter with corner frequency 325 rad/s. This transfer function is compared to data in Figure 2.15 which shows the open loop plant has good phase agreement and magnitude agreement up to 30 Hz. The closed loop system matching is very good. Since the interesting bandwidth of the system is much less than 30 Hz, it is reasonable to disregard the Butterworth filter in this model.

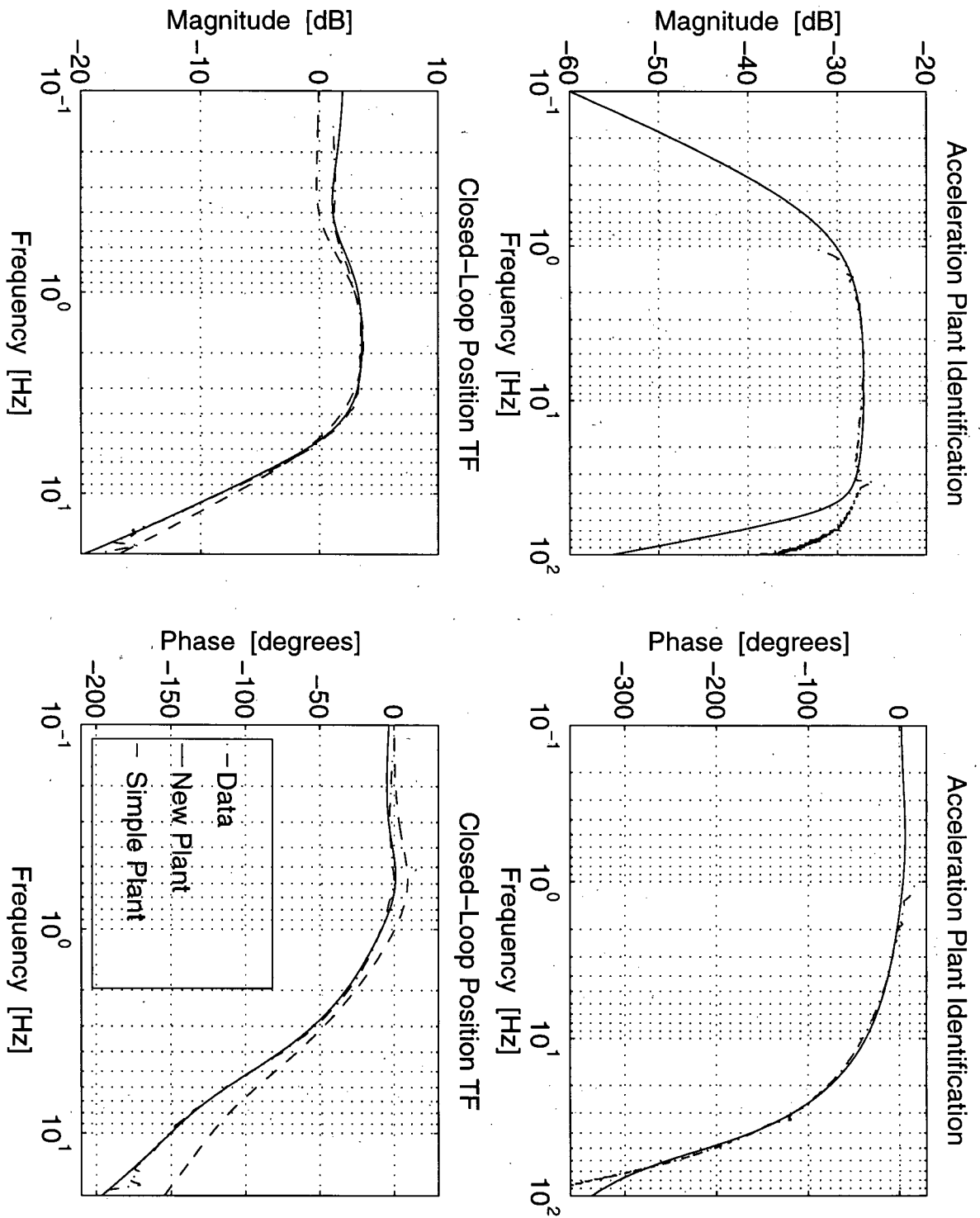


Figure 2.15: Acceleration plant identification.

Chapter 3

H_∞ Controller

This chapter investigates H_∞ control theory for use in vibration isolation. First, the design objectives of the controller are investigated. Then the theory of H_∞ design is presented and design parameters are explained. A position controller using this theory is obtained, and more theory on its design is presented. Acceleration feedback is used to improve the system response and the theory for this is presented.

3.1 Design Objectives

The objective of controller design for vibration isolation is to keep the acceleration levels of the flotor as low as possible. The acceleration of the flotor should have low frequency tracking to keep the flotor returning to the center of the workspace. The controller should also attenuate high frequency disturbance accelerations on the flotor. It has been shown [16] that isolation effectiveness of the controller can be found by examining position excitation. Thus the objective is to design a low bandwidth position controller. Acceleration feedback can then be used to further reduce the bandwidth, creating a better isolation controller. Acceleration control is also used to improve the force disturbance rejection response.

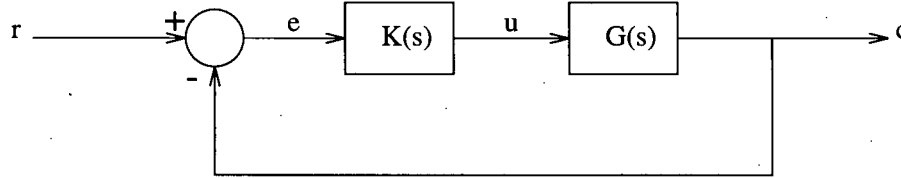


Figure 3.16: The classic feedback loop for control systems.

3.2 Theory

3.2.1 Plant and Design

The simple feedback control system is usually drawn as in Figure 3.16, with $K(s)$ being the controller, $G(s)$ the plant, r the input signal, c the output signal, e the tracking error, and u the control input.

For H_∞ control theory, the plant changes somewhat. The loop is drawn in a unique way, such that the system has two inputs and two outputs. This allows for better understanding of how the system is affected by different changes. Figure 3.17 shows this modified block diagram for H_∞ theory. The input w is the external input and includes all inputs to the system such as disturbances and tracking signals. The other input signal is u and is the control signal from the controller. The two outputs are z and y , which are the control output and measured output respectively. The signal z is not necessarily available for measurement (it doesn't even have to exist) but contains the states of interest for the control design. The various $W_i(s)$ are weights that are applied to the control output to shape the controller and dictate the response of the states in question. The entire system without the controller $K(s)$ is known as the *augmented plant*, $P(s)$. The block diagram is often simplified to Figure 3.18 which is known as standard form.

The augmented plant, $P(s)$, is the transfer matrix from w and u to z and y .

$$\begin{bmatrix} z \\ y \end{bmatrix} = P(s) \begin{bmatrix} w \\ u \end{bmatrix}. \quad (3.26)$$

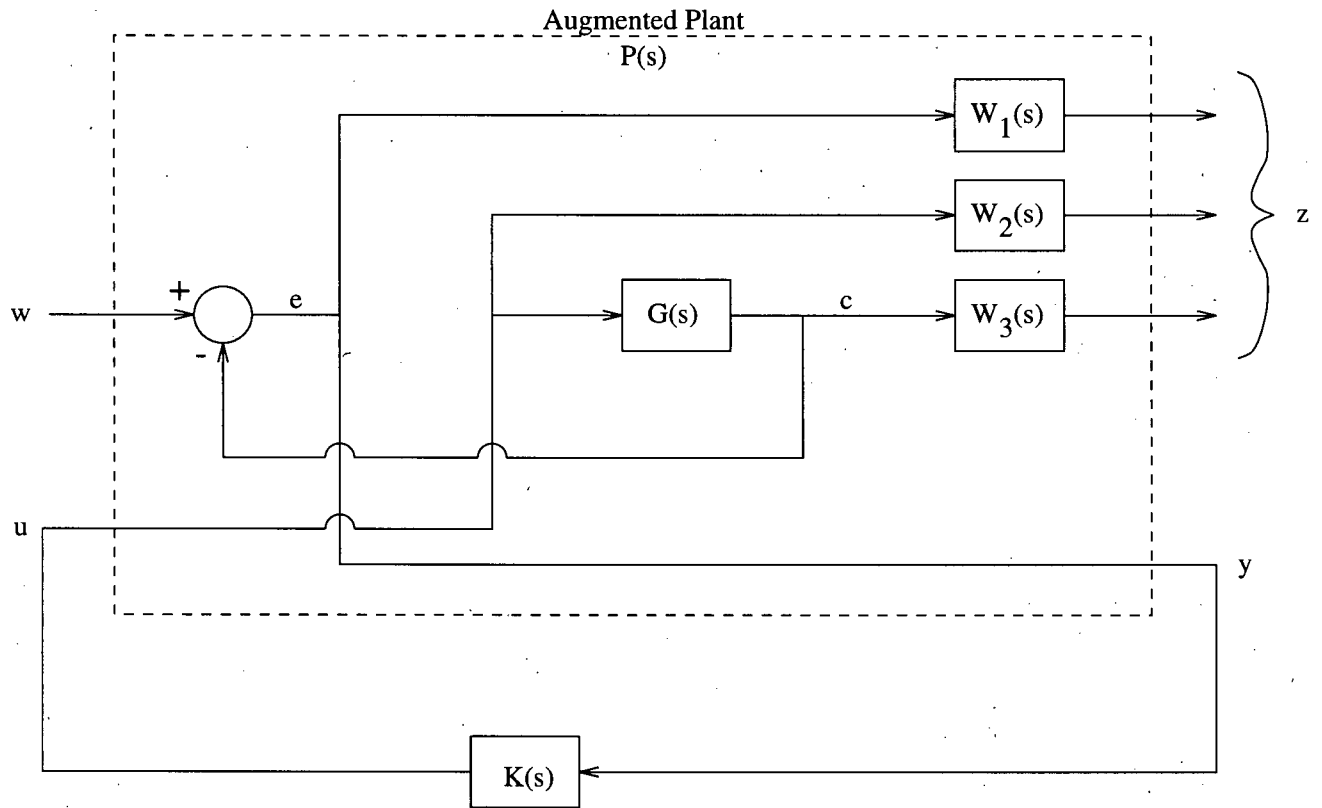


Figure 3.17: The unique model representation for H_∞ control theory.

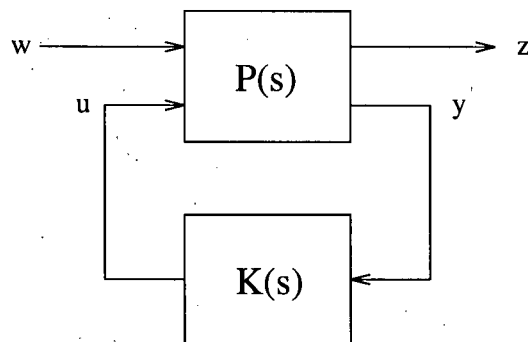


Figure 3.18: Standard form for the H_∞ control problem.

Section A.1 has more augmented plant details.

The basic idea for H_∞ control theory is to minimize the ∞ -norm for the closed-loop transfer function between z and w [25], [23]. More specifically, design the system so that

$$\|T_{zw}(s)\|_\infty < 1. \quad (3.27)$$

where the transfer function is

$$T_{zw}(s) = \begin{bmatrix} W_1 S(s) \\ W_2 R(s) \\ W_3 T(s) \end{bmatrix} \quad (3.28)$$

and

$$S(s) = (I + GK(s))^{-1} \quad (3.29)$$

$$R(s) = K(s)(I + GK(s))^{-1} \quad (3.30)$$

$$T(s) = GK(s)(I + GK(s))^{-1}. \quad (3.31)$$

$S(s)$ is known as the *Sensitivity function*, $T(s)$ is the *Complementary Sensitivity function* and I is the identity matrix of appropriate dimensions. Using this, a successful H_∞ controller has

$$|W_1^{-1}(s)| \geq \bar{\sigma}[S(j\omega)] \quad (3.32)$$

$$|W_2^{-1}(s)| \geq \bar{\sigma}[R(j\omega)] \quad (3.33)$$

$$|W_3^{-1}(s)| \geq \bar{\sigma}[T(j\omega)] \quad (3.34)$$

where $|W_1^{-1}(j\omega)|$ is the desired disturbance attenuation factor. The definitions

$$W_1(s) = W_S(s) \quad (3.35)$$

$$W_2(s) = W_R(s) \quad (3.36)$$

$$W_3(s) = W_T(s) \quad (3.37)$$

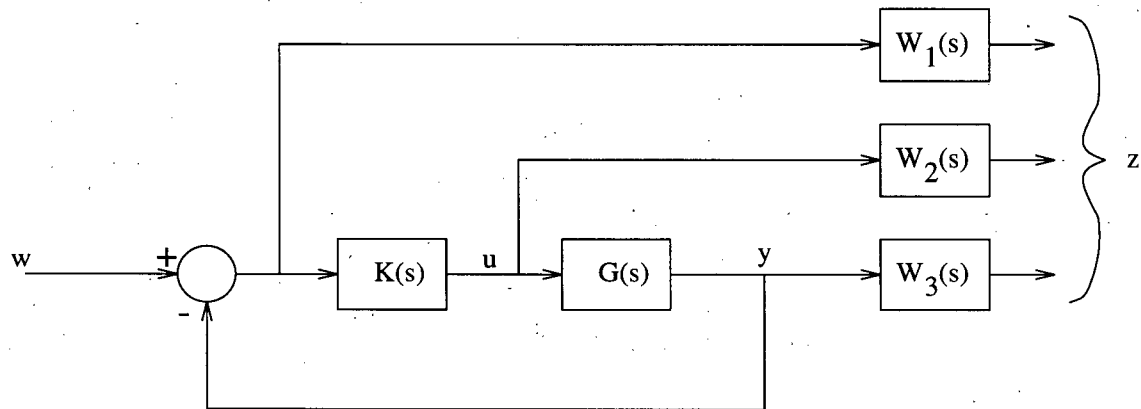


Figure 3.19: The position of the weights in the classic feedback model.

are used interchangeably.

3.2.2 Weights

How the choice of weights affects the performance of the system can be examined two ways: shaping the singular values of the various transfer functions defining the system using (3.32) to (3.34); or, by looking at Figure 3.19, $W_1(s)$ shapes the error, $W_2(s)$ shapes the control signal, and $W_3(s)$ shapes the measured output.

3.2.3 Restrictions

There are certain restrictions in H_∞ design that must be accounted for else the theory will not work [25], [2].

First the plant must be *stabilizable* and *detectable*. This is further explained in Section A.2.

The next restriction on design is that D_{12} and D_{21} must be full rank. Examining the rank requirements, the relationships between D_{12} and D_{21} and the system can be seen by writing the equations

$$z = C_1 x + D_{11} w + D_{12} u; \quad (3.38)$$

$$y = C_2x + D_{21}w + D_{22}u. \quad (3.39)$$

In words, there must be some direct transmission from u to z , and from w to y . The rank of D_{12} can be made full by making the control input a new output at z , but weighted so heavily by a constant it becomes insignificant. Another option is to make the polynomial $W_3G(s)$ strictly proper. To make the rank of D_{21} full, w must have direct transmission to y .

Another requirement deals specifically with the choice of weights. $W_1(jw)$ and $W_3(jw)$ must be chosen in such a way that

$$\bar{\sigma}[W_1^{-1}(jw)] + \bar{\sigma}[W_3^{-1}(jw)] \geq 1, \quad \forall w \quad (3.40)$$

so (3.32) and (3.34) can be achieved [25, page I-40], [24].

The final restriction is the existence of poles or zeroes of the plant on the ju -axis: this is not allowed. As a result, in order to develop a controller for a plant with illegal poles and zeroes, it is required that the plant be transformed in such a way that the infringing poles and zeroes positions are changed. Two methods of doing this are *axis shifting* and *bilinear transform* (see Section A.3).

3.2.4 γ -Optimization

The solution with H_∞ theory is not necessarily optimal - it may be possible to get a better solution using the same shape weights. Or, it is possible, and really quite likely, that the initial choice of weights will not yield a solution to the design problem. In these cases, a γ -iteration technique can be employed [25].

This is the equivalent of doing multiple designs with varying weights. γ has the initial value of 1, and the weights are adjusted such that the new design is run with $\gamma W_1(s)$, $\gamma W_2(s)$ and $\gamma W_3(s)$. For each successful solution, γ can be increased. Each unsuccessful

attempt would require γ to be decreased. In many cases, a binary search is the best vehicle to determine the optimal value of γ . Of course, it is not necessary to multiply each weight by γ - perhaps due to some tough closed-loop specifications certain weights cannot be altered. Then only the weights that are more flexible should be changed.

3.2.5 SISO Simplification

In Single Input Single Output systems, such as a one degree of freedom model, certain simplifications in set up and theory can be done.

Given the standard feedback transfer function, the closed-loop responses of the system are

$$S(s) = \frac{1}{1 + GK(s)} \quad (3.41)$$

$$T(s) = \frac{GK(s)}{1 + GK(s)} \quad (3.42)$$

Interpretation of these functions is easy for a single-input single-output system, and design therefore becomes easy as well.

Getting right back to basics (and leaving out the Laplace operator for simplicity),

$$S = \frac{1}{1 + GK} = \begin{cases} \frac{1}{GK} & GK \gg 1 \\ 1 & GK \ll 1 \end{cases} \quad (3.43)$$

$$T = \frac{GK}{1 + GK} = \begin{cases} 1 & GK \gg 1 \\ GK & GK \ll 1 \end{cases} \quad (3.44)$$

which means to get a flat response of unity gain, $|GK|$ should be larger than 1, and the larger the value, the closer $|T|$ will be to unity. Also, the sensitivity of the system is $\frac{1}{|GK|}$ for large $|GK|$.

Of perhaps of more import in the SISO case are the following relations:

$$\begin{aligned} \text{when } |GK| \gg 1, \quad GK &\approx (1 + GK) = W_1 \\ \text{when } |GK| \ll 1, \quad GK &\approx GK(1 + GK)^{-1} = W_3^{-1}. \end{aligned} \quad (3.45)$$

The implications of this are apparent when deciding on weights for H_∞ design.

- Unity gain implies $|GK| \gg 1$. It can be calculated that if $|GK| = 25$ dB, $|T| \approx -\frac{1}{2}$ dB.
- When $|GK| \gg 1$, as is desired in the bandwidth, $GK = W_1$, and $T \approx 1$.
- The bandwidth of W_3^{-1} dictates the bandwidth of T .
- The slope of W_3^{-1} dictates the slope of T after the roll off, since when $|GK| \ll 1$, as is the case out of the bandwidth, $T = GK = W_3^{-1}$.

Of course, a design that looks only at magnitudes (the train of thought followed here) could cause resonant peaks in the closed-loop transfer function.

3.3 Position Controller

3.3.1 Weight Selection

The augmented plant is shown as Figure 3.20 and indicates the signals to which each weight applies. $W_f(s)$, as explained previously, is small and exists only to make the rank of D_{12} full and is not necessary if the polynomial $W_T G(s)$ is strictly proper. In this model, it is possible to achieve this with a non-proper $W_T(s)$ with order 2. Otherwise $W_f(s)$ would be necessary.

As noted in a previous section, the weights affect the open loop system $GK(s)$ in a direct fashion. $W_T(s)$ controls the bandwidth of the open loop plant, and as such $\frac{1}{W_T(s)}$

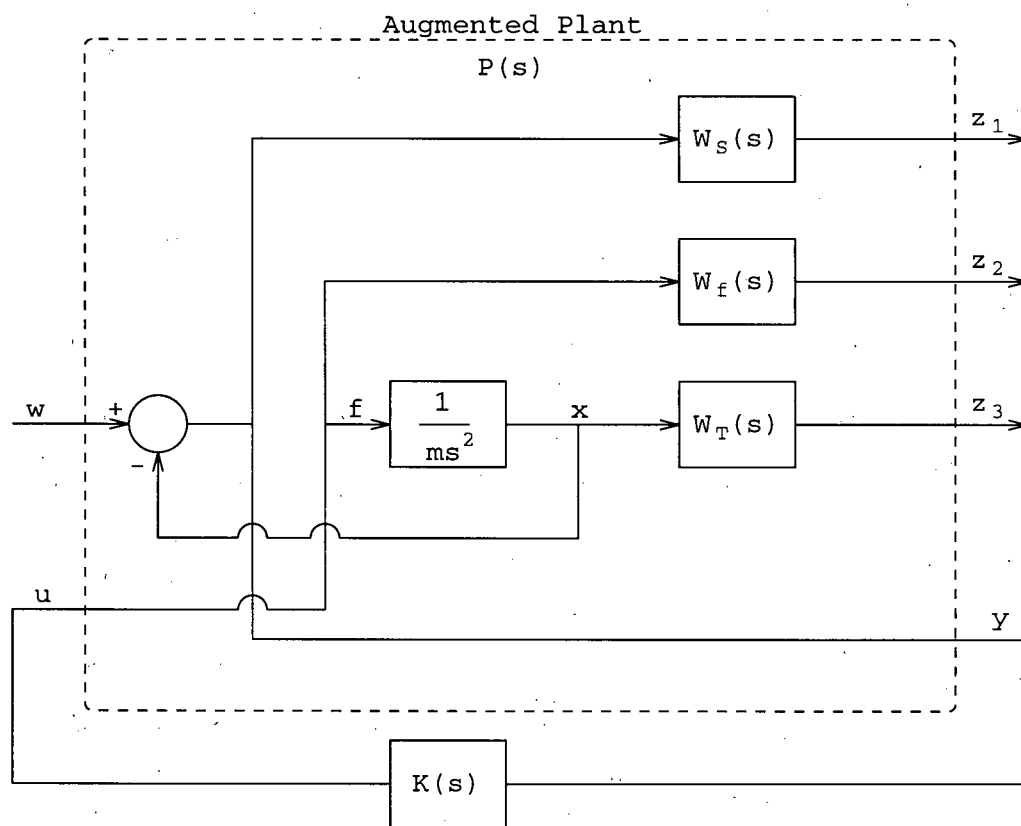


Figure 3.20: Augmented Plant.

is to have unity gain at the desired bandwidth of the system and roll off at the desired rate for the system. $W_S(s)$ dictates the response below the cut off frequency, and should be low pass with greater than unity gain for the closed-loop system to approach unity gain at low frequency.

One set of possible weights are defined as

$$W_S(s) = \beta \left(\frac{\alpha s^2 + 2\zeta \frac{w_c}{2} \sqrt{\alpha} + w_c^2}{\beta s^2 + 2\zeta \frac{w_c}{2} \sqrt{\beta} + w_c^2} \right) \quad (3.46)$$

$$W_T(s) = \left(\frac{s}{w_c} \right)^m \quad (3.47)$$

$$(3.48)$$

where β is the desired DC gain of the open loop system, α is the desired HF gain of the open loop system, w_c is the desired bandwidth of the system in rad/s, ζ is the damping, and $20m$ dB/decade is the roll off of the system. These weights are only two of a set. Other possibilities include changing W_S to fourth order, or increasing the roll off rate of the system. It is necessary to note, however, that if $m > 2$ is desired,

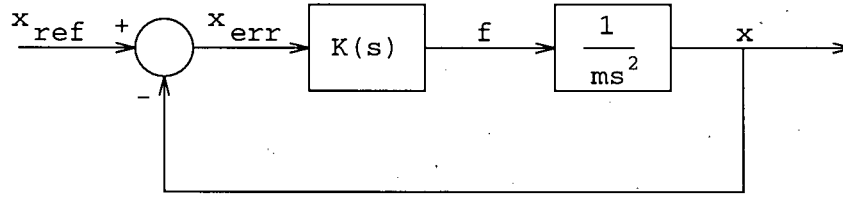
$$W_T(s) = \left(\frac{s}{w_c} \right)^2 \left(\frac{1}{\frac{s}{1000w_c} + 1} \right)^{m-2} \quad (3.49)$$

so that the polynomial $W_T G(s)$ remains proper.

3.3.2 Simple Plant

In its most basic form, the LMIM platform is a simple double integrator plant and therefore the model for design will be as shown in Figure 3.21.

The augmented plant is required in state space form and can be calculated for this mixed sensitivity approach using the MATLAB function *augtf*. If $W_T G(s)$ is strictly

Figure 3.21: Model for H_∞ design - simple double integrator plant.

proper, the matrices can be worked out to be

$$\begin{bmatrix} A & B_1 & B_2 \\ C_1 & D_{11} & D_{12} \\ C_2 & D_{21} & D_{22} \end{bmatrix} = \begin{bmatrix} A_G & 0 & 0 & 0 & B_G \\ -B_{W_S}C_G & A_{W_S} & 0 & B_{W_S} & -B_{W_S}D_G \\ 0 & 0 & A_{W_{TG}} & 0 & B_{W_{TG}} \\ -D_{W_S}C_G & C_{W_S} & 0 & D_{W_S} & -D_G D_{W_S} \\ 0 & 0 & C_{W_{TG}} & 0 & D_{W_{TG}} \\ -C_G & 0 & 0 & 1 & -D_G \end{bmatrix} \quad (3.50)$$

where (A_G, B_G, C_G, D_G) is the state space representation of the simple plant, $G(s)$, such that

$$G(s) = D_G + C_G(sI - A_G)B_G, \quad (3.51)$$

$(A_{W_S}, B_{W_S}, C_{W_S}, D_{W_S})$ is the state space representation of the sensitivity weight $W_S(s)$, and $(A_{W_{TG}}, B_{W_{TG}}, C_{W_{TG}}, D_{W_{TG}})$ is the state space representation of the cascade function $W_{TG}(s)$.

The resulting augmented plant has both $j\omega$ -axis poles and zeroes so a bilinear transform technique (Section A.3) is employed to allow H_∞ design. In this case, the dominant pole placement was chosen to be at -0.1 to start.

With the weight variables chosen as

$$w_c = 2\pi 1.0$$

$$m = 2$$

$$\beta = 15$$

$$\alpha = 0$$

$$\zeta = 0.7$$

a controller, κ , was designed. Its particulars are shown as Figure 3.22, showing the bandwidth of the closed-loop system to be 0.9 Hz. A second order roll off was desired because the plant has a “natural” slope of -40 dB/decade and this choice will simplify the controller response and design. It is also theoretically possible to remove controller poles and zeroes well past the bandwidth of the system without adversely affecting the system response. This idea may be used for reducing high state controllers for complex plants.

3.3.3 Destabilizing Feedback

Using the plant

$$G(s) = \frac{1}{ms^2 - 500} \quad (3.52)$$

and with the weights as defined previously and parameters

$$w_c = 2\pi 3.0$$

$$m = 2$$

$$\beta = 60$$

$$\alpha = 0$$

$$\zeta = 0.7$$

a controller can be designed. It will be designated κ_Y . The specifics of the controller are shown in Figure 3.23, where a large resonant peak is evident in the closed-loop transfer function and the bandwidth is 3.1 Hz. The sensitivity weight is the limiting factor in this design, as it can be seen that the complementary sensitivity weight is not approached.

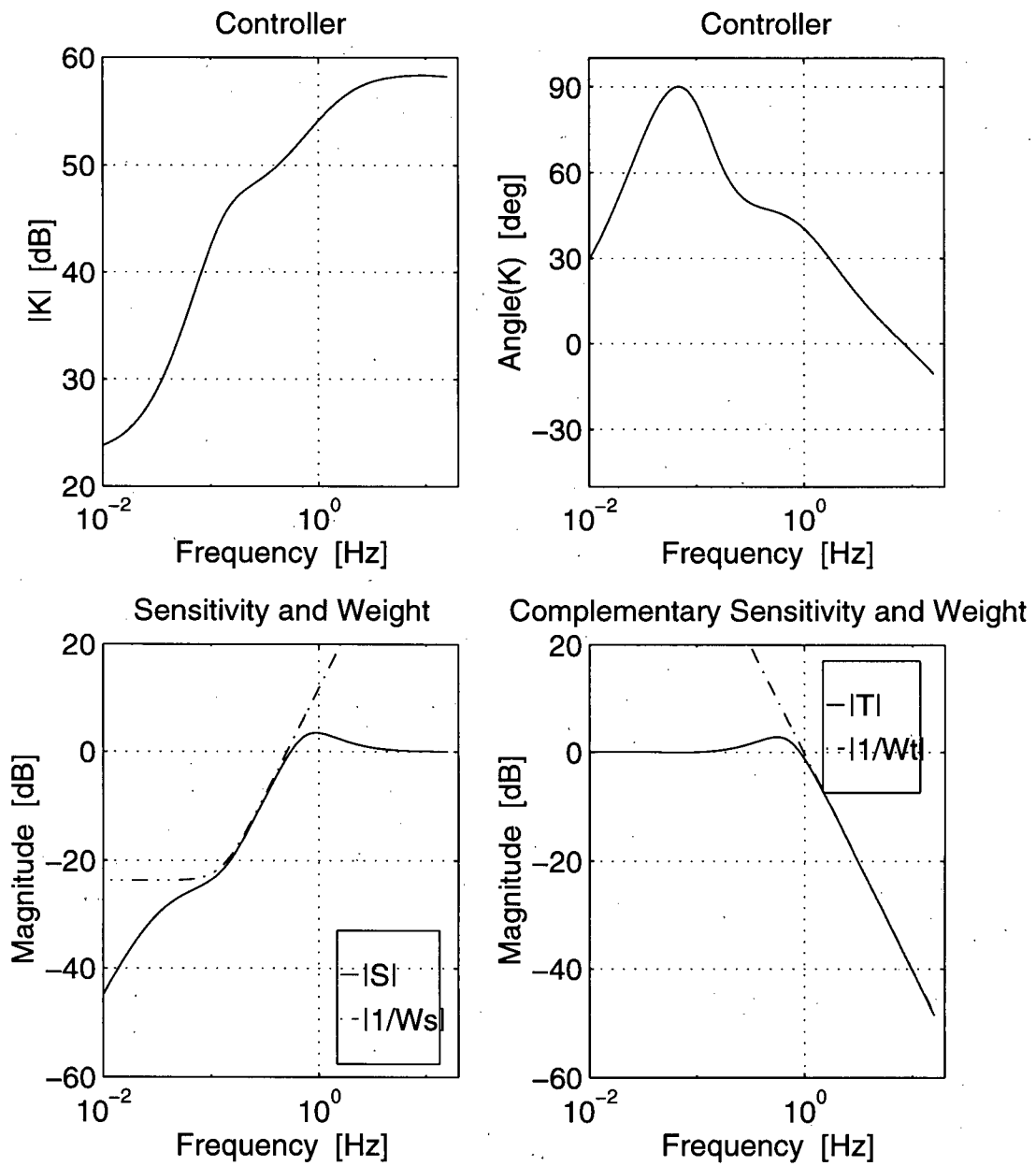


Figure 3.22: H_∞ controller. (a,b) Frequency response of controller, (c) Sensitivity of the system with the sensitivity weight superimposed, (d) Closed-loop response of the system with the complementary sensitivity weight superimposed.

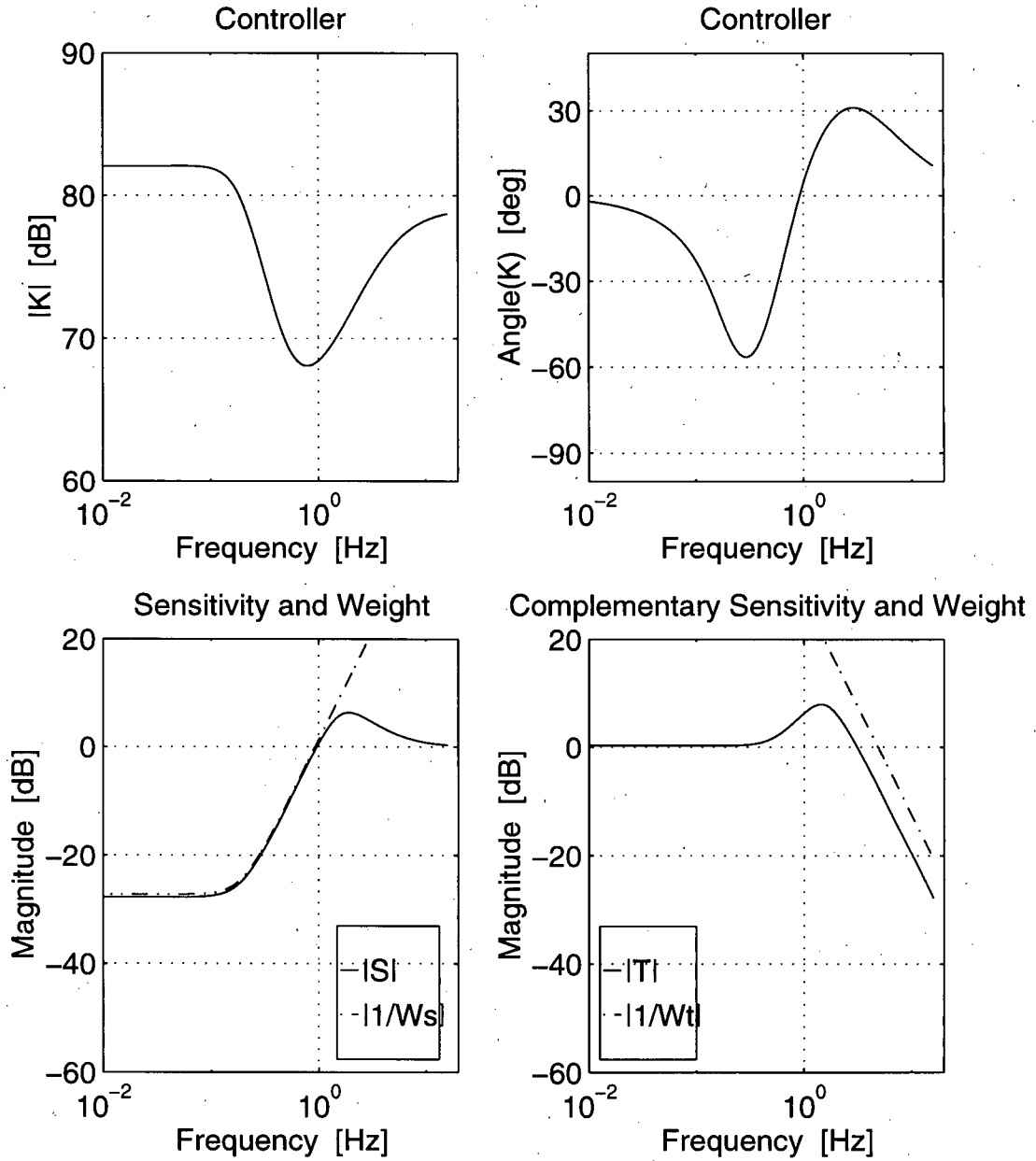


Figure 3.23: Characteristics of the designed system with unstable force feedback.

3.3.4 MATLAB Code

A design tool was developed to aid in producing H_∞ controllers with different plants. The available plant options are double integrator, positive feedback, and $Y(s)$. The weights are as defined in this section and need variables f_c , m , β , and α . Summary plots are drawn as well. The code can be found in Appendix C.

3.3.5 Implementation

Implementation of controller κ on the LMIM reveals that the controller fails by allowing the flotor to fall to the edge of the workspace, which indicates that the bandwidth of the system is not high enough. Simulation with plant $Y(s)$ gives a similar situation which indicates designing a controller with the simple plant is limited in application. There is obviously an increase in the force required as the flotor moves to the limits of the workspace. This corresponds to a negative spring constant for the system which makes it unstable.

Implementing controller κ_Y on the LMIM platform was successful. The flotor centered quickly and a spectral analysis of the motion was done to compare to the theoretical transfer function. This comparison is shown in the first plot of Figure 3.24 and shows good agreement. The difference is a result of improper modeling, including inaccurate modeling of the feedback and lack of modeling the filters for analog and digital conversion.

The size of H is a variable, and its affect on the system was examined. Increasing the value would just make the system stiffer, so the value was lowered as much as possible. As H decreased, it was easier to design controllers - a wider range was possible. At first, the bandwidth of 3.11 Hz was preserved for comparison to the case where $H = 500$. Good characteristics, defined as smooth and timely convergence to the center plus no drift, were observed in controllers designed down to $H = 40$. At this value, the centering

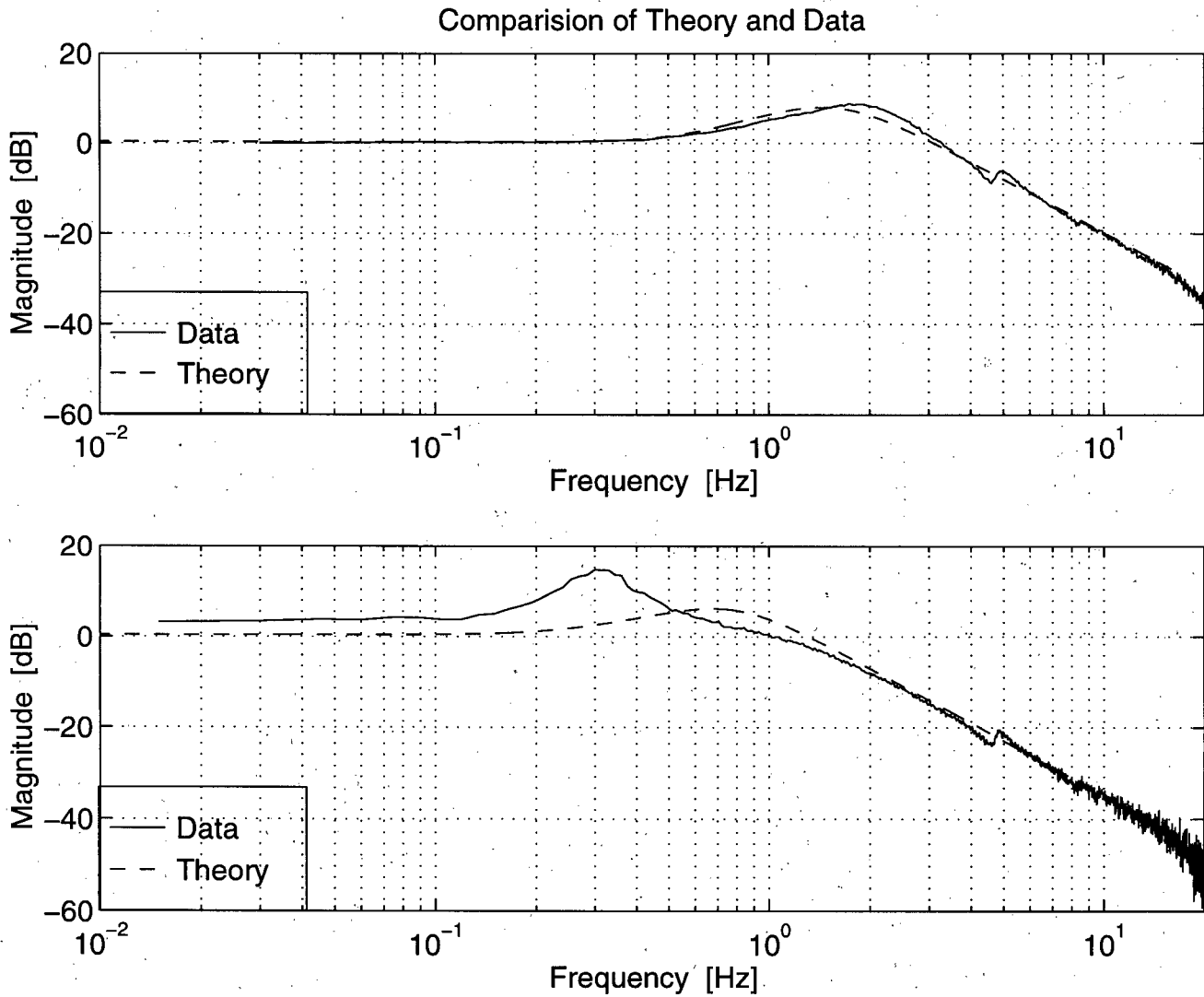


Figure 3.24: A comparison of closed-loop transfer functions of disturbance input to flotor position in theory and practice. (a) $H = 500$ and $f_c = 3.113$ Hz, (b) $H = 40$ and $f_c = 1.3$ Hz.

motion was initially slightly oscillatory until the center was found. The resonant peak for the closed-loop system also decreased as H decreased, to less than 4 dB.

3.3.6 Impulse Response

One measure of performance to a disturbance is the closed-loop systems response to an impulse function. To effect this input in practice, the flotor was suddenly displaced from center and the result studied. Similar results were found when simulated with the plant $Y(s)$.

In the case of the H_∞ controllers, after the displacing force was removed, the flotor returned quickly to the center of the workspace. So quickly, in fact, that overshoot resulted and a short period of oscillations followed. In real terms, this means that while the flotor is safe from falling to the edge of the workspace, the quickness of its zero return causes extra, and unnecessary, accelerations.

3.3.7 The Sensitivity Problem

The sensitivity of a system is bounded by the constraint that the area bounded by the graph of $|S(jw)|$ on a log scale as a function of w on a linear scale be greater or equal to zero [24]:

$$\int_0^\infty \log |S(jw)| dw \geq 0 \quad (3.53)$$

The sensitivity function of the system with κ with these plot axes is shown as Figure 3.25. Obviously the lower the frequency range of attenuation, the less positive area must be made up. But for a higher bandwidth, more positive area is necessary - and hard to get. The solutions are a collection of trade offs.

The sensitivity is mathematically linked to the open loop function, and the sensitivity can only be greater than one when $|GK(s)|$ is near one as well, and with parts of the

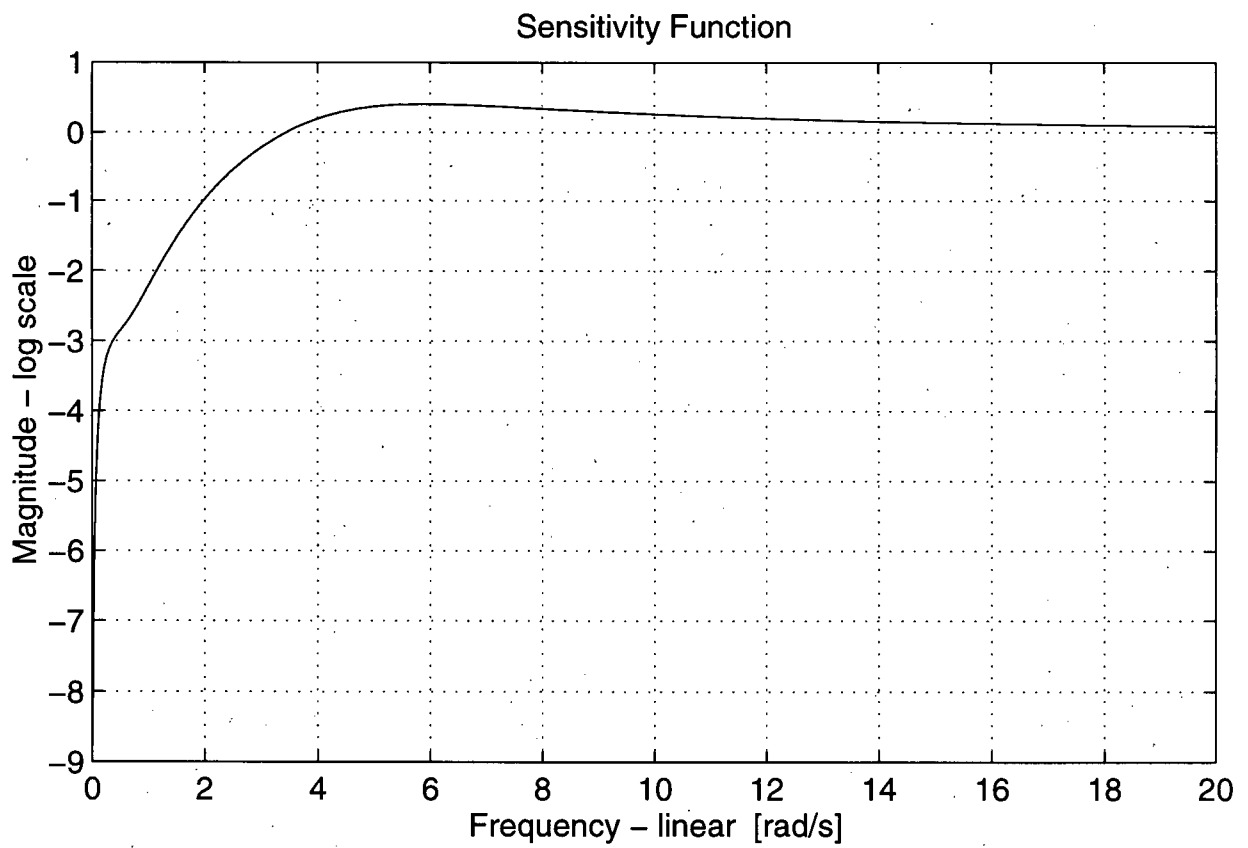


Figure 3.25: Plot to evaluate the area of the sensitivity function.

complex number negative.

One solution would be to keep $|GK(s)|$ near one for a longer range and this could be achieved by having a slower roll off at the bandwidth. This increases the chance for positive $|S(j\omega)|$, but at the same time, if $|GK(s)|$ is decreasing slower, then more negative $|S(j\omega)|$ accumulates.

Another solution would be to have the angle of $GK(s)$ be closer to -180° near the crossover so that the $|GK(s)|$ counts more to the positive area. This has the negative effect of lowering the robustness and stability of the system.

Yet another thought is to have smaller $|GK(s)|$ at lower frequency. This would be the most direct way to decrease the negative area, and also decreases the closed-loop tracking at low frequency, but reduces disturbance rejection.

3.4 Acceleration Feedback

It is not possible to design controllers with arbitrary weight characteristics. As before, trying to design the system for bandwidth much greater than 3 Hz causes problems with the sensitivity. Also, the low frequency seems bounded as well by near 0.3 Hz. Not only does this cause problems when designing but the resulting closed-loop system has a bad transfer function (large DC gain and large resonant peak).

If only position feedback was used this large resonant peak could cause a problem as it is not going to disappear. However, additional data is available to use for control: the accelerations of the flotor. It may be possible to remove the resonant peak while decreasing the bandwidth of the closed-loop position system.

3.4.1 Controller Design Considerations

Now that a stabilizing position controller has been achieved it is time to see if the response of the system can be improved using the acceleration data that is available. A new plant can be defined that includes the closed-loop position system and will be the plant to be controlled. This new plant, G_{ax} is shown in Figure 3.26 in relation to the other important blocks in the design procedure, and a sample Bode plot is shown in Figure 3.27. $G_{ax}(s)$ can be manipulated so that its transfer function is

$$G_{ax}(s) = \frac{s^2}{ms^2 - H + K_x(s)} \quad (3.54)$$

where $K_x(s)$ is the position controller designed previously and all other variables are as before. $W_f = \epsilon$ for rank requirements, and only if $W_T G(s)$ is not strictly proper. If both $W_T(s)$ and $G(s)$ are proper (NB. $G_{ax}(s)$ is strictly proper and therefore $W_T(s)$ must be proper) and there are no pole or zero cancellations, the simplest augmented plant can be determined to be

$$\begin{bmatrix} A & B_1 & B_2 \\ C_1 & D_{11} & D_{12} \\ C_2 & D_{21} & D_{22} \end{bmatrix} = \begin{bmatrix} A_{G_{ax}} & 0 & 0 & 0 & B_{G_{ax}} \\ B_{W_T} C_{G_{ax}} & A_{W_T} & 0 & 0 & B_{W_T} D_{G_{ax}} \\ B_{W_S} C_{G_{ax}} & 0 & A_{W_S} & B_{W_S} & B_{W_S} D_{G_{ax}} \\ 0 & 0 & 0 & 0 & \epsilon \\ D_{W_T} C_{G_{ax}} & C_{W_T} & 0 & 0 & D_{G_{ax}} D_{W_T} \\ D_{W_S} C_{G_{ax}} & 0 & C_{W_S} & D_{W_S} & D_{G_{ax}} D_{W_S} \\ C_{G_{ax}} & 0 & 0 & 1 & D_{G_{ax}} \end{bmatrix} \quad (3.55)$$

where the state space matrices are defined similar to as before.

The desired acceleration function is one with decreased sensitivity to noise in a frequency range with tracking of inputs in this range. This bandwidth cannot extend to DC, but should include the cut off of the closed-loop position plant. The general shape

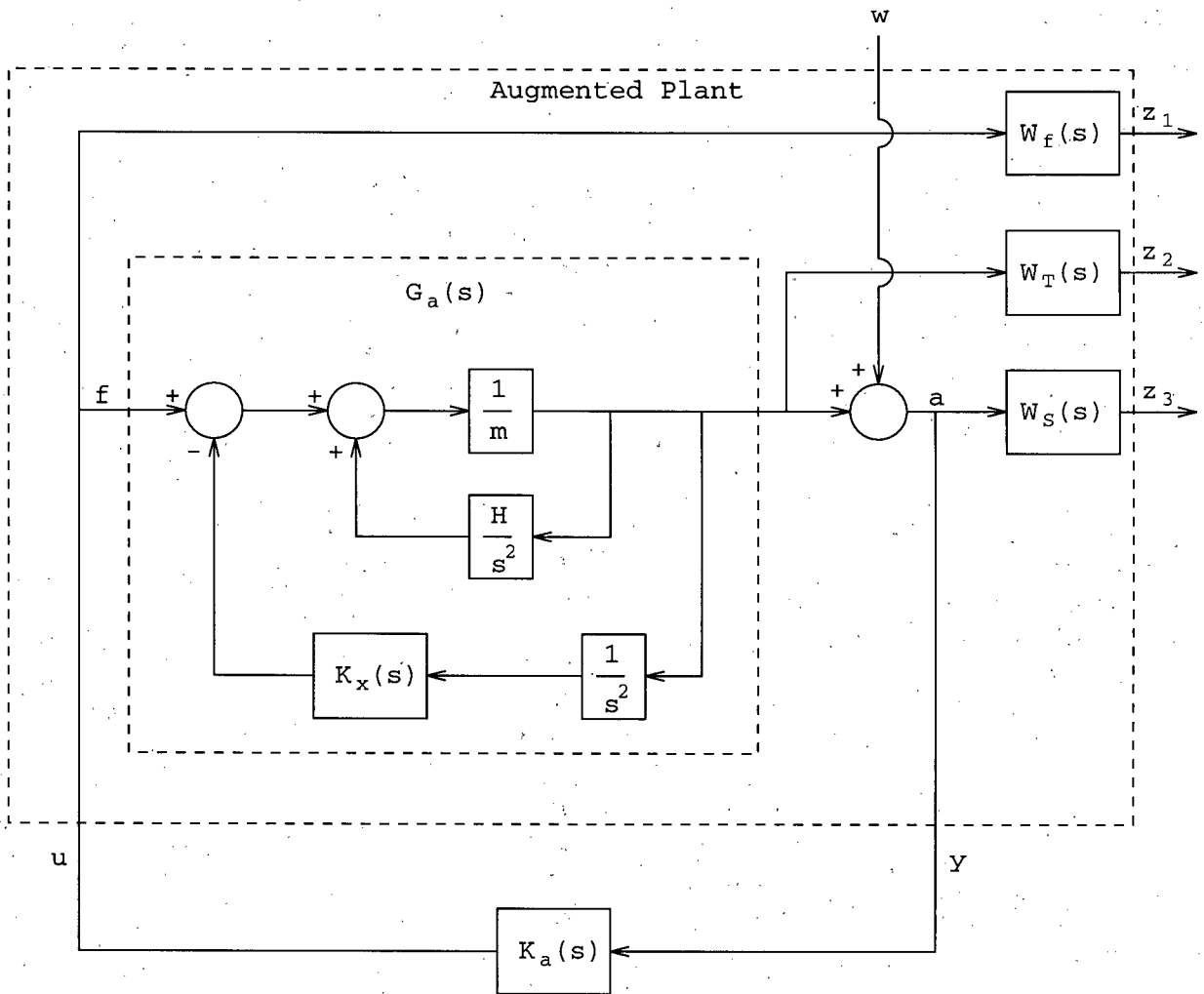
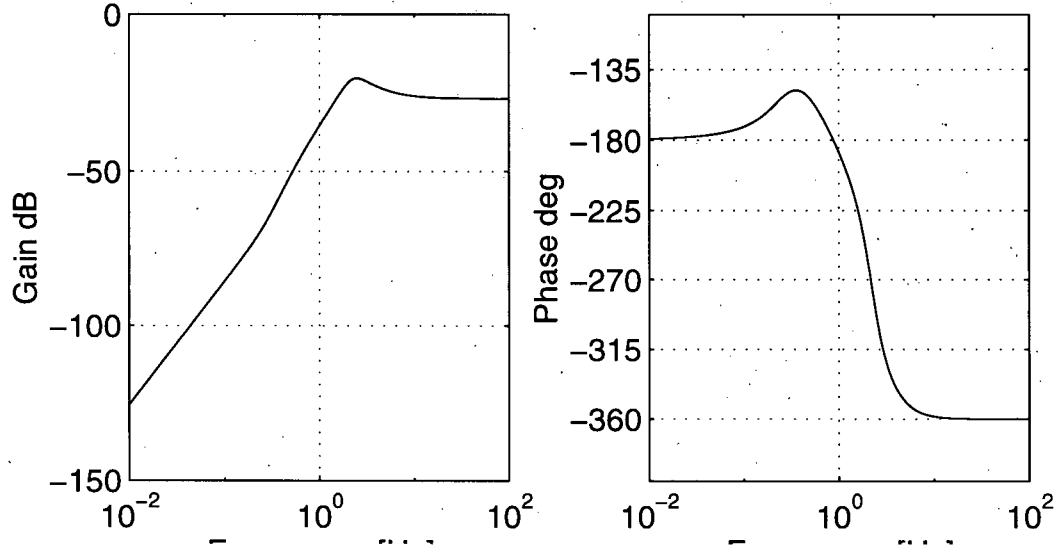


Figure 3.26: The acceleration plant with an inner closed-loop position feedback.

Figure 3.27: Bode plot for acceleration plant $G_{ax}(s)$.

of the desired weights is shown in Figure 3.28, where can be seen that the sensitivity weight is large in the bandwidth to keep the sensitivity small, and the complementary sensitivity weight shapes the closed-loop response outside of the bandwidth. A possible set of weights with second order slope is

$$W_S(s) = \frac{\left(\left(\frac{s}{w_{c1}}\right)^2 + 2\zeta\frac{s}{w_{c1}} + 1\right)\left(\left(\frac{s}{w_{c2}}\right)^2 + 2\zeta\frac{s}{w_{c2}} + 1\right)}{\beta\left(\frac{s}{\sqrt{w_{c1}w_{c2}}} + 1\right)^4} \quad (3.56)$$

$$W_T(s) = \frac{\left(\frac{s}{\sqrt{w_{c1}w_{c2}}} + 1\right)^4}{\left(\frac{3s}{2w_{c1}} + 0.01\right)^2\left(\frac{s}{10w_{c2}} + 1\right)^2} \quad (3.57)$$

where w_{c1} is the cut in of the acceleration controller, w_{c2} is the cut off, ζ is a damping ratio, and β is a gain that brings the magnitude of $W_S(s)$ to one at the crossover. Although these weights only dictate second order roll off, they have an order 4. So increasing the desired roll off greatly complicates the weights. The weights are also strictly proper, since the plant is strictly proper.

Assuming successful design of an acceleration controller, the new transfer function

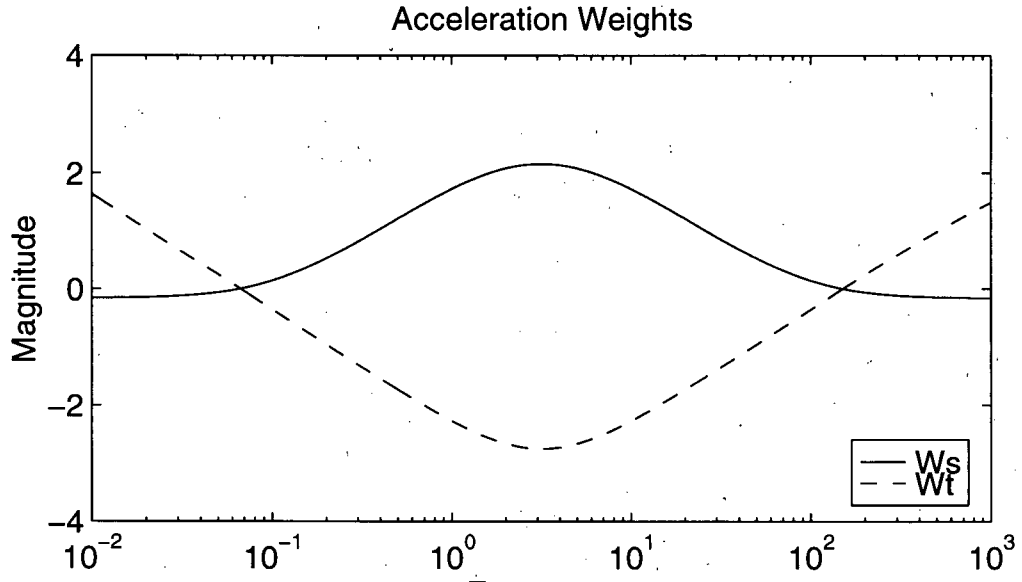


Figure 3.28: General shape of the weights for acceleration controller design.

from disturbance to position becomes

$$\frac{\hat{x}}{\hat{d}} = \frac{\frac{1}{ms^2}K_x(s)}{1 + \frac{1}{ms^2}K_x(s) - \frac{1}{ms^2}H - \frac{1}{m}K_a(s)} \quad (3.58)$$

$$= \frac{G_x K_x(s)}{1 + G_x K_x(s) - G_a K_a(s)} \quad (3.59)$$

based on Figure 3.29, and where

$$G_x(s) = \frac{1}{ms^2 - H} \quad (3.60)$$

$$G_a(s) = \frac{s^2}{ms^2 - H} \quad (3.61)$$

By examining this transfer function, certain things can be inferred about the behavior of the closed-loop system. For low frequencies the system behaves as the position only design since $|G_x K_x(s)| \gg |G_a K_a(s)|$. The new system continues to follow $G_x K_x(s)$ until the order of the magnitudes approach. At this time the phases of the functions come into play. If the phase difference is very large while $|G_x K_x(s)| \approx |G_a K_a(s)|$ then the closed-loop response will show a resonant peak. As $|G_a K_a(s)|$ continues to increase, $|\frac{\hat{x}}{\hat{d}}|$ begins

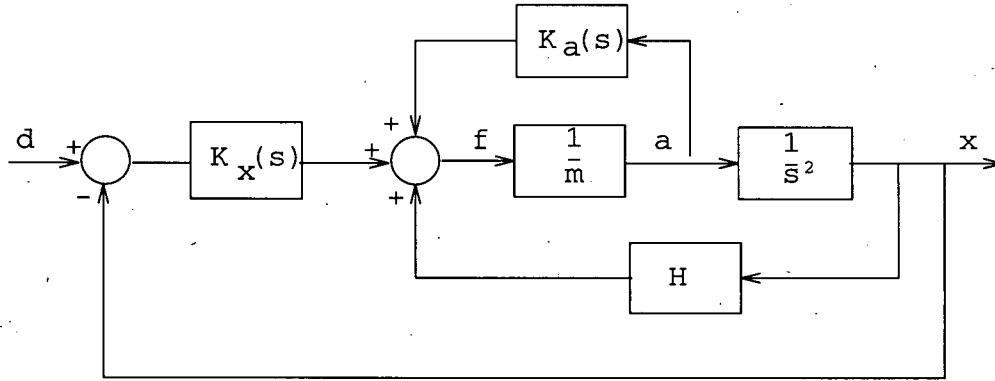


Figure 3.29: The complete position plant with acceleration feedback.

to decrease and is equal to the ratio of $|G_x K_x(s)|/|G_a K_a(s)|$. This is how the system bandwidth is decreased, so the value of this new cut off is dependent on the frequency where $|G_x K_x(s)| \approx |G_a K_a(s)| > 1$, and in theory could be placed anywhere with the proper choice of controller. As $|G_a K_a(s)|$ decreases, the system again approaches the simple position only closed-loop function. Note this will also eliminate the resonant peak of the position only transfer function.

A better indication for design parameters comes with a little manipulation of (3.58) (see Appendix B for more closed-loop manipulations):

$$\begin{aligned}
 T_{xa}(s) &= \frac{\frac{1}{ms^2} K_x(s)}{1 + \frac{1}{ms^2} K_x(s) - \frac{1}{ms^2} H - \frac{1}{m} K_a(s)} \\
 &= \frac{K_x(s)}{ms^2 + K_x - H - s^2 K_a(s)} \\
 &= \frac{K_x(s)}{(ms^2 + K_x(s) - H) \left(1 - \frac{s^2 K_a(s)}{ms^2 - H + K_x(s)}\right)} \\
 &= \left(\frac{\frac{K_x(s)}{ms^2 - H}}{1 + \frac{K_x(s)}{ms^2 - H}} \right) \left(\frac{1}{1 - G_{ax} K_a(s)} \right) \\
 &= \left(\frac{G_x K_x(s)}{1 + G_x K_x(s)} \right) \left(\frac{1}{1 - G_{ax} K_a(s)} \right) \\
 &= T_x S_{ax}(s) \tag{3.62}
 \end{aligned}$$

where $T_{xa}(s)$ is the closed-loop position function with acceleration feedback, $T_x(s)$ is the

closed-loop position function without acceleration feedback, and $S_{ax}(s)$ is the sensitivity of the acceleration system with position controller. The last definition also gives $W_S(s)$, since H_∞ attempts to near equalize $S(s)$ and $\frac{1}{W_S(s)}$. $W_S(s)$ should be chosen to reflect the desired new response of the system, and $W_T(s)$ should be chosen to complement this.

Knowing the desired sensitivity, choose $W_S(s)$ such that $|W_S^{-1}(s)| \geq |S(s)|$. The Bode plot of $G_{ax}(s)$ shows that it increases at 40 dB/decade at low frequency and levels off to a gain less than one. In an attempt to keep the controller simple, $W_T(s)$ was picked to match the controller roll up at low frequency, and to have a 20 dB/decade slope through the cut off (for robustness and so that the controller doesn't have to deviate so much from $G_{ax}(s)$). $W_T(s)$ also has a leveling term so that it is a proper function. These simple weights have the same shape as (3.56) and (3.57), confirming the previous selection.

3.4.2 Acceleration Controller

A controller that should in theory work can be found by choosing the acceleration weights to be as in (3.56) and (3.57)

$$W_S(s) = \left[\frac{[(\frac{s}{w_{c1}})^2 + 2\zeta \frac{s}{w_{c1}} + 1][(\frac{s}{w_{c2}})^2 + 2\zeta \frac{s}{w_{c2}} + 1]}{\beta(\frac{s}{\sqrt{w_{c1}w_{c2}}} + 1)^4} \right]^{m/2} \quad (3.63)$$

$$W_2(s) = \epsilon \quad (3.64)$$

$$W_T(s) = \frac{(\frac{s}{\sqrt{c_1 c_2}} + 1)^4}{(\frac{s}{c_1} + 0.01)^2 (\frac{s}{10w_{c2}} + 1)} \quad (3.65)$$

where w_{c1} and w_{c2} are the low and high frequency ranges for the bandpass, c_1, c_2 are frequencies a little smaller than the cut in and a little larger than the cut off respectively (done so that $|W_S(jw)|^{-1} + |W_T(jw)|^{-1} > 1$), and m is the desired slope of W_1 . By setting the bandpass range to be 0.05 rad/s to 20 rad/s, and choosing a simple second order slope for W_S with unity damping, the weights are

$$W_S(s) = \frac{s^4 + 40.1s^3 + 404s^2 + 40.1s + 1}{1.63s^4 + 6.54s^3 + 9.81s^2 + 6.54s + 1.63} \quad (3.66)$$

$$W_2(s) = 10^{-5} \quad (3.67)$$

$$W_T(s) = \frac{1.09s^4 + 4.25s^3 + 6.25s^2 + 4.08s + 1}{3.13s^3 + 625s^2 + 0.5s + 10^{-4}} \quad (3.68)$$

The new position transfer function is shown in Figure 3.30 and it indicates a small resonant peak of less than 1 dB exists at the new cut off of approximately 0.4 rad/s. The behavior of the transfer function is easily explained. The new function can be represented as

$$\frac{x}{X_{ref}} = \frac{G_x K_x}{1 + G_x K_x - G_a K_a} \quad (3.69)$$

where subscript x refers to position design and subscript a refers to acceleration design. The peak is a result of the phase characteristics of $G_a K_a$. As $|G_a K_a|$ approaches $|G_x K_x|$, the phases of the functions must not be opposite, or near opposite, else the peak is created.

Another thing to notice about Figure 3.30 is that the magnitude only drops to about -10 dB for the first while. This is because $|G_a K_a|$ is not much larger than $|G_x K_x|$, and when the two magnitudes are similar, mathematically $\frac{x}{X_{ref}} \approx \frac{1}{2} = -6$ dB. To effect a larger decrease in magnitude would either require making $|G_x K_x|$ smaller, which would affect the DC and low frequency gain of the system, or by making $|G_a K_a|$ larger, which would require making the order of W_{1a} larger. Making the order larger, however, dramatically increases the resonant peak, which can be somewhat reduced by choosing larger damping ratios. Of course, larger order also means a larger controller order.

Technically, the roll off can be placed anywhere with the proper choice of bandwidth, but practically there would be limitations.

If $|G_x K_x|$ is around 25 dB, it takes about 1/2 a decade for $G_a K_a$ to get that large, so that is when the new roll off starts. For example, if a desired new roll off was 0.05 rad/s, we choose the low frequency bandpass for acceleration to be 0.01 rad/s and after some tuning we get Figure 3.31.

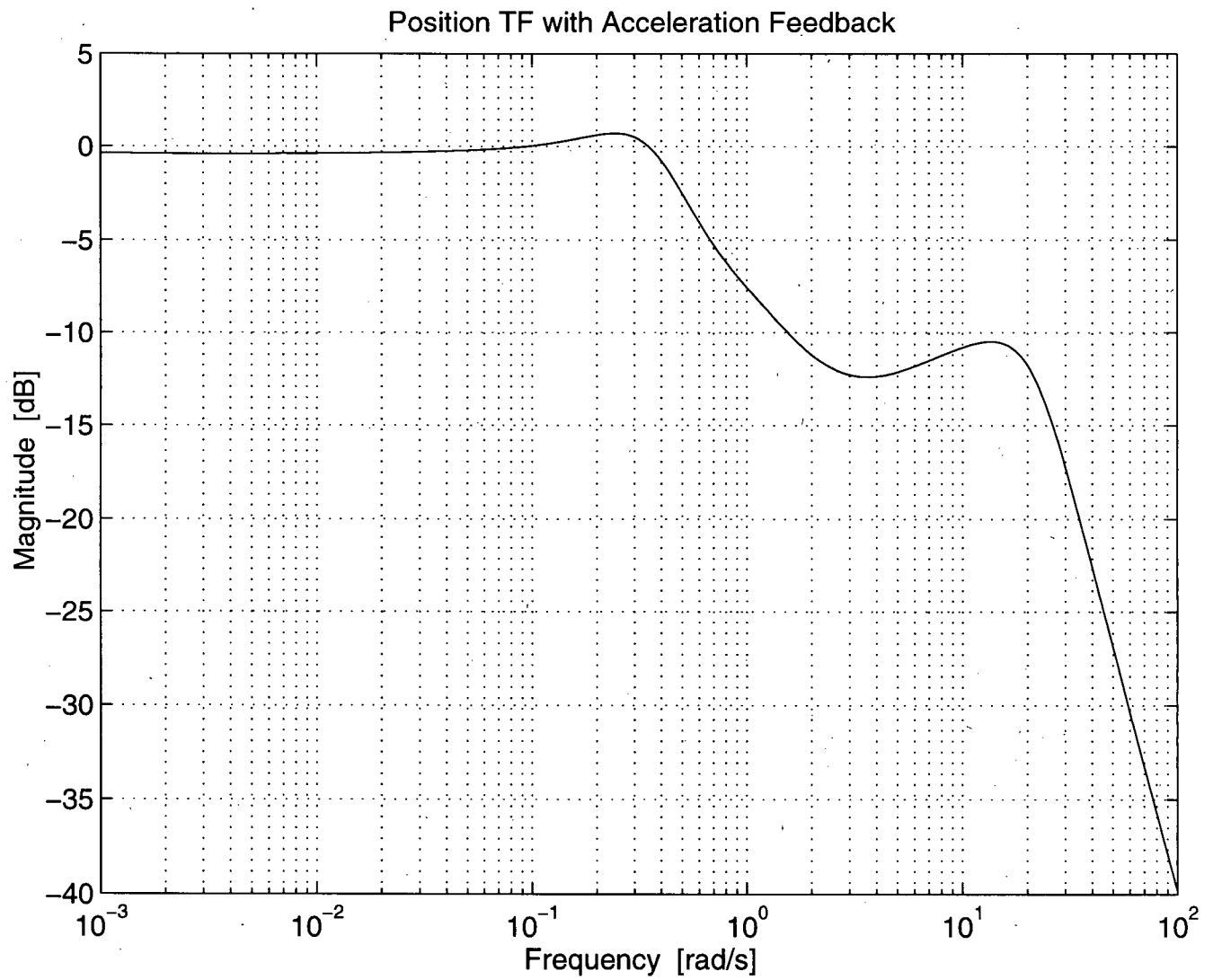


Figure 3.30: A position transfer function with acceleration feedback.

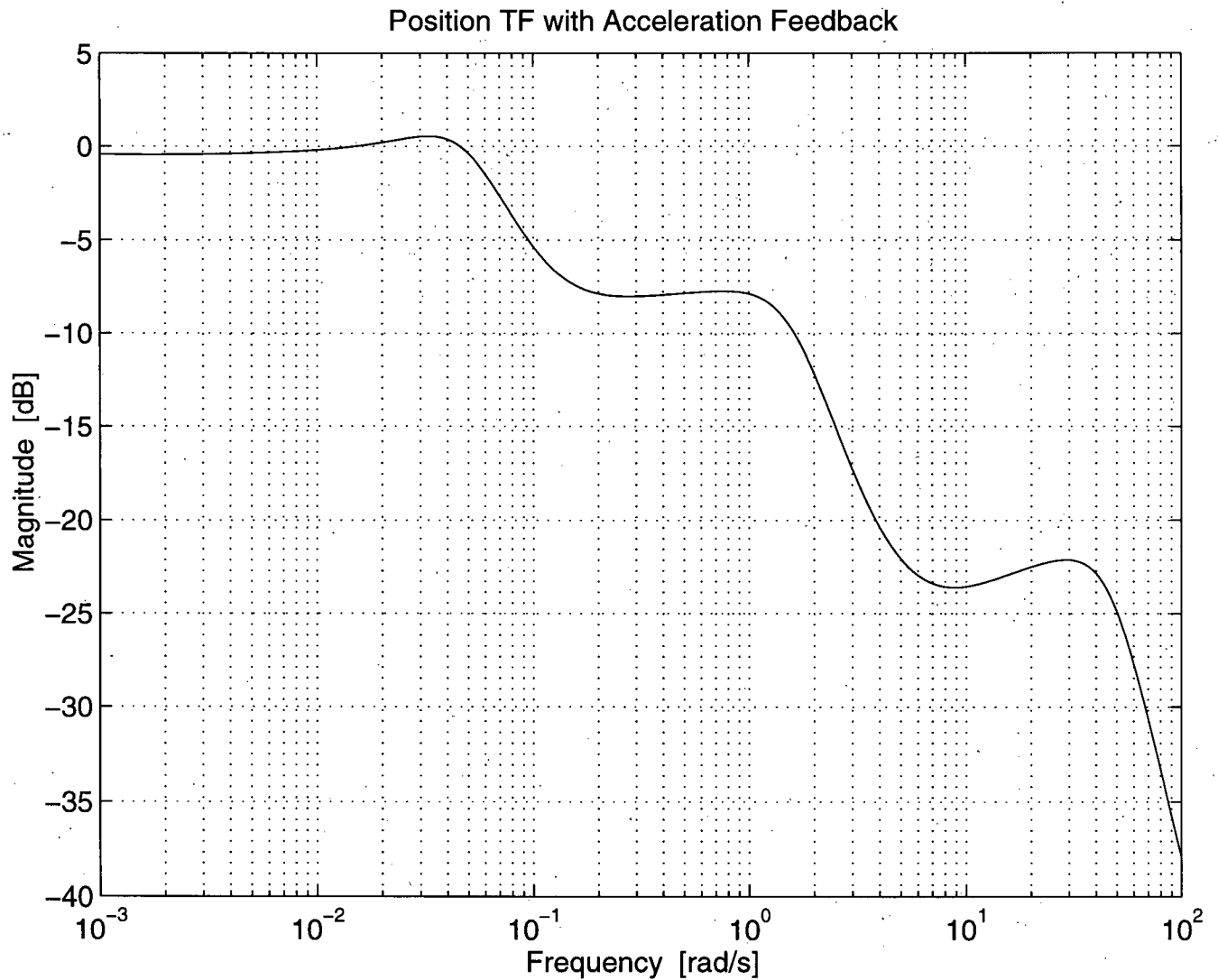


Figure 3.31: An attempt to get the new corner frequency to 0.05 rad/s. The parameters used in the design: Position - DC = 40, HF = 0.01, slope = -2, bandwidth = 10 rad/s. Acceleration - frequency range 0.01 rad/s to 50 rad/s, damping ratio = 10, order = 4. Note that this controller has 19 states.

The important design plots are those of $G_a K_a$ and $G_x K_x$. Proper manipulation of these will give the desired design. Looking at the plots can also give a good indication of the resulting system before it is even designed.

3.4.3 Force Rejection

The purpose in adding acceleration force feedback was two fold. First the position roll off was to be pushed to a lower frequency, and that was accomplished earlier. Second, a better response to the disturbance force was expected. This has yet to be confirmed.

The hope is that a disturbance force, applied just before the plant, has a lesser effect on the plant acceleration with acceleration feedback than without. To test this, the controllers designed leading to Figure 3.30 were used. The effect of the disturbance force can be seen in Figure 3.32 and shows a better rejection function with feedback than without. In fact, disturbance rejection can also be controlled by $|G_a K_a|$, where in a higher magnitude over a wider range decreases the disturbance effect accordingly.

3.4.4 Acceleration Controller Implementation

No designed acceleration controllers stabilized the LMIM platform. The LMIM is an inverted pendulum and needs a higher bandwidth controller to be stable.

3.5 Conclusions

H_∞ design theory was able to successfully design a position controller but not an implementable acceleration controller. H_∞ design for the single degree of freedom case is very straight forward to set up since the weights have direct relevance to the open loop, and hence closed-loop system. However, even if the problem is set up properly, a solution does not always exist.

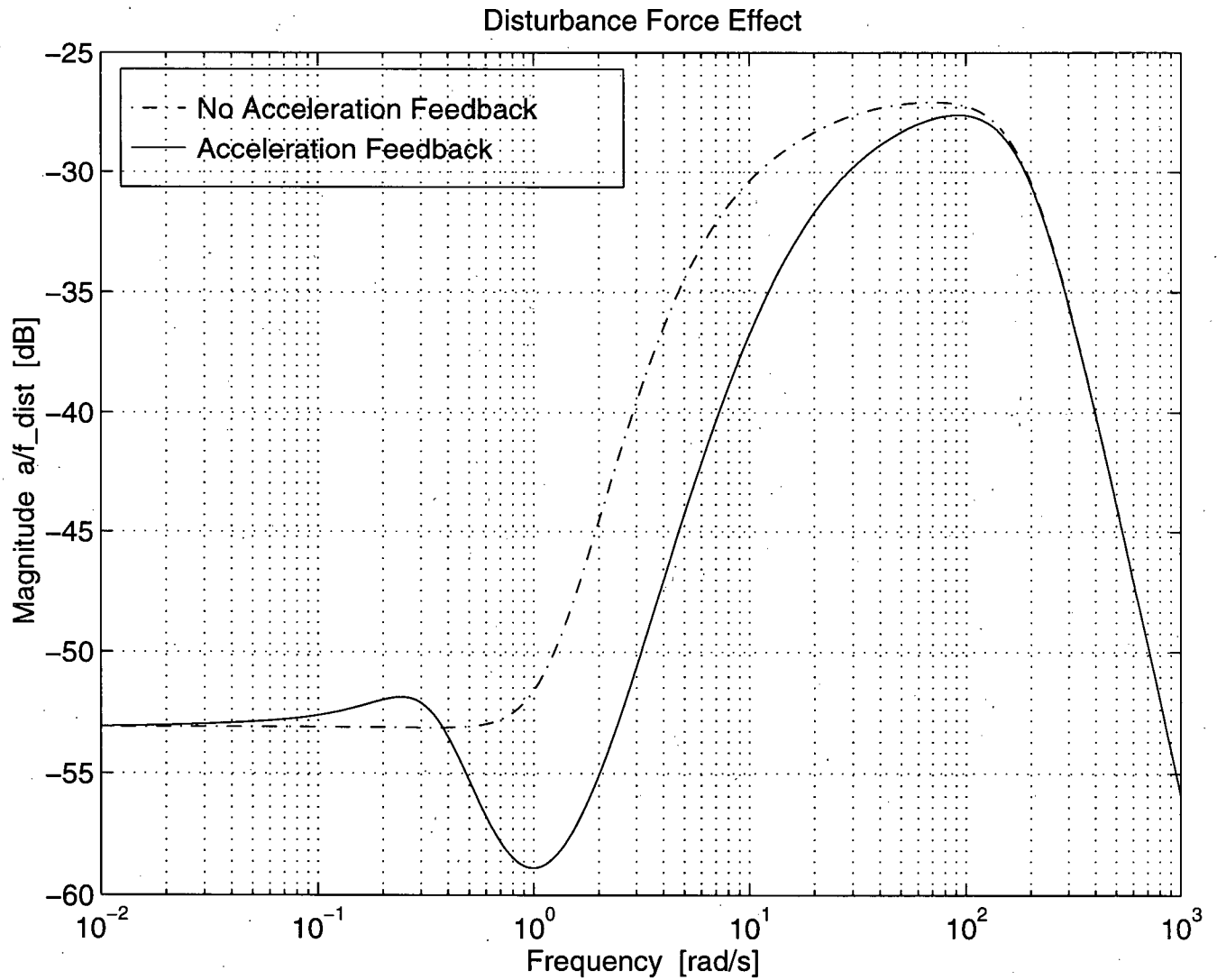


Figure 3.32: The effect of a disturbance force added just before the plant on the plant acceleration. Acceleration feedback decreases the effect.

This chapter provided a lot of insight into selecting design weights specifically for a single input single output system. The sensitivity function desired dictates the shape of W_S for the performance specification. W_T limits the bandwidth of the closed-loop system. Using this information, suitable weights can be formulated for H_∞ control design.

For this case the plant created complications in the controller solution that were difficult to overcome. The iw -axis poles of the simple plant and the right half plane pole [20] of the more accurate plant hinder finding solutions to all problems.

Even with this problem, the H_∞ controller designed showed slightly better performance than PID controllers. If the problem can be addressed satisfactorily then the use of H_∞ design will provide good vibration isolation controllers.

Chapter 4.

The Coarse-Fine System

This chapter describes the coarse-fine system that will be tested on the DC-9. A description of the hardware and software is followed by the development of a model for simulation.

4.1 Hardware and Software

4.1.1 Hardware

The hardware for the one degree of freedom Coarse-Fine Tracking System itself consists of two main parts: the fine stage wrist and the coarse stage rail. This system was designed and developed by Tim Salcudean and Chia-Tung Chen at the University of British Columbia [29, 30, 31]. A simple representation is shown in Figure 4.33.

The wrist is a similar and smaller version of the LMIM, described previously, and operates in the same fashion. The wrist also has a flotor that is suspended above the stator by magnetic field forces, but instead the flotor contains the permanent magnets and the stator holds the wire coils. The position of the flotor with respect to the stator is determined by position sensing diodes, and the acceleration of the flotor is determined by an accelerometer mounted externally. The flotor workspace is limited, and in the vertical direction the maximum displacement from centre is ± 4.5 mm. The stator is attached to a plate that is in turn bolted to a linear bearing car. The acceleration level of the stator is determined by an accelerometer attached to the plate. The flotor is the fine stage. The

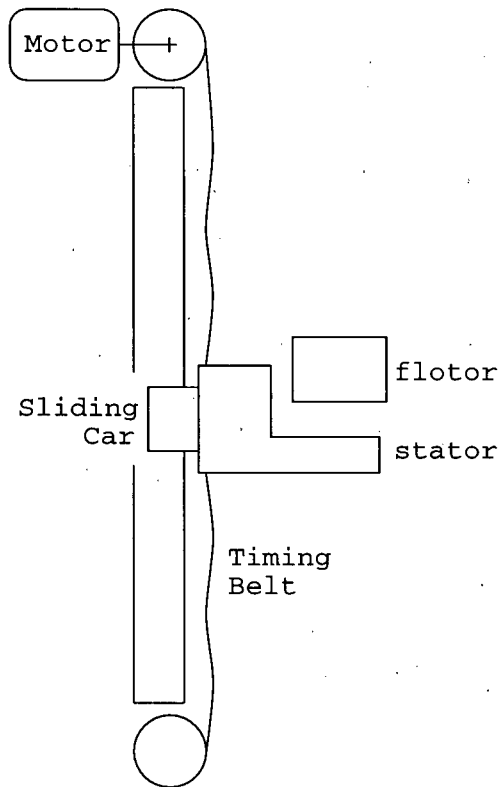


Figure 4.33: Diagram of the 1 DOF coarse-fine tracker.

plate, stator, accelerometers, and linear bearing car are collectively the coarse stage.

The coarse stage is set on a linear bearing rail with low friction bearings. This rail is 1600 mm long and has a small shock damper at each end to soften any impact on the wrist. The rail is attached to a 1915 mm long aluminum I-beam that is clamped vertically to a camera pole in the DC-9. The coarse stage is also attached to a timing belt on one side of the I-beam that is wrapped tightly around two pulleys, one of which is attached to a DC motor. The velocity of the timing belt is reduced by viscous forces of the bearing system and acceleration limits of the motor. The other side of the I-beam has a position transducer and the magnet is attached to and moves with the coarse stage. The approximate motion limit of the coarse stage on the rail is ± 630 mm. The wrist gets power from a larger six channel current driver which is in turn powered by a 25 Volt DC supply, as is the motor current driver. All signals are filtered and connected to the computer by cables.

The signals are interfaced with a computer through the digital/analog converter on the DSP board. The output signals from the computer are routed to the two current amplifiers, and the input signals are from the wrist PSD's, the coarse transducer, and the accelerometers.

4.1.2 Software

The software used to move control code onto the DSP board is one developed at UBC by Nelson Ho called *IN*. Separate data storing software is necessary to write the variables to the computer hard drive; this was developed at UBC by Chia-Tung Chen. The wrist is controlled by a simple PID controller, but is certainly not restricted to this. The method described previously in the thesis could be adapted for the wrist with a few changes in the variables.

Appendix D gives some particulars for the software used to control the coarse-fine

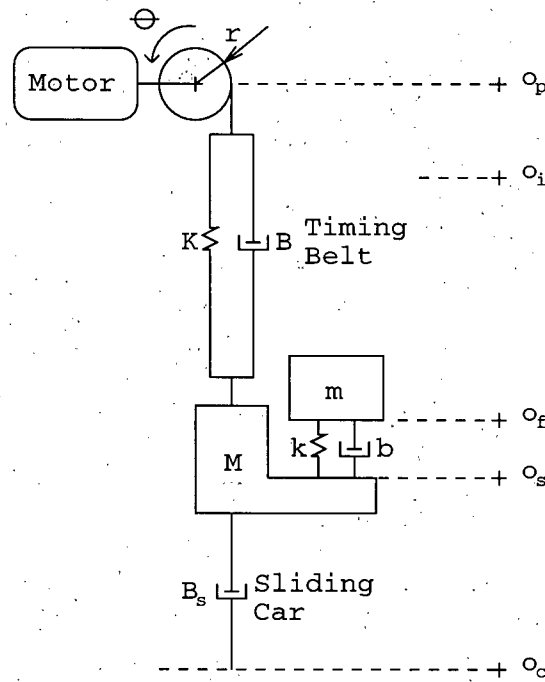


Figure 4.34: Freebody diagram of the coarse fine coupled system.

system. The variables that will be used most often for varying the controllers are kv_{crse} , kp_{crse_iso} , f_n , and ζ . Another variable of interest is ORIENTATION, which can be VERTICAL, HORIZONTAL, or SPACE, depending on the current application. By changing ORIENTATION, variables are initially set to allow the flotor to be levitated.

4.2 Model Development

To develop the model, the freebody diagram in Figure 4.34 will be referenced. It indicates the variables and coordinate systems of interest for model development. All units are S.I., and displacements are measured in the *inertial frame*. The coordinate systems are defined as follows:

o_i – inertial reference

o_c – centre of the I-beam

o_p – position of the pulley linearly

o_s – position of the stator

o_f – position of the flotor

Using these coordinate systems, several variables are defined.

$x_{psd} = o_f - o_s$: value of the position sensing diodes

$x_f = o_f - o_i$: position of flotor from inertial reference

$x_s = o_s - o_c$: value of the position transducer

$x_a = o_c - o_i$: error displacement of the airplane

$r\theta = o_p - o_c$: displacement of the timing belt at the pulley

Since o_i is assigned the inertial reference,

$$o_i = 0$$

$$o_c = x_a$$

$$o_p = r\theta + x_a$$

$$o_s = x_s + x_a$$

$$o_f = x_f$$

$$x_{psd} = x_f - x_s - x_a$$

Using Figure 4.34, the freebody equations of motion can be obtained to develop a simulation model and system transfer functions.

The flotor is a mass suspended above the stator by magnetic forces that effect a spring-damper connection. The force applied to the flotor is

$$F_{fl} = -[b(\dot{o}_f - \dot{o}_s) + k(o_f - o_s)] \quad (4.70)$$

where b and k are the effective damping and spring constants obtained when the flotor is stabilized. The motion of the flotor is given by

$$m\ddot{o}_f = F_{fl} = -b(\dot{o}_f - \dot{o}_s) - k(o_f - o_s) \quad (4.71)$$

$$m\ddot{x}_f = -[b(\dot{x}_f - \dot{x}_s - \dot{x}_a) + k(x_f - x_s - x_a)] \quad (4.72)$$

where m is the mass of the flotor. In the Laplace domain,

$$(k + bs + ms^2)\hat{x}_f = (bs + k)(\hat{x}_s + \hat{x}_a) \quad (4.73)$$

$$A(s)\hat{x}_f = D(s)(\hat{x}_s + \hat{x}_a). \quad (4.74)$$

The main motion of the stator is produced by the motor through the timing belt. The forces acting on the stator are the reaction force from the flotor, any disturbance forces to the system, the sliding friction of the linear bearing car, and the force applied by the timing belt. The force of the timing belt is given by

$$\begin{aligned} F_{tb} &= B(\dot{o}_p - \dot{o}_s) + K(o_p - o_s) \\ &= B(r\dot{\theta} - \dot{x}_s) + K(r\theta - x_s) \end{aligned} \quad (4.75)$$

where B and K identify the mode of the timing belt. The sliding friction is

$$\begin{aligned} F_{sf} &= B_s(\dot{o}_s - \dot{o}_c) \\ &= B_s\dot{x}_s \end{aligned} \quad (4.76)$$

where B_s is the sliding friction constant. The sum of the forces on the stator is

$$F_{st} = -F_{fl} + f_d - F_{sf} + F_{tb} \quad (4.77)$$

which yields the equation of motion

$$\begin{aligned} M\ddot{x}_s &= [b(\dot{x}_f - \dot{x}_s - \dot{x}_a) + k(x_f - x_s - x_a)] + f_d \\ &\quad - B_s\dot{x}_s + [B(r\dot{\theta} - \dot{x}_s) + K(r\theta - x_s)] \end{aligned} \quad (4.78)$$

where M is the mass of the stator. In the Laplace domain, the equation becomes

$$\hat{x}_s [Ms^2 + (b + B_s + B)s + (k + K)] = \hat{f}_d + (\hat{x}_f - \hat{x}_a)(bs + k) + r\hat{\theta}(Bs + K) \quad (4.79)$$

$$G(s)\hat{x}_s = \hat{f}_d + D(s)(\hat{x}_f - \hat{x}_a) + N(s)r\hat{\theta}. \quad (4.80)$$

The torques acting on the pulley are the torque of the motor and the reaction torque of the timing belt. The torque of the motor is characterized by the equation

$$T_l = v_a - b_m \dot{\theta} \quad (4.81)$$

where v_a is the input voltage, I_m is the motor inertia, and b_m is the back emf. The torque of the motor-pulley system is

$$T_m = T_l - rF_{tb} \quad (4.82)$$

and the equation of motion is

$$I_m \ddot{\theta} = v_a - b_m \dot{\theta} - r[B(r\dot{\theta} - \dot{x}_s) + K(r\theta - x_s)] \quad (4.83)$$

The equation becomes

$$\hat{\theta} [I_m s^2 + (b_m + r^2 B)s + r^2 K] = \hat{v}_a + \hat{x}_s r(Bs + K) \quad (4.84)$$

$$P(s)\hat{\theta} = \hat{v}_a + rN(s)\hat{x}_s \quad (4.85)$$

in the Laplace domain.

The system variables need to be estimated for analysis and simulation. For the flotor, the values that will be used during micro-gravity are

$$m = 0.88$$

$$\left. \begin{array}{l} \omega_f = 2\pi 0.1 \\ \rho_f = 0.7 \end{array} \right\} \begin{array}{l} k = \omega_f^2 \\ b = 2\rho_f \omega_f \end{array}$$

which is a soft coupling to the stator. The values for the stator and timing belt are

$$\begin{array}{l} M = 10.0 \\ \left. \begin{array}{l} \omega_s = 2\pi 60 \\ \rho_s = 0.5 \end{array} \right\} \begin{array}{l} K = \omega_s^2 \\ B = 2\rho_s \omega_s \end{array} \\ B_s = 5 \end{array}$$

with the frequency of the timing belt quite high to represent that the timing belt does not slip over the pulley. The motor system variables are

$$I_m = 0.05$$

$$b_m = 0.3$$

$$r = 0.0025$$

where the back emf was estimated from horizontal test runs.

4.3 Open Loop System Analysis

For stability analysis of the system, the notation defined previously as

$$A(s) = ms^2 + bs + k \quad (4.86a)$$

$$D(s) = bs + k \quad (4.86b)$$

$$G(s) = Ms^2 + (B_s + B + b)s + (K + k) \quad (4.86c)$$

$$N(s) = Bs + K \quad (4.86d)$$

$$P(s) = I_m s^2 + (r^2 B + b_m)s + r^2 K \quad (4.86e)$$

can be used to develop open loop transfer functions for the system. Manipulating these, the transfer functions can be derived as

$$\hat{x}_s = \frac{1}{APG(s) - r^2N^2A(s) - PD^2(s)} [(D - A)PD(s)\hat{x}_a + AP(s)\hat{f}_d + rNA(s)\hat{v}_a] \quad (4.87)$$

$$\hat{x}_f = \frac{1}{APG(s) - r^2N^2A(s) - PD^2(s)} [(PG - PD - r^2N^2)D(s)\hat{x}_a + DP(s)\hat{f}_d + rND(s)\hat{v}_a]. \quad (4.88)$$

Letting

$$E(s) = APG(s) - r^2N^2A(s) - PD^2(s) \quad (4.89)$$

the open loop equations can be put into matrix form as

$$\begin{bmatrix} \hat{x}_s \\ \hat{x}_f \end{bmatrix} = \frac{1}{E} \begin{bmatrix} AP & rNA & PD(D - A) \\ DP & rND & D(PG - PD - r^2N^2) \end{bmatrix} \begin{bmatrix} \hat{f}_d \\ \hat{v}_a \\ \hat{x}_a \end{bmatrix} \quad (4.90)$$

The stability of the open loop system will be examined using Nyquist criteria and plots. There are no right half plane poles in the system. The plots from the inputs v_a and f_d show stability over a very large gain margin. The plots from the input x_a are shown in Figure 4.35. These plots indicate that the flotor is stable for all gain values and the stator has a gain margin of 1250. Thus, the system is anticipated to be stable for all inputs.

4.4 Closed Loop System Analysis

For closed loop analysis, the controller in the computer must be defined. The stator is to follow the flotor's displacement from the centre of the workspace, given by the signal x_{psd} . To ensure the stator doesn't gain too much speed and overshoot the centre position, velocity damping will be included as well. The output of the computer will be defined as

$$v_a = K_p x_{psd} - K_v \dot{x}_s \quad (4.91)$$

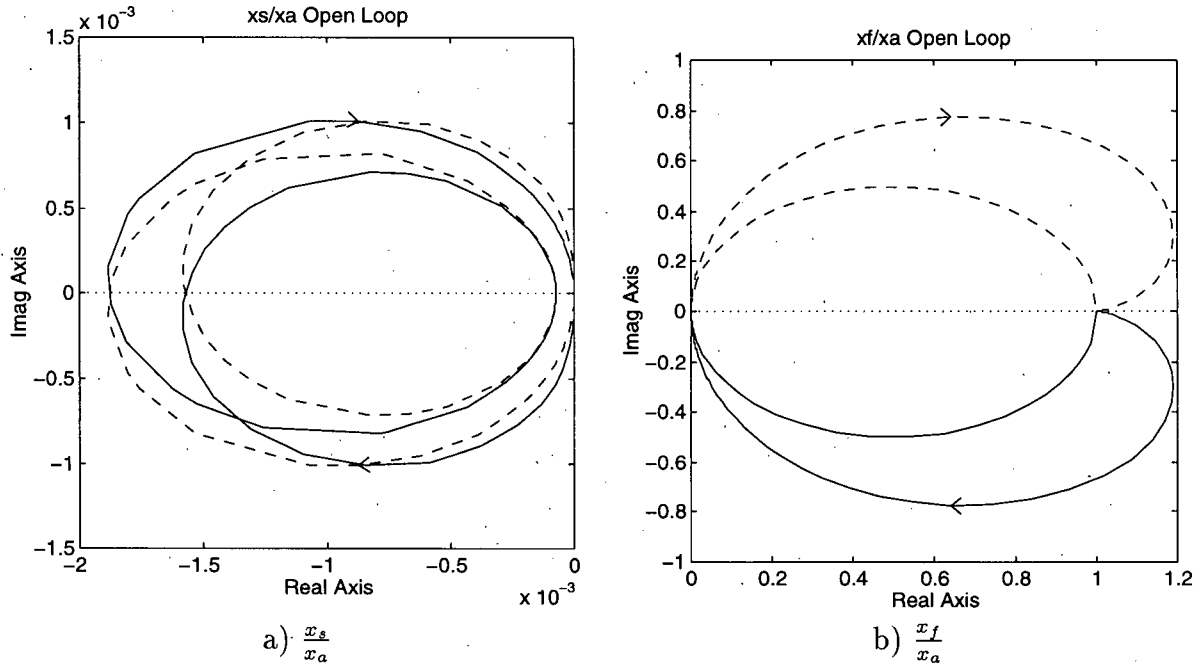


Figure 4.35: Nyquist plots showing open loop stability of the system to airplane vibrations.

where K_p and K_v are the proportional and velocity constants respectively. Since the value of x_{psd} is in the millimetre range, the proportional constant will be quite large. Putting the voltage into the open loop equations (4.87) and (4.88), the closed loop system transfer functions can be derived in the Laplace domain as

$$\hat{x}_s = \frac{1}{E + rNK_p(A - D) + rNAK_v s} [AP\hat{f}_d + (rNK_p + PD)(D - A)\hat{x}_a] \quad (4.92)$$

$$\hat{x}_f = \frac{1}{E + rNK_p(A - D) + rNAK_v s} [DP\hat{f}_d + D(PG - PD - r^2N^2 + rNK_v s)\hat{x}_a] \quad (4.93)$$

where E is $E(s)$ as defined previously. The frequency response of these equations to airplane motion x_a for $K_p = 1200$ and $K_v = 15$ is shown in Figure 4.36. The first plot shows that the stator cancels the airplane motion at low frequency and does not respond to high frequency motion. There is a resonant peak in the response of small magnitude that should not affect the system too greatly. The reduction at very low frequency is the

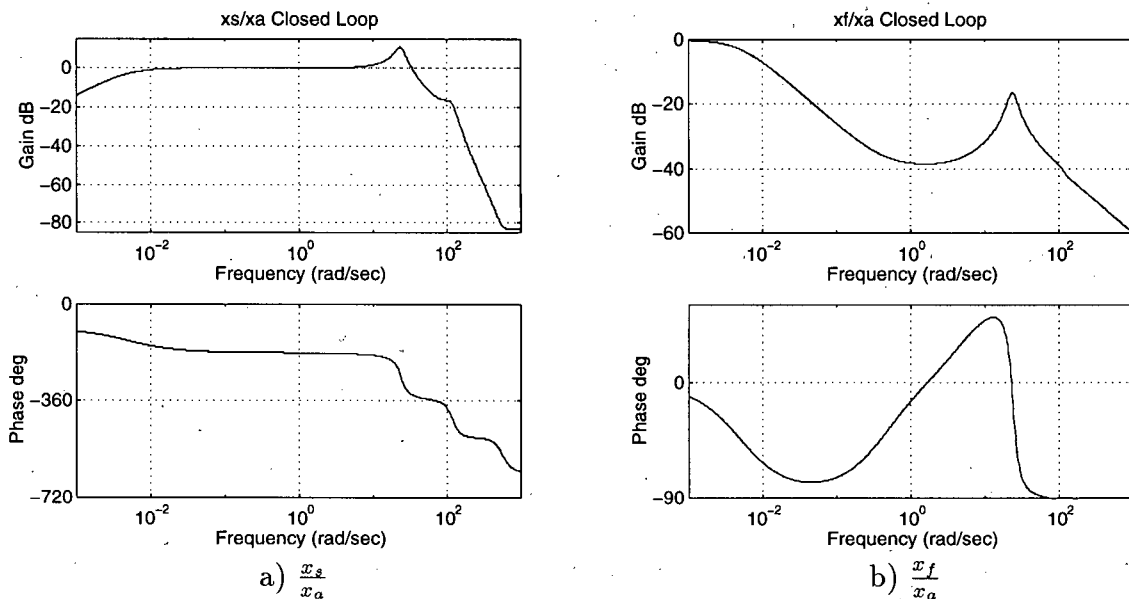


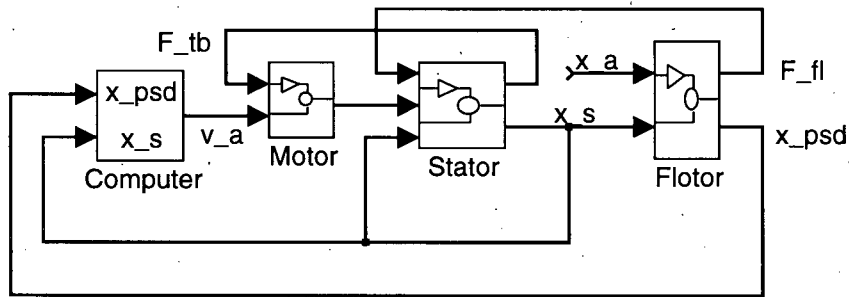
Figure 4.36: Bode plots showing closed loop response of the system to airplane vibrations.

effect of the flotor on the system. As shown in the second plot, the flotor follows very low frequency airplane motions. This is consistent with the desired response of the system.

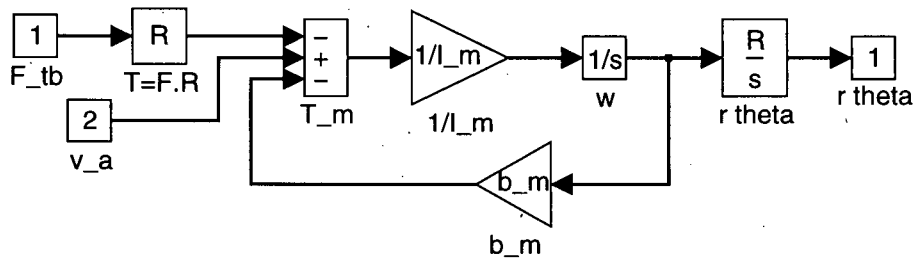
4.5 Simulink Simulations

The equations of motion were developed into a Simulink system, which is shown in Figure 4.37. This model can be used to test the system against various expected input airplane vibrations. Note that in this model, the workspace limits of the flotor and stator have not been included.

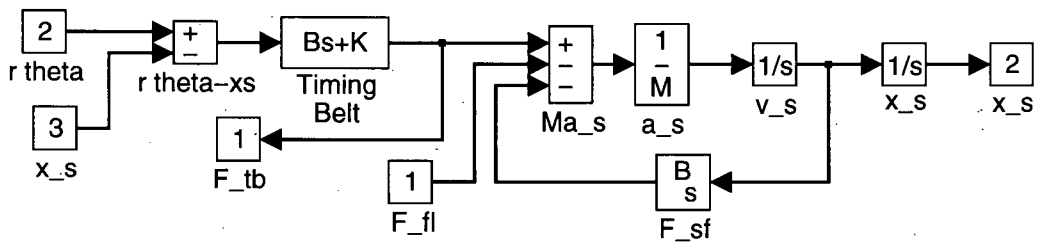
Figure 4.38 shows the results when the model is subjected to a sample of airplane acceleration data. The acceleration levels of the flotor are 100 to 1000 times smaller than the input acceleration and at a frequency of approximately 5 Hz. If this had been an actual test run, the flotor would have hit the workspace limits in under 3 seconds, and the stator exceeded its bounds in under 5 seconds. To stop the flotor from reaching its limits, the stator has to move faster, though the stator would reach its bounds sooner



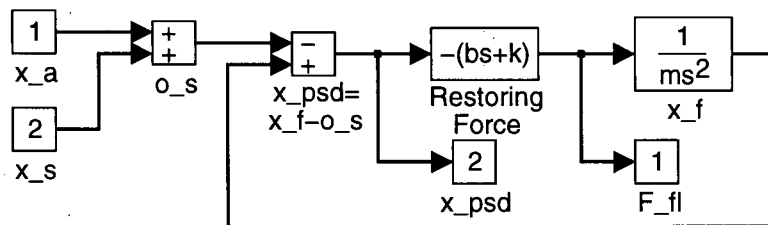
a) Complete system in Simulink



b) Motor block expanded



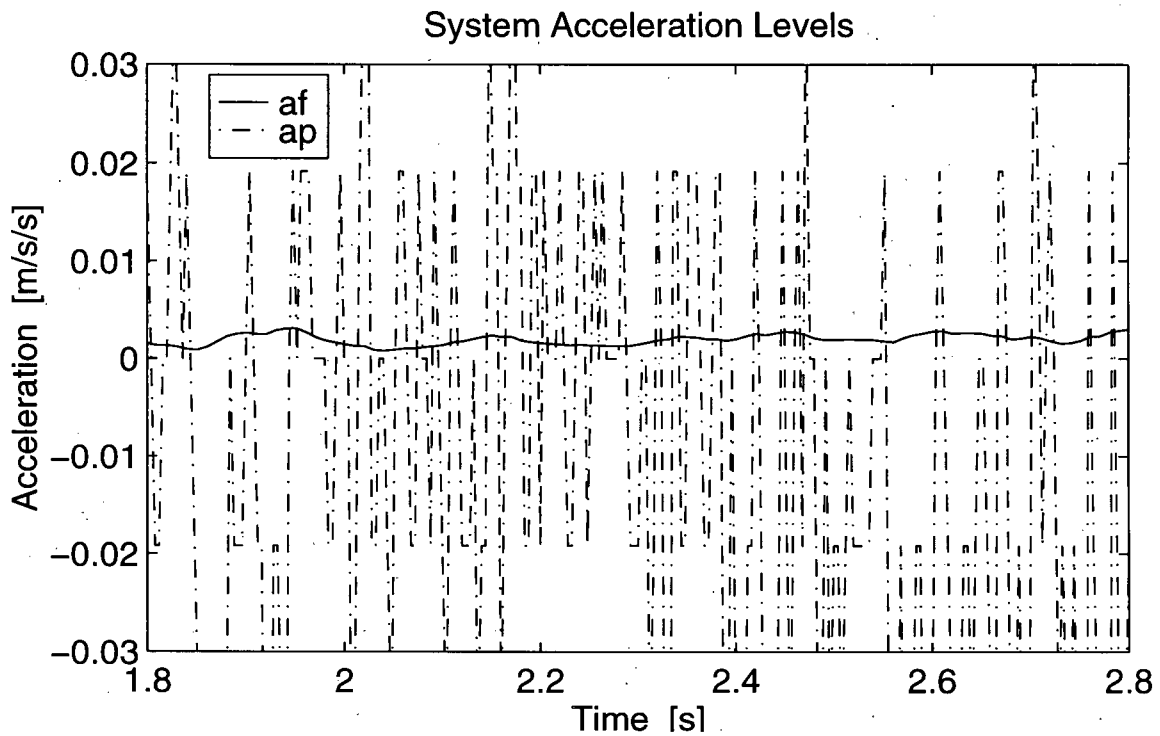
c) Stator block expanded



d) Flotor block expanded

Figure 4.37: Model of the coarse-fine control system.

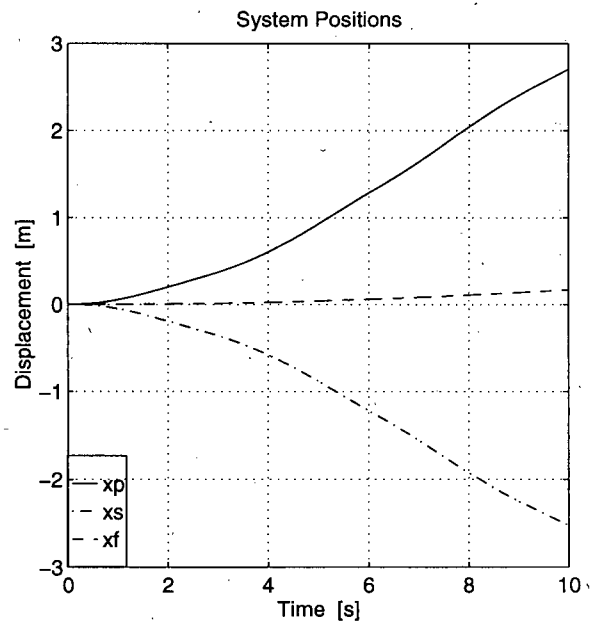
as a result. Figure 4.39 shows the response of the system when the velocity damping of the stator, K_v , is reduced to zero. The flotor in this case stays within its workspace as the stator is able to move faster. The stator exceeds its workspace in under 4 seconds.



a) Sample of acceleration levels of the airplane and flotor.

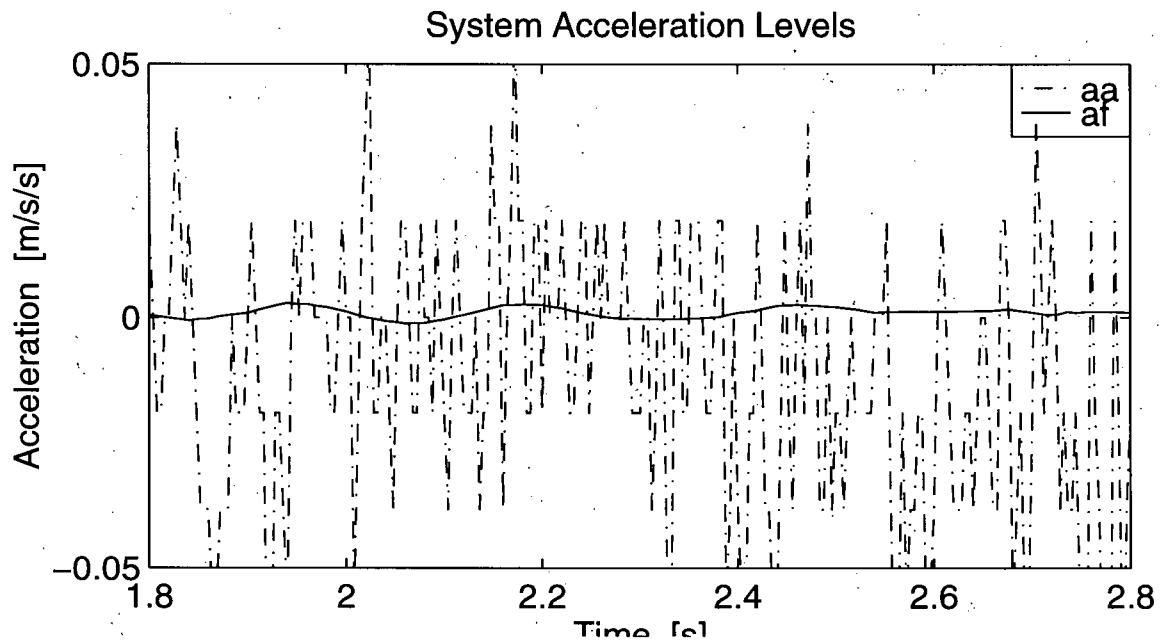


b) PSD signal output.

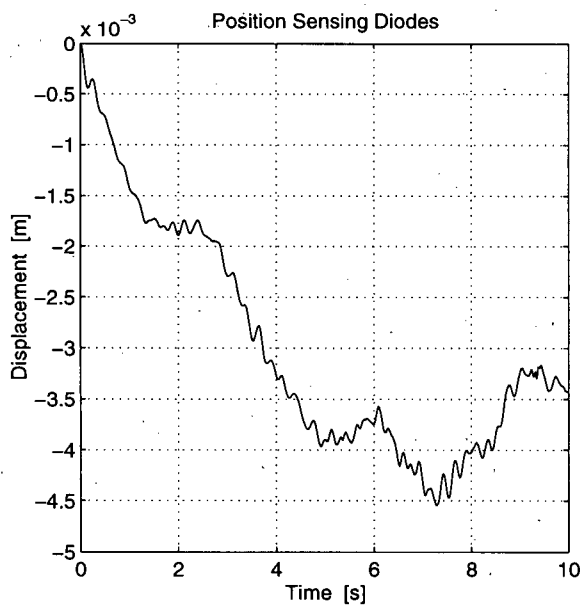


c) Displacements of system elements

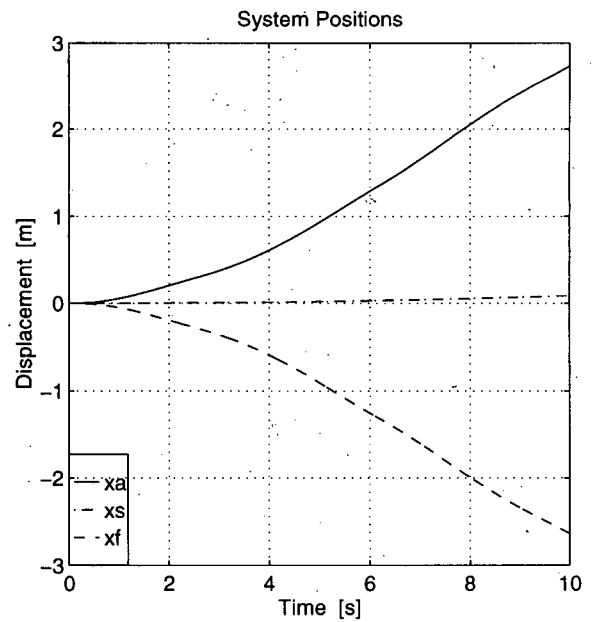
Figure 4.38: Plots showing the simulation response to a sample vibration signal with $K_p = 1200$, $K_v = 15$.



a) Sample of acceleration levels of the airplane and flotor.



b) PSD signal output



c) Displacements of system elements

Figure 4.39: Plots showing the simulation response to a sample vibration signal with $K_p = 1200$, $K_v = 0$.

Chapter 5

Micro-Gravity Testing

This chapter explains briefly about the micro-gravity testing and presents the data from the DC-9 flight. Analysis of data, comparison to simulation predictions, and recommendations for future testing is also presented.

5.1 Installation and Testing

The system was installed on NASA Lewis Research Center's DC-9 to be tested during micro-gravity flights. The I-beam was clamped to a vertical pole in the plane and long wires were used to connect the hardware to the computer, which was situated in a rack with the voltage and current supplies. There were some problems encountered while setting up the system. First, the pole to which the I-beam was attached was very flexible and would add increased vibrations to the system. Another problem was electrical. A ground reference error with the coarse current amplifier had to be fixed.

The first flights were used to judge the response of the flotor in low gravity situations to get an intuitive feel for the bandwidth necessary for successful control. With the coarse stage strapped down and the flotor control bandwidth rather large, data from the system was collected. The signals stored were acceleration of plane, acceleration of flotor, and position of flotor (x_{psd}).

The next step was to release the coarse stage and observe the entire system. A typical micro-gravity run produced variables with the trends shown in Figure 5.40. The acceleration of the plane starts at -9.8 m/s/s and approaches zero. The acceleration

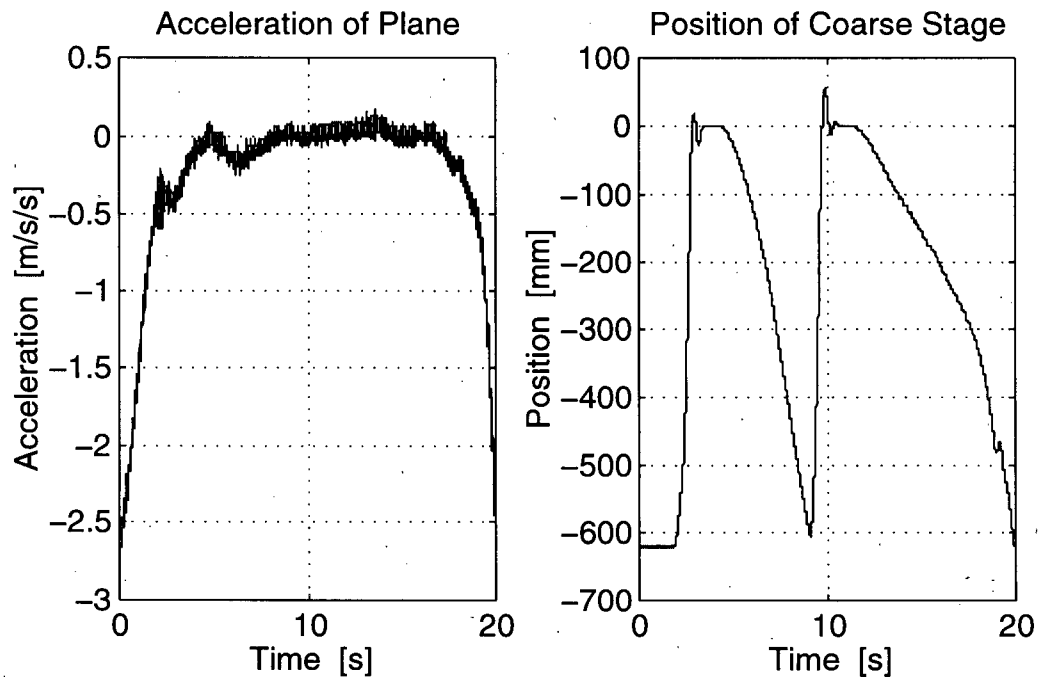


Figure 5.40: Typical parabola cycle.

remains around zero for a time (approximately 20 seconds) until the plane begins its pull up phase. Then the acceleration becomes large negative again. The position of the coarse stage is at the bottom of the I-beam until the acceleration level becomes small enough, at which time the coarse stage is centred. This causes large vibrations and motion on the flotor. When the coarse stage is centred and the acceleration of the plane remains small enough, the coarse stage is controlled to follow the flotor. Control continues until the coarse position approaches the edge of the workspace, at which time the coarse stage is centred along the I-beam again, or until the acceleration level of the plane becomes too large, then the coarse stage is returned to the base of the I-beam.

Several things were attempted during flights to control the system. The effect of a dead band switch on flotor position was investigated as well as different gains for the system. All controllers could not be tested due to a memory error with the DSP board.

The ambient weather conditions were rougher than normal during the testing on the DC-9. This caused larger amplitude vibrations and also increased the low frequency errors. As a result, the coarse stage reached the workspace limits quicker than would be expected under average conditions.

5.2 Results

The data for the wrist only experiment (when the coarse stage was strapped down) was plotted and compared to simulation predictions. The comparisons are shown in Figure 5.41 and indicate very good agreement between theory and experiments for the wrist. The difference between actual and simulation data comes as a result of a steady state force on the flotor, which is set when the flotor position is reset to the centre of the workspace. Since each parabola has different acceleration characteristics, this steady state force is not correct for all instances, but provides a good starting force to near centre the wrist. Indeed, the first graph shows the simulation is a constant 0.2 mm off the actual data, which is the effect of an extra steady state force. The second set of data has a better centred wrist and the simulation and data are in good agreement.

Some of the data collected when the coarse stage was controlled to follow the flotor is shown in Appendix E. The first three show control for the parameters $f_n = 0.2$, $k_p = 80$ and $k_v = 1$ with the coarse controller only in effect when the flotor position exceeds ± 1 mm, a dead band. The position of the flotor vibrates greatly, due to the large coarse control signal constantly turning on and off as the flotor vibrates around the 1 mm mark. This was verified later on the model in simulation. The dead band was not included in the simulation model since its effect was underestimated.

The dead band was then removed from the digital controller and tracking was attempted again. The next three graphs in the Appendix show the data collected for the

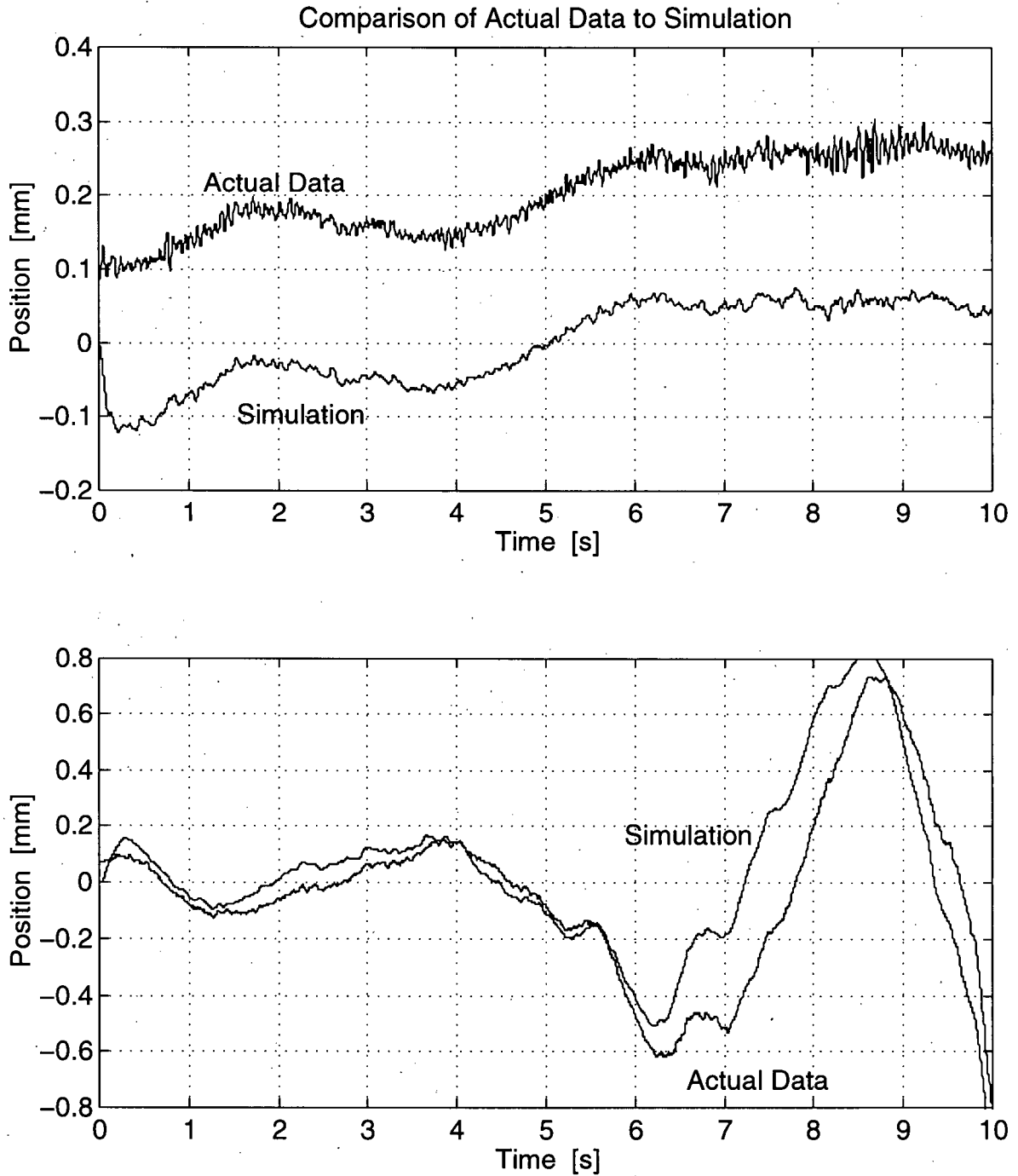


Figure 5.41: Comparison of actual data to simulation of wrist. In the top graph, $f_n = 5$, the lower $f_n = 2$.

same values for the variables. Again the flotor position is oscillatory, but not as much as the previous attempt, and not always. At first it was thought that the problem was due to initial conditions the flotor acquired rapidly being centred on the I-beam. The velocity constant was increased to limit the centering speed, but this did not improve the flotor response.

The velocity constant was then set to zero and the response of the system improved greatly. However, modifications to the control code increased the size of the compiled file to beyond that available on the DSP board and memory allocation errors were occurring. As a result, the response of the system was inconsistent and the data was unreliable. Some data can be analyzed for trends but no concrete conclusions can be drawn.

5.3 Analysis

Figure 5.42 shows plots of data collected during one parabola that the system behaved relatively as desired. The variables for this parabola were $f_n = 0.1$ and $kp_crse_iso = 50$. At the start of the micro-gravity phase the acceleration of the flotor is much smaller than the acceleration of the plane. The magnet levitation system has removed the slow oscillations and attenuated by more than a factor of two the high frequency noise. The coarse stage has a slow downward drift, changing 200 mm in just over 7 seconds, and the flotor position is negative. This agrees with the acceleration of the plane which is more negative at the beginning of the parabola. After time approximately 12 seconds, the acceleration of the plane tends to be more positive and the flotor position confirms this by becoming positive as well. The coarse stage begins to move rapidly upwards following the flotor and finally hits the workspace limits. During this part of the parabola the flotor acceleration degrades and shows the action-reaction effect of the stator on the flotor, indicating that a lower bandwidth is still required for the system to have greater

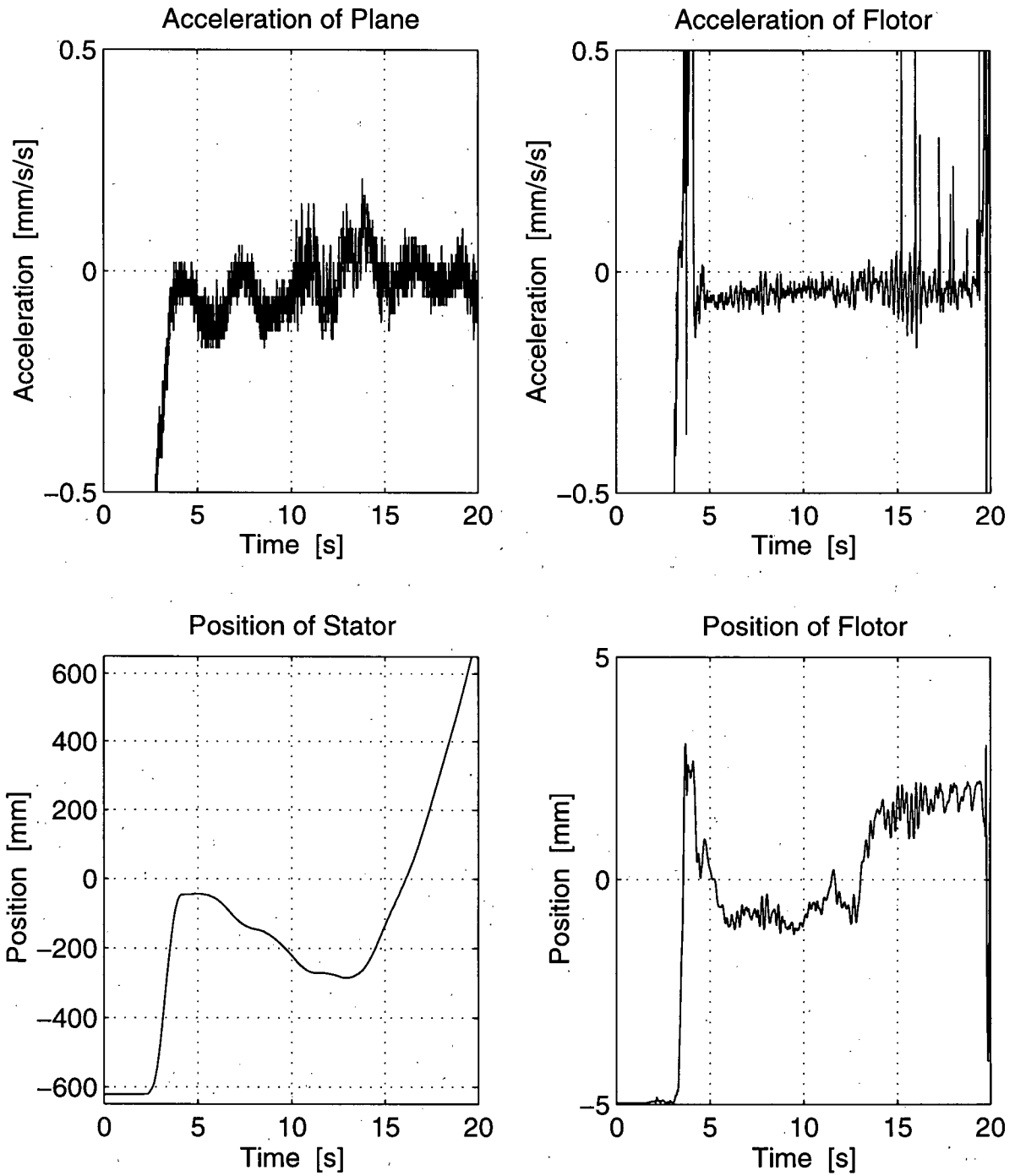


Figure 5.42: Data plots for parabola number 50 on day 4. The flotor acceleration is considerably less than the plane acceleration while the flotor position is near centre.

effectiveness.

The response of the system during micro-gravity parabola is in disagreement with the system model. There are several things that may contribute to this, both linear and non-linear considerations.

The acceleration due to gravity, while small, is not zero and will cause the flotor and stator to have disturbance forces. For effective vibration isolation, a small w_f is necessary for the flotor, and the disturbance will have a larger effect on the system. The acceleration changes direction rapidly. This either increases or decreases the power necessary to move the coarse stage by the motor. For example, if the desired coarse motion is negative, and the force due to gravity is also negative, the static friction of the bearings is much easier to overcome. However, if the force due to gravity is positive, then a much larger signal is necessary to overcome both static friction and this positive force. This unmodelled force, which is a function of the acceleration of the plane, can be found and added to the model.

The timing belt for the coarse stage also introduces unmodelled effects. The belt is stretched between two pulleys and has a small amount of elasticity and a large amount of flexibility. The belt has several vibration modes at low frequency that cause perturbations on the system, the most significant one at 7 Hz. This effect will cause oscillations in the coarse position when the coarse motion is not steady.

There are non-linear effects to consider as well. The MAGLEV wrist, being a smaller version of it, will have similar concerns as the LMIM. This includes acting as an inverted pendulum due to the magnetic non-linearities. This was not included in the model since the effect was expected to be small. Also, the hard contact the flotor experiences as it hits the edge of its workspace has not been modelled, but is not important if x_{psd} remains within acceptable limits.

While the timing belt has known vibration nodes, these can not simply be modelled

as a spring-damper connection with a 7 Hz bandwidth – there is a maximum stretch the timing belt can experience. If no maximum stretch is considered and the timing belt frequency reduced, the system simulation becomes unstable as x_s oscillates with increasing magnitude and does not follow $r\theta$, which it must. No effective way of modelling the maximum stretch was found.

Another non-linear consideration is that of static friction of the linear bearing car on the rail, which is in addition to sliding friction. The static friction causes the linear bearing car to remain stationary until sufficient force is applied. When it does start to move, the friction force is reduced and the stator moves faster than necessary, overshooting the desired response. Then the stator stops briefly as the flotor catches up and passes the stator once again. The stator must once again overcome the static friction, and continues this jerky motion.

Attempts to model these effects to verify their effect proved difficult, in particular the maximum stretch of the belt. A rough approximation of the non-linear timing belt with a lower vibration frequency was modelled and added to the simulation. As well, an approximation of the static friction was included in the new model. Figure 5.43 shows the comparison between actual data and simulation using the same airplane acceleration signal. While the simulation does not exactly match the observations on the plane, the behaviour of the simulation is similar to actual data. Therefore, using coarse control with a flexible timing belt and a sliding car produces undesired oscillations.

5.4 Recommendations for Future Study

Recommendations for future work with the coarse-fine tracker to improve the system:

- Use a different coarse motion system.

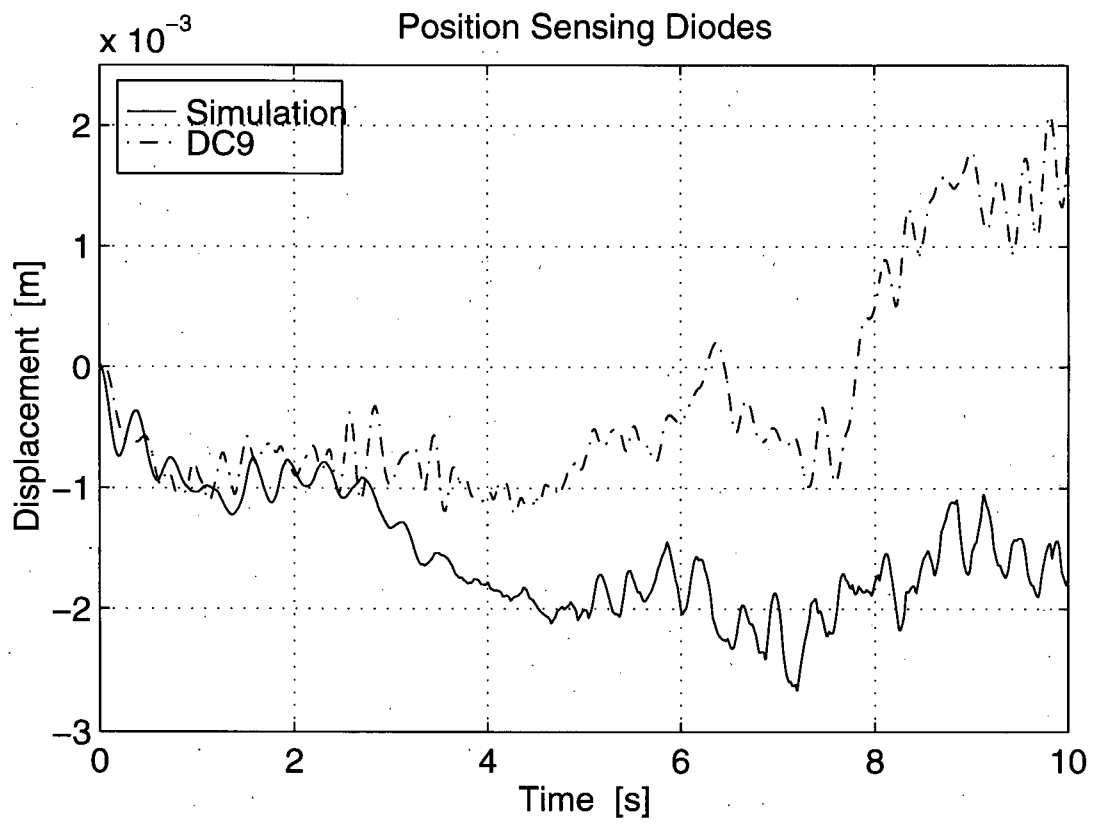


Figure 5.43: Comparison of data and simulation with low frequency mode for the timing belt and static friction for the sliding car.

- To remove initial conditions of the flotor the stiffness should be quite high when the coarse stage is being centred. This way the flotor will converge to the centre of its workspace quickly instead of being pushed around at the beginning.
- Use previous data to predict the initial acceleration levels and provide beneficial initial conditions to the flotor. For example, if the acceleration is drifting positive during the centering mode, a negative velocity could be added to the flotor to extend the length of time the system stays in the tracking mode, thus longer improved micro-gravity time.
- The stiffness of the wrist can be increased as the flotor approaches the edge of the rattle space to give the flotor a centering velocity before hitting the edge. This becomes a tradeoff between hitting the edge of the rattle space and allowing greater transmission of vibrations.
- The control output to the motor could be an increasing centering force as the coarse stage nears the edge of the I-beam. Again, it depends if a swift movement to the centre of the workspace, as is the case presently, is a better option than transmitting greater vibrations or forcing the flotor to hit the edge of the rattle space.

Chapter 6

Conclusions

Magnetic levitation technology using Lorentz forces is a good method for isolating applications from external vibrations and acceleration disturbances. The LMIM platform, designed under contract at UBC, and the smaller version known as the wrist use this theory to create a non-contact system for vibration isolation.

This thesis looked at the LMIM and wrist and explained briefly how Lorentz theory has been applied to create the non-contact technology. An accurate model of the LMIM was developed for possible use in designing controllers. The identified plant had an unstable pole and confirmed the mass of the flotor to be approximately 22 kg. The LMIM system acts as an inverted pendulum and it was difficult to adequately control the system with this problem.

Using the LMIM for testing, H_∞ control techniques were employed to actively control the system. Several assumptions were made on the LMIM model to facilitate controller design.

The H_∞ control theory proved difficult to design with. Solutions to the H_∞ control problem do not always exist which forces an iterative procedure to finding answers. The poles of the LMIM plant also contributed problems to the design of a successful controller, as Bode's Integral theorem must be satisfied. The effect of the weights on controller design was studied and weight selection insight was provided. Some successful position controllers were developed with bandwidth of the closed-loop system near 3 Hz that stabilized the LMIM. Further reduction of the bandwidth was not possible with

the position controller. Adding acceleration feedback was straight-forward in theory, but design solutions were difficult. Acceleration feedback controller testing on the LMIM was unsuccessful.

The controllers that worked in practice showed good disturbance attenuation for position control. There is one important point when adding acceleration feedback. With H_∞ theory the solution does not always exist, but if one does it is shaped as expected and gives the desired closed-loop response.

The wrist was used in a coarse-fine tracking approach to vibration isolation in a micro-gravity environment. A model of the wrist was developed and was in good agreement with actual responses to noise. Simple PID control was employed for the wrist with the coarse stage tracking the flotor position in a DC-9 performing parabolic flights. The data collected showed effects not included in the model of the coarse stage play a significant role in the system. The data also showed disturbance attenuation while tracking the flotor was possible but requires further testing.

Bibliography

- [1] J. Yan, "Design and Control of a Bilateral Motion-Scaling System Using Magnetic Levitation," Master's thesis, University of British Columbia, March 1994.
- [2] J.C Doyle, K. Glover, P.P. Khargonekar, and B.A. Francis, "State-Space Solutions to Standard H_2 and H_∞ Control Problems," *IEEE Trans. Automatic Control*, vol. AC-34, pp. 831-847, 1989.
- [3] J.M. Maciejowski, *Multivariable Feedback Design*. New York: Addison-Wesley, 1989.
- [4] R.M. Alexander, C.H. Gerhold, C.B. Atwood, and J.F. Cordera, "Vibration Isolation in a Microgravity Environment," *J. of Vibration and Acoustics*, vol. 115, no. 4, pp. 477-483, Oct. 1993.
- [5] L.A. Sievers, and A.H. von Flotow, "Linear Control Design for Active Vibration Isolation of Narrow Band Disturbances," *Proc. of IEEE Conf. on Decision and Control*, vol. 2, pp. 1032-1037, 1988.
- [6] N. Tanaka, Y. Kikushima, "Optimal Design of Active Vibration Isolation Systems," *Trans. of ASME Journ. of Vibration, Acoustics, Stress, and Reliability in Design*, vol. 110, no. 1, pp. 42-48, 1988.
- [7] N.G. Fitz-Coy, and J.Jang, "Active Vibration Isolation of a Space Platform: A Game Theoretic Approach," *Advances in the Astronautical Sciences*, vol. 85, pt. 3, pp. 2199-2110, 1993.
- [8] S.E. Salcudean, H. Davis, C.T. Chen, D.E. Goertz, and B.V. Tryggvason, "Coarse-Fine Residual Gravity Cancellation System with Magnetic Levitation," *Proc. of IEEE Conf. on Robotics and Automation*, pp. 1641-1647, 1992.
- [9] Z.J. Geng and L.S. Haynes, "Six Degree-of-Freedom Active Vibration Control Using the Stewart Platforms," *IEEE Trans. on Control Systems Tech.*, vol. 2, no. 1, pp. 45-53, 1994.
- [10] S. Li and R. Barron, "Control Strategies in the Active Isolation of Engineering Systems," *IEE Conf. on Control*, pp. 405-410, 1990.
- [11] A.P. Allan and C.R. Knospe, "A Six Degree-of-Freedom Magnetic Bearing for Microgravity Vibration Isolation," *NASA Conference Pub. 3152 - Int. Symp. on Magnetic Suspension Technology*, pp. 209-218, 1991.

- [12] R.D. Hampton, C.R. Knopse, C.M. Grodsinsky, P.E. Allaire, and D.W. Lewis, "Microgravity Vibration Isolation: Optimal Preview and Feedback Control," *NASA Technical Memorandum n. 105673*, p. 24, May 1992.
- [13] "Users Guide for NASA Lewis Research Center DC-9 Reduced-Gravity Aircraft Program," *NASA Technical Memorandum n. 106755*, January 1995.
- [14] R.L. Hollis and S.E. Salcudean, "Lorentz Levitation Technology: A New Approach to Fine Motion Robotics, Teleoperation, Haptic Interfaces, and Vibration Isolation," *Proceedings of the 5th International Symposium on Robotics Research*, 18 pages, October 1993.
- [15] K. Youcef-Toumi and T.J. Yeh, "Dynamics and Control of High Precision Magnetically Levitated Vibration Isolation Systems," *Proc. of American Control Conference*, vol. 4, pp. 2770-2774, 1992.
- [16] N. Parker, S. Salcudean, and J. Boulet, "Vibration Isolation with Active Magnetic Suspension," report for DSS contract 9F008-4-0001/01-SW, 140 pages, April 1996.
- [17] B.V. Tryggvason, S.E. Salcudean, W.Y. Stewart and N. Parker, "Microgravity Vibration Isolation Mount," *24th Int. Conf. on Environmental Systems and 5th European Symposium on Space Environmental Control Systems*, 1994.
- [18] K.A. Logsdon, C.M. Grodsinsky, and G.V. Brown, "Development of a Vibration Isolation Prototype System for Microgravity Space Experiments," *NASA Technical Memorandum n. 103664*, p. 8, June 1990.
- [19] C.M. Grodsinsky, "Development and Approach to Low-Frequency Microgravity Isolation Systems," *NASA Technical Paper 2984*, August 1990.
- [20] J.S. Freudenberg, and D.P. Looze, "Right Half Plane Poles and Zeros and Design Tradeoffs in Feedback Systems," *IEEE Trans. on Automatic Control*, vol. 30, no. 6, pp. 555-565, June 1985.
- [21] J.S. Freudenberg, and D.P. Looze, "An Analysis of H^∞ -Optimization Design Methods," *IEEE Trans. on Automatic Control*, vol. 31, no. 3, pp. 194-200, March 1986.
- [22] E. Polak, S.E. Salcudean, "On the Design of Linear Multivariable Feedback Systems Via Constrained Nondifferentiable Optimization in H^∞ Spaces," *IEEE Trans. on Automatic Control*, vol. 34, no. 3, pp. 268-276, March 1989.
- [23] M. Green, and D.J. Limebeer, *Linear Robust Control*. Englewood Cliffs, N.J:Prentice Hall, 1995.

- [24] J.C. Doyle, B.A. Francis, and A.R. Tannenbaum, *Feedback Control Theory*. New York:MacMillan Publishing, 1992.
- [25] R.Y. Chiang, and M.G. Safoniuk, *Robust Control Toolbox User's Guide*. Natick, Mass.:The MathWorks Inc., 1992.
- [26] R.C. Dorf, *Modern Control Systems*. Addison-Wesely Publishing Company, 1992.
- [27] A. Grace, A.J. Laub, J.N. Little, and C.M. Thompson, *Control System Toolbox User's Guide*. Natick, Mass.:The MathWorks Inc., 1992.
- [28] D.I. Jones, A.R. Owens, and R.G. Owen, "A Control System for a Microgravity Isolation Mount," *IEEE Trans. on Control Systems Technology*, vol. 4, no. 4, pp. 313-325, July 1996.
- [29] N. Parker, and S.E. Salcudean, "Vibration Isolation with Active Magnetic Suspension," report for DSS contract 9F007-2-0321/01-SR, 37 pages, April 5, 1993.
- [30] N. Parker and S.E. Salcudean, "Design of a Magnetically Levitated Isolation Mount for the KC-135," report for DSS contract 9F007-2-6076/01-SW, 47 pages, February 25, 1994.
- [31] C.T. Chen, and S.E. Salcudean, "Computer Simulation of a Proposed 6-DOF Residual Gravity Cancellation System," report for DSS contract, 9F007-2-6024/01-SS, 31 pages, November 11, 1992.
- [32] R.L. Hollis, S. Salcudean, and A.P. Allan, "A Six Degree-of-Freedom Magnetically Levitated Variable Compliance Fine Motion Wrist," *Robotics Research: 4th Int'l Symp. On Robotics Research*, pp. 65-73, August 1987.
- [33] R.L. Hollis, S. Salcudean, and A.P. Allan, "A Six Degree-of-Freedom Magnetically Levitated Variable Compliance Fine Motion Wrist: Design, Modeling, and Control," *IEEE Transactions on Robotics and Automation*, vol. 7, pp. 320-332, June 1991.
- [34] R.L. Hollis, and S.E. Salcudean, "Input/Output System for Computer User Interface Using Magnetic Levitation," *U.S. Patent No. 5,146,566*, September 8 1992.
- [35] C.E. Rudinger, C.J. Harris, and P.C. Dolkas, "Special Considerations in Outfitting a Space Station Module for Scientific Use," *Proc. 16th ICES Conf. Aerospace Environmental Systems*, pp. 427-433, July 1986.
- [36] C.M. Grodinsky, and G.V. Brown, "Low Frequency Vibration Isolation Technology for Micro-Gravity Space Experiments," *Proc. Machinery Dynamics - Applications and Vibration Control*, pp. 295-302, September 1989.

- [37] B.V. Tryggvason, B.Y. Stewart, H.R. Davies, and S.E. Salcudean, "Development of a Large Motion Vibration Isolation Mount for the KC-135: Summary of Flight Tests to Date," *Spacebound '92 Workshop*, May 1992.
- [38] S. Salcudean, H. Davis, C.T. Chen, D.E. Goertz, and B. Tryggvason, "Coarse-Fine Residual Gravity Cancellation System with Magnetic Levitation," *Proc. of IEEE Int'l Conf. on Robotics and Automation*, May 1992.
- [39] M.R. Milligan, "PSD, LED and Signal Conditioning Setup and Calibration Documentation," techn. rep., Dept. of Electrical Engineering, University of British Columbia, November 1993.
- [40] P.C. Sen, *Principles of Electric Machines and Power Electronics*. New York: John Wiley & Sons, 1989.
- [41] C.W. deSilva, *Control Sensors and Actuators*. Englewood Cliffs, NJ: Prentice-Hall, 1989.

Appendix A

H_∞ Theory Notes

A.1 Augmented Plant

The augmented plant, $P(s)$, is the transfer matrix from w and u to z and y

$$\begin{bmatrix} z \\ y \end{bmatrix} = P(s) \begin{bmatrix} w \\ u \end{bmatrix} \quad (\text{A.94})$$

$$\begin{bmatrix} z \\ y \end{bmatrix} = \begin{bmatrix} P_{11}(s) & P_{12}(s) \\ P_{21}(s) & P_{22}(s) \end{bmatrix} \begin{bmatrix} w \\ u \end{bmatrix}. \quad (\text{A.95})$$

Knowing $u = K(s)y$ the transfer function between z and w is

$$T_{zw}(s) = P_{11}(s) + P_{12}K(s)(I - P_{22}K(s))^{-1}P_{21}(s). \quad (\text{A.96})$$

The augmented plant is most often represented in state-space form

$$\begin{bmatrix} \dot{x} \\ z \\ y \end{bmatrix} = \begin{bmatrix} A & B_1 & B_2 \\ C_1 & D_{11} & D_{12} \\ C_2 & D_{21} & D_{22} \end{bmatrix} \begin{bmatrix} x \\ r \\ u \end{bmatrix}, \quad (\text{A.97})$$

which can be found by converting the transfer matrix to state space, *i.e.*

$$P(s) \Rightarrow \left(A, \begin{bmatrix} B_1 & B_2 \end{bmatrix}, \begin{bmatrix} C_1 \\ C_2 \end{bmatrix}, \begin{bmatrix} D_{11} & D_{12} \\ D_{21} & D_{22} \end{bmatrix} \right)$$

where the notation (A, B, C, D) is the state space representation of the transfer function

$$T(s) = D + C(sI - A)^{-1}B. \quad (\text{A.98})$$

The B_i , C_i , and D_{ij} matrices must be partitioned to reflect the number of external inputs, control inputs, control outputs and measured outputs.

A.2 Stabilizable and Detectable

These are defined as [3], [25]

- (A, B) is *stabilizable* if the uncontrollable modes are stable.
- (A, C) is *detectable* if the unobservable modes are stable.

The uncontrollable and unobservable modes can be determined using the theorems

- (A, B) is controllable if the rank of $[(sI - A) B]$ is equal to the size of A for all s .

The values of s where this is not true are the uncontrollable modes.

- (A, C) is observable if the rank of $\begin{bmatrix} (sI - A) \\ C \end{bmatrix}$ is equal to the size of A for all s .

The values of s where this is not true are the unobservable modes.

A.3 Plant Transformations

A.3.1 Axis Shifting

With axis shifting the idea is to shift all the poles of the plant a small amount before the design is run, and then after a successful design is achieved, to shift the poles back. This can be thought of as shifting the iw -axis back and forth. The pole shifting can be done with the transform on the A matrix of the plant state space

$$A = A + \varepsilon I \quad (\text{A.99})$$

where I is the identity matrix of same dimension as A . This is the same as shifting the iw -axis by ε units to the left. Shifting the axis to the left puts the poles in the RHP, *i.e.*

makes the plant unstable. This is required as a consequence of H_∞ theory, which will place the closed loop poles of the successful design in the LHP. By shifting the axis left, one insures that the poles remain in the LHP when the axis is shifted back. If the axis was shifted right, any closed loop poles with value less than ϵ will be in the RHP after the axis is shifted back.

The proper choice of ϵ is essential for determining the closed loop poles of the system. H_∞ design theory will not design unstable systems, nor marginally stable ones. Therefore, the smallest pole of the system will be larger than ϵ . This smallest pole also dictates the response of the system. Obviously, ϵ must be less than the desired bandwidth so that the designed controller is able to react fast enough. At the same time, ϵ can not be too small or the plant matrix may get badly conditioned. The choice of ϵ is critical in the system design – it dictates the smallest allowable pole in the closed loop response.

A.3.2 Bilinear Transform

In bilinear transform [25], as with the axis shifting, the controller will be designed for the transformed plant, and then the solution is transformed back into the original plane.

The bilinear transform takes the form

$$s = \frac{\alpha z + \delta}{\gamma z + \beta} \quad (\text{A.100})$$

and the inverse transform is

$$z = \frac{\delta - \beta s}{\gamma s - \alpha} \quad (\text{A.101})$$

A special form of the transform maps the jw -axis to a circle and a circle to the new jw -axis, as shown in Figure A.44. This operation has the form

$$s = \frac{z + p_1}{\frac{z}{p_2} + 1} \quad (\text{A.102})$$

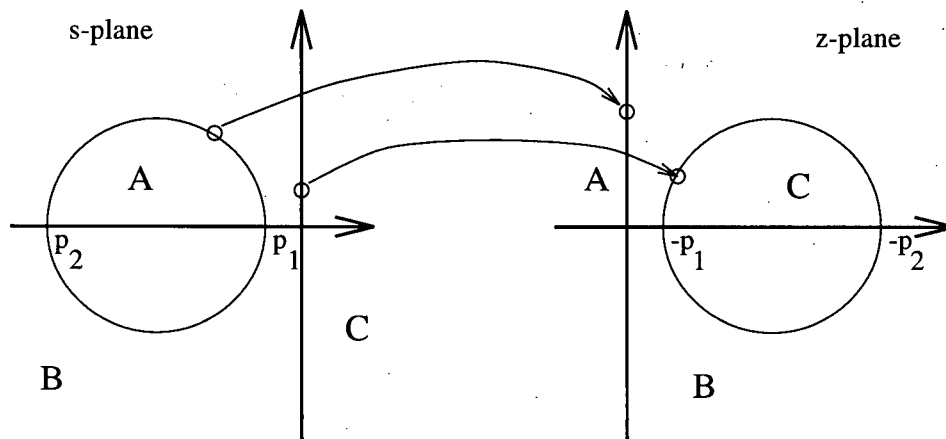


Figure A.44: Special form of the bilinear transform that maps the $j\omega$ -axis to a circle.

so that $\alpha = 1$, $\delta = p_1$, $\gamma = \frac{1}{p_2}$, and $\beta = 1$. When $p_2 = \infty$ ($\gamma = 0$), this becomes the simple axis shifting and gives the same results as previous.

The choice of locations of p_1 and p_2 are important since they limit the placements of the closed loop poles. p_2 affects the high frequency response of the system. p_1 determines the dominant poles of the closed loop system since the controller designed in the z -plane will have its poles in the LHP, which is inside the circle (region A) when transformed back. All poles of the designed closed loop system are in the circle, so the size and location of it directly determines the possible configuration of the closed loop system. Choosing it too small or in a bad position could result in a solution with totally unacceptable results.

Appendix B

Nomenclature

Based on the closed loop shown in Figure B.45, the following nomenclature is used.

Position Plant

$$G_x = \frac{1}{ms^2 - H} \quad (\text{B.103})$$

Acceleration Plant

$$G_a = \frac{s^2}{ms^2 - H} \quad (\text{B.104})$$

Position Plant with Acceleration Feedback

$$G_{xa} = \frac{K_x}{ms^2 - s^2 K_a - H} \quad (\text{B.105})$$

Acceleration Plant with Position Feedback

$$G_{ax} = \frac{s^2 K_a}{ms^2 - H + K_x} \quad (\text{B.106})$$

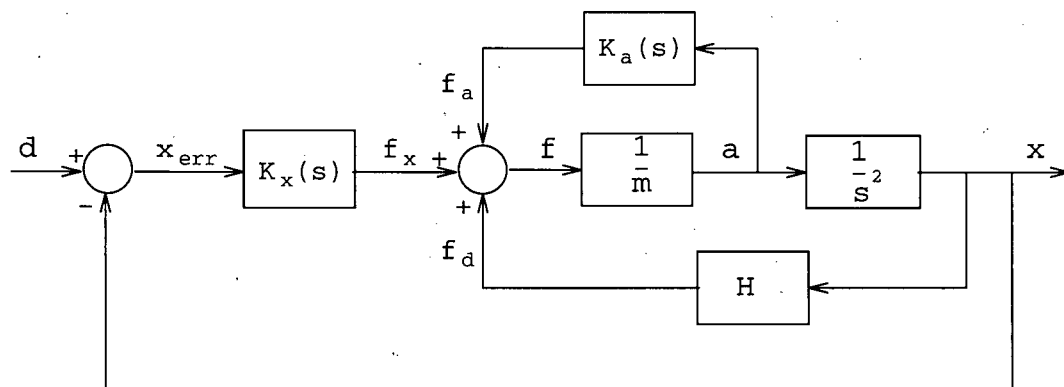


Figure B.45: Closed loop position system with acceleration feedback.

The open loop plants with cascade controller have the same subscripts, but G is replaced with GK .

Sensitivity of Position

$$S_x = \frac{1}{1 + GK_x} \quad (\text{B.107})$$

Sensitivity of Acceleration

$$S_a = \frac{1}{1 - GK_a} \quad (\text{B.108})$$

Sensitivity of Position with Acceleration Feedback

$$S_{xa} = \frac{1}{1 + GK_{xa}} \quad (\text{B.109})$$

Sensitivity of Acceleration with Position Feedback

$$S_{ax} = \frac{1}{1 - GK_{ax}} \quad (\text{B.110})$$

Position Closed Loop

$$T_x = \frac{GK_x}{1 + GK_x} \quad (\text{B.111})$$

Acceleration Closed Loop

$$T_a = \frac{GK_a}{1 - GK_a} \quad (\text{B.112})$$

Position Closed Loop with Acceleration Feedback

$$T_{xa} = \frac{GK_{xa}}{1 + GK_{xa}} \quad (\text{B.113})$$

Acceleration Closed Loop with Position Feedback

$$T_{ax} = \frac{GK_{ax}}{1 - GK_{ax}} \quad (\text{B.114})$$

Other interesting relationships:

$$GK_{xa} = GK_x S_a \quad (\text{B.115})$$

$$GK_{ax} = GK_a S_x \quad (\text{B.116})$$

$$S_{xa} = \frac{1}{1 + GK_x S_a} \quad (\text{B.117})$$

$$S_{ax} = \frac{1}{1 - GK_a S_x} \quad (\text{B.118})$$

$$T_{xa} = T_x S_{ax} \quad (\text{B.119})$$

$$T_{ax} = T_a S_{xa} \quad (\text{B.120})$$

Appendix C

H_∞ Controller Design Code

The following is a listing of the design code for H_∞ control for use with MATLAB.

C.1 Main design file: design.m

```
disp('----- Position Controller -----')
wrad = logspace(-2,3,600);
m = 22;
ok = 'n';
while ok == 'n',
    choice = menu('Choose plant type','Double integrator', ...
        'Positive Feedback','More Accurate Plant','PD Stabilized');
    if choice == 1,
        [agx,bgx,cgx,dgx] = tf2ss(1,[m 0 0]);
    elseif choice == 2,
        H = -40;
        [agx,bgx,cgx,dgx] = tf2ss(1,[m 0 H]);
    elseif (choice == 3) | (choice == 4),
        dnx = conv([1/140,1],[1,2*.15*sqrt(45/2.6),-45/2.6]);
        [agx,bgx,cgx,dgx] = tf2ss(45/1000,dnx);
        if choice == 4,
            [apd,bpd,cpd,dpd] = tf2ss([600 2000],[0.001 1]);
            [agx,bgx,cgx,dgx] = feedback(agx,bgx,cgx,dgx,apd,bpd,cpd,dpd,-1);
        end
    end
    ss_gx = mksys(agx,bgx,cgx,dgx);
    [W1x,W2x,W3x] = weights_x;
    [gamx,ss_kx,ss_Tx,normx] = hinf_bilin(ss_gx,W1x,W2x,W3x);
    [akx,bkx,ckx,dkx] = branch(ss_kx);
    [agkx,bgkx,cgkx,dgkx] = series(akx,bkx,ckx,dkx,agx,bgx,cgx,dgx);
    [atx,btx,ctx,dtx] = cloop(agkx,bgkx,cgkx,dgkx,-1);
    if max(bode(atx,btx,ctx,dtx)) > 1,
        fc(atx,btx,ctx,dtx)
    end
    figure(1)
    jbode(atx,btx,ctx,dtx,1,wrad);
    subplot(211)
    title('Closed Loop Response')
    axis([.01 20 -40 10])
    subplot(212)
    v=axis;
    v(1:2) = [.01 20];
    axis(v)
```

```

    ok = input('Is this satisfactory? ([y]/n): ','s');
end
pltsum(ss_gx,W1x,W3x,ss_kx,gamx)
%-----
disp(''); disp(''); disp(''); disp(''); disp(''); disp(''); disp(''); disp('');
disp('----- Acceleration Controller -----')
[aka,bka,cka,dka] = tf2ss(0,1);
[aga,bga,cga,dga] = tf2ss(0,1);
acc_control = input('Acceleration controller? (y/[n]): ','s');
while acc_control == 'y',
    if choice == 1,
        [ai,bi,ci,di] = tf2ss(1,[1 0 0]);
        [ah,bh,ch,dh] = series(ai,bi,ci,di,akx,bkx,ckx,dkx);
        [aga,bga,cga,dga] = feedback([],[],[],1/m,ah,bh,ch,dh,-1);
    elseif choice == 2,
        [ah,bh,ch,dh] = parallel([],[],[],H,akx,bkx,-ckx,-dkx);
        [ah,bh,ch,dh] = series([0 0;1 0],[1;0],[0 1],[0],ah,bh,ch,dh);
        [aga,bga,cga,dga] = feedback([],[],[],1/m,ah,bh,ch,dh,+1);
    elseif (choice == 3) | (choice == 4),
        [nmf,dnf] = butter(4,325,'s');
        [nmg,dng] = series([45/2.6 0 0],dnx,nmf,dnf);
        [aga,bga,cga,dga] = tf2ss(nmg,dng);
    end
    ss_ga = mksys(aga,bga,cga,dga);
    [W1a,W2a,W3a] = weights_a;
    [gamma,ss_ka,ss-Ta,norma] = hinf_bilin(ss_ga,W1a,W2a,W3a);
    % Acceleration system
    [aka,bka,cka,dka] = branch(ss_ka);
    [agka,bgka,cgka,dgka] = series(aka,bka,cka,dka,aga,bga,cga,dga);
    [ata,bta,cta,dta] = cloop(agka,bgka,cgka,dgka,+1);
    [as,bs,cs,ds] = feedback([],[],[],1,agka,bgka,cgka,dgka,+1);
    % Complete system
    if choice == 1,
        ag = [0 0;1 0]; bg = [1/m;0]; cg = [0 1;0 0]; dg = [0;1/m];
    elseif choice == 2,
        [ag,bg,cg,dg] = tf2ss(1,[m 0 -H]);
        cg = [cg ; H/m*cg];
        dg = [dg ; 1/m];
    elseif choice == 3,
        [ax,bx,cx,dx] = tf2ss(45/1000,[1,2*.15*sqrt(45/2.6),-45/2.6]);
        [a1,b1,c1,d1] = tf2ss(1,[1/140 1]);
        [a2,b2,c2,d2] = tf2ss([1 0 0]*nmf(5),dnf);
        [ag,bg,cg,dg] = append(a1,b1,c1,d1,a2,b2,c2,d2);
        bg = [b1;b2]; dg = [d1;d2];
        [ag,bg,cg,dg] = series(ax,bx,cx,dx,ag,bg,cg,dg);
    end
    ss_g = mksys(ag,bg,cg,dg);
    [ak,bk] = append(akx,bkx,ckx,dkx,aka,bka,cka,dka);
    ck = [ ckx cka ];
    dk = [ dkx dka ];
    ss_k = mksys(ak,bk,ck,dk);
    [agk,bgk,cgk,dgk] = series(ak,bk,ck,dk,ag,bg,cg,dg);
    [al,bl,cl,d1] = feedback(agk,bgk,cgk,dgk,[],[],[],[-1 0;0 1],+1);
    figure(2)
    jbode(al,bl,cl,d1,1,wrad);
    subplot(211)

```

```

title('Closed Loop Response')
axis([.01 20 -40 20])
subplot(212)
v=axis;
v(1:2) = [.01 20];
axis(v)

acc_control = input('Would you like to try again? (y/[n]): ','s');
end

```

C.2 Position weight generation: weights_x.m

```

function [W1, W2, W3] = weights
% Setup for robust controller design
% Defines weights only. Sets it up for position only design.
% Robustness Spec (W3)
disp('W3 controls the robustness spec of the system')
bw = input('Enter bandwidth (Hz) of the closed loop position system: ');
bw = 2*pi*bw;
wc = bw;
slope = input('Enter slope (ie: -1 for -20dB/decade, -2 for -40dB/decade): ');
crossover = 10^(-slope*log10(wc));
num = [1];
den = [crossover];
for k = 1:-slope,
    num = conv(num,[1, 0]);
end
if (slope < -2),
    for k = 3:-slope,
        den = conv(den,[1/wc/10^(2) 1]);
    end
end
[r,c] = size(num);
[x,r] = size(den);
den = [ zeros(1,c-r), den ];
W3 = [ num ; den ];

% Disturbance rejection (W1)
disp('-----')
disp('W1 affects the sensitivity function')
disp('The DC gain affects the low frequency response of T(s). A too low value')
disp('will cause early roll off. A too high value will create resonant peaks.')
disp('The HF gain, if small enough (<.1) has little effect on the system.')
DC = input('DC gain: ');
HF = input('HF gain: '); % High frequency gain
wc = 0.5*bw; % filter crossover frequency
d1 = 0.7; % damping ratio 1
num = DC*[HF 2*d1*wc*sqrt(HF) wc^2] ;
den = [DC 2*d1*wc*sqrt(DC) wc^2] ;
if 0, % Fourth order W1
    num = conv(num,num);
    den = conv(den,den);
end
W1 = [ num ; den ];
W2 = [1.e-4 ; 1]; % Small to fulfill rank requirements on complex plants

```

C.3 Acceleration weight generation: weights_a.m

```

function [W1, W2, W3] = weights_a
% [W1, W2, W3] = weights_a
%
% Weights for acceleration only controller.

disp('The bandwidth for the acceleration control is band pass. ');
wc1 = input('Please enter the low frequency crossover (Hz): ');
wc1 = 2*pi*wc1;
wc2 = input('Please enter the high frequency crossover (Hz): ');
wc2 = 2*pi*wc2;
d1 = input('Damping ratio 1: ');
d2 = input('Damping ratio 2: ');
ord = input('Input slope/order of performance spec (see notes): ');
c1 = 2/3*wc1; c2 = 3/2*wc2;

den = conv([1/4/wc1 1],[1/0.25/wc2 1]);
den = conv(den,den);
num = [1/wc1 0];
num = conv(num,num);
W1 = [ 0 0 num ; den ];

num = conv([1/2/c1 1],[1/0.25/c2 1]);
num = conv(num,[1/2/c1 1]);
den = [1/c1 0];
den = conv(den,den);
den = conv(den,[1/10/c2 1]);
W3 = [ num ; den ];

W2 = [1.e-4 ; 1];

W1 = [0 5 0.9 ; 0.05 0.6 1];
W3 = [0.0500 1.0500 1.0000; 0.0100 10.0001 0.1000];

```

C.4 Bilinear transform: hinf_bilin.m

```

function [gam, ss_k, ss_Tzw, norm_Tzw] = hinf_bilin(ss_g,W1,W2,W3);
% [gam, ss_k, ss_Tzw, normhinf] = hinf_bilin(ss_g,W1,W2,W3);
%
% Bilinear transform H-infinity design
%      az + d
% s = -----
%      cz + b
%
% Plant independant
% Requires
%   Plant --> (ss_g)
%   Weights --> W1, W2, W3 as for use in augtf.m
% Calculates
%   Augmented plant (with gam*W) --> Tss
%   Gamma --> gam
%   Controller --> (ak,bk,ck,dk) or ss_k
%   Tzw loop --> (acl,bcl,ccl,dcl) or ss_Tzw

[ag,bg,cg,dg] = branch(ss_g);
[nW1,q] = size(W1); nW1 = nW1/2;
% Assign values
a = 1; % Axis scaling

```

```

b = 1;          %
c = 0.0;       % 1/p2
d = -0.1;     % Dominant pole placement

% Augment plant
Tss = augtf(ss_g,W1,W2,W3);

% Bunch of stuff to be done for transform on augmented plant
[a1,b1,b2,c1,c2,d11,d12,d21,d22]=branch(Tss);
[q,ni] = size(b2);
[no,q] = size(c2);
[a1,b1,c1,d1]=bilin(a1,[b1,b2],[c1;c2],[d11,d12;d21,d22],1,'G_Bili',[a,b,c,d]);
Tss = msys(a1,b1,c1,d1,ni,no);

% Do robust design
[ss_k,ss_Tzw] = hinf(Tss); gam = 1;
[gam,ss_k,ss_Tzw] = hinfopt(Tss,[1 3]); %,1:nW1);

% Compute controller and do inverse transform
ss_k = bilin(ss_k,-1,'G_Bili',[a,b,c,d]);

% Compute Tzw and do inverse transform
ss_Tzw = bilin(ss_Tzw,-1,'G_Bili',[a,b,c,d]);
norm_Tzw = normhinf(ss_Tzw);

```

C.5 State space system: msys.m

```

function tss_p = msys(ap,bp,cp,dp,u,y)
% Changes the state space representation of a plant into one for the hinf
% routine in Matlab. (Standard State-space to Two-port State-space)
%
% tss_p = msys(ap,bp,cp,dp,ni,no)
%       where ni = number of control inputs (size of u)
%       no = number of control outputs (size of y)
[n,m]=size(dp);
a = ap;
b1 = bp(:,1:m-u);
b2 = bp(:,m-u+1:m);
c1 = cp(1:n-y,:);
c2 = cp(n-y+1:n,:);
d11 = dp(1:n-y,1:m-u);
d12 = dp(1:n-y,m-u+1:m);
d21 = dp(n-y+1:n,1:m-u);
d22 = dp(n-y+1:n,m-u+1:m);
tss_p = mksys(a,b1,b2,c1,c2,d11,d12,d21,d22,'tss');

```

C.6 Plotting summary: pltsum.m

```

function pltsum(ss_g,W1,W3,ss_k,gam)
% pltsum(ss_g,W1,W3,ss_k,gam)
%
% Summary plotting routine
%
[ag,bg,cg,dg] = branch(ss_g);

```

```

[ak,bk,ck,dk] = branch(ss_k);
[agk,bgk,cgk,dgk] = series(ak,bk,ck,dk,ag,bg,cg,dg);
[as,bs,cs,ds] = feedbk(agk,bgk,cgk,dgk,1);
[at,bt,ct,dt] = cloop(agk,bgk,cgk,dgk,-1);
wrad = logspace(-1.5,2,800);
figure
subplot(221)
[mag1,phi1] = bode(ak,bk,ck,dk,1,wrad);
semilogx(wrad/2/pi,20*log10(mag1));
xlabel('Frequency [Hz]')
title('Controller')
ylabel('|K| [dB]')
v=axis;
v(1:2)=[.01 20];
axis(v);
grid
subplot(222)
semilogx(wrad/2/pi,phi1);
title('Controller')
xlabel('Frequency [Hz]')
ylabel('Angle(K) [deg]')
v = axis;
v(1) = 0.01; v(2) = 20;
axis(v)
ytick = get(gca, 'ytick');
ylim = get(gca, 'ylim');
yrange = ylim(2) - ylim(1);
no_of_pts = log(yrange/(length(ytick)*90))/log(2);
n = round(log(yrange/(length(ytick)*90))/log(2));
set(gca, 'ylimmode', 'manual')
if no_of_pts >= -1.15
    % 45, 90, 180, 360, ... degree increments
    ytick = [-90*2^n:-(90*2^n):ylim(1), 0:(90*2^n):ylim(2)];
    ytick = ytick(find(ytick >= ylim(1) & ytick <= ylim(2)));
    set(gca, 'ytick', ytick);
elseif n >= -2
    % Special case for 30 degree increments rather than 22.5
    ytick = [-30:-30:ylim(1), 0:30:ylim(2)];
    ytick = ytick(find(ytick >= ylim(1) & ytick <= ylim(2)));
    set(gca, 'ytick', ytick);
end
grid
subplot(223)
mag2 = bode(as,bs,cs,ds,1,wrad);
mag3 = bode(W1(2,:),gam*W1(1,:),wrad);
semilogx(wrad/2/pi,20*log10(mag2),wrad/2/pi,20*log10(mag3),'-.')
axis([.01 20 -60 20])
grid
title('Sensitivity and Weight')
xlabel('Frequency [Hz]')
ylabel('Magnitude [dB]')
legend('|S|', '|1/Ws|')
subplot(224)
mag4 = bode(at,bt,ct,dt,1,wrad);
mag5 = bode(W3(2,:),gam*W3(1,:),wrad);
semilogx(wrad/2/pi,20*log10(mag4),wrad/2/pi,20*log10(mag5),'-.')
axis([.01 20 -60 20])

```

```
grid .
title('Complementary Sensitivity and Weight')
xlabel('Frequency [Hz]')
ylabel('Magnitude [dB]')
legend('|T|', '|1/Wt|')
set(gcf, 'PaperPosition', [1 2 6 7])
```

Appendix D

Coarse-Fine Tracker Software Particulars

The software was developed by Tim Salcudean and Chia-Tung Chen.

D.1 Coarse-Fine Software Algorithm

The controller code and the include files are compiled and linked with a C30 compiler. The control code is executed every time the DSP has a specific interrupt set, causing the following functions to execute:

1. getAD
2. psd_position, measure_accel, measure_coarse_pos
3. determine_state
4. coarse_control
5. flotor_control
6. force_to_current, current_to_volt
7. putDA

In short, the code reads in the signal data and calculates relevant position, velocity, and acceleration variables, calculates the control signals required to drive the system, and outputs these signals. The above is explained in greater detail now.

1. The raw data available at the A/D port is read in and stored.
2. The raw data is manipulated through algebra and matrix multiplication to get the position and orientation of the flotor, the acceleration levels of the flotor, stator, and plane, and the coarse position.
3. The type of control to be used is dependent on the state of the system. There are five states: READY, ISOLATE, CATCH, LOWER, and REST. The state the system is in depends on the plane acceleration and coarse position. Figure D.46 shows the state switching diagram which can be summarized as follows:

READY Magnitude of the acceleration of plane less than MAXLEV but greater than MAXISO.

ISOLATE Magnitude of the acceleration of plane less than MAXISO.

CATCH Coarse position in ISOLATE nears the end of the rail.

LOWER Acceleration of plane less than -MAXLEV and coarse position not at minimum.

REST Acceleration of plane less than -MAXLEV and coarse position at minimum.

MAXLEV is the maximum acceleration allowed to keep the coarse stage centered on the rail, while MAXISO is the maximum acceleration allowed during the vibration isolation and tracking phase.

4. The control of the coarse position is dependent on the State of the system. The coarse control signal, u_{crse} , is an integer between ± 500 that gets converted to a voltage to the current amp. See Appendix D for the control relationships.
5. The flotor is controlled by a simple PID,

$$f = k_p x_{err} + k_i \int x_{err} + k_d \dot{x}_{err} \quad (D.121)$$

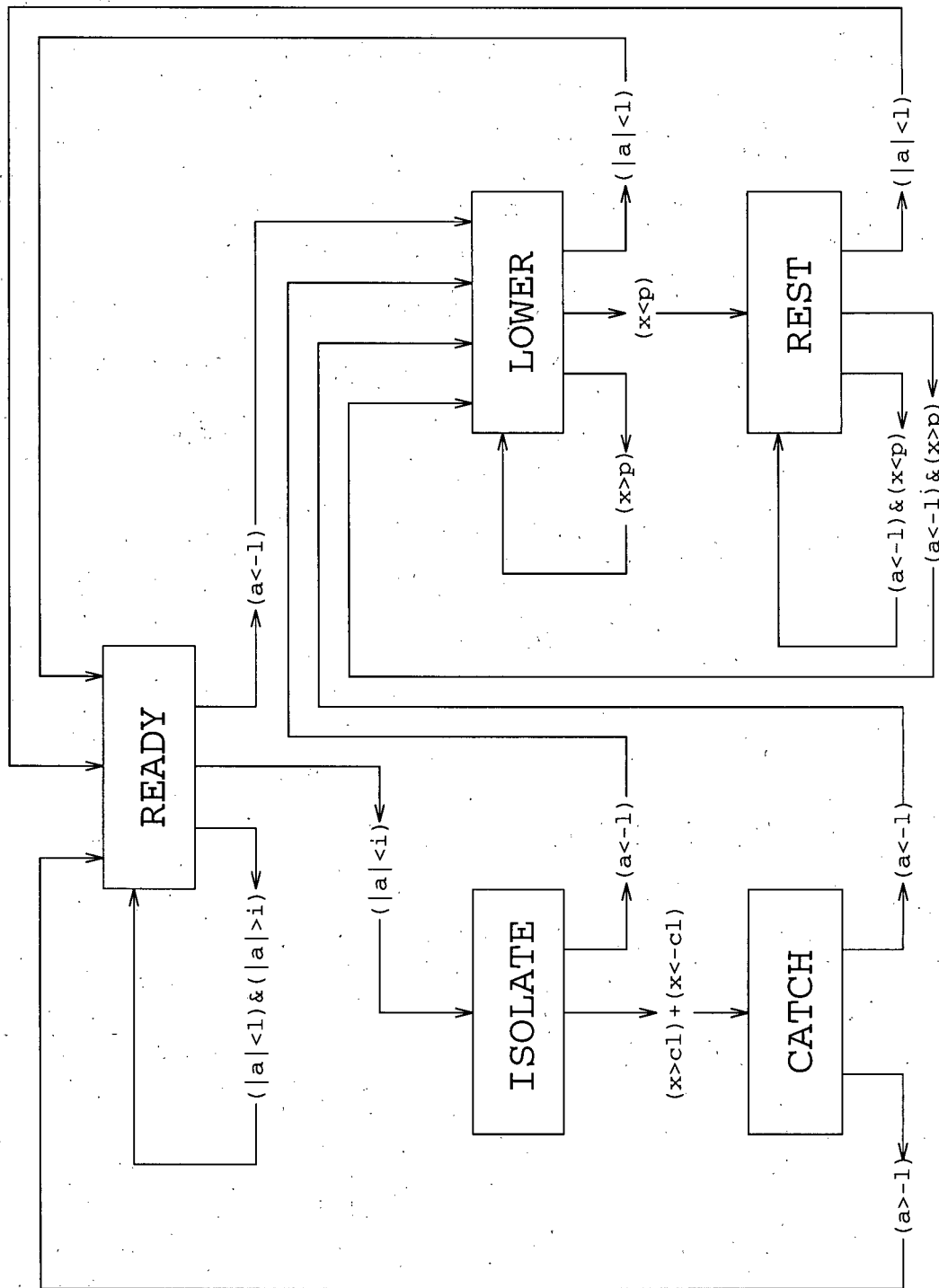


Figure D.46: State switching algorithm. x is the coarse position, a is the acceleration of the plane, i is MAXISO, l is MAXLEV, p is the lower limit of the I-beam, and cl is the coarse position limits during operation.

where $x_{err} = x_{ref} - x_{fine}$.

6. The force just calculated is transformed first into a current, then a voltage.
7. The voltages for the coarse control and flotor control are put to the D/A converter for use by the system.

D.2 Coarse Stage Control Signal

READY $u_{crse} = kp_{crse_rdy} * (CRSE_DB - x_{crse_err}) - kv_{crse} * v_{crse_f}$

This centers the coarse stage on the rail.

ISOLATE $u_{crse} = kp_{crse_iso} * x_{fine} - kv_{crse} * v_{crse_f}$

The coarse stage is driven to follow the displacement of the flotor with velocity damping.

CATCH $u_{crse} = 0$

Stops the motion toward the rail limits.

LOWER $u_{crse} = kv_{crse} * (PARK_VEL - v_{crse_f})$

Lowers the coarse stage to the bottom of the rail.

REST $u_{crse} = -70$

Constant negative force to keep the coarse stage at the bottom of the rail.

D.3 Coarse Stage Code Variables

All position variables have units mm and velocity variables mm/s.

kp_{crse_rdy} Proportional constant for coarse control in State READY.

CRSE_DB Minimum displacement of coarse position (dead band) from center before control is started.

x_crse Coarse position.

crse_cen Set point for centering the coarse stage.

$$x_{crse_err} = x_{crse} - crse_cen$$

kv_crse Derivative constant for the coarse position.

v_crse_f Velocity of coarse position, filtered.

kp_crse_iso Proportional constant for coarse control in State ISOLATE.

x_fine Position of flotor as measured by the PSD's.

PARK_VEL Maximum velocity when lowering the coarse stage.

k_p Proportional constant for flotor control in N.mm.

$$k_p = 4\pi^2 f_n^2 * mass_{flotor} / 1000$$

k_i Integral constant for flotor control, equal to 0.1 N/s/mm arbitrarily.

k_d Derivative constant for flotor control in N.s/mm.

$$k_d = 4\pi\zeta f_n * mass_{flotor} / 1000$$

f_n Desired bandwidth of fine motion system in Hz.

ζ Desired damping ratio of fine motion system.

Appendix E

Data Plots

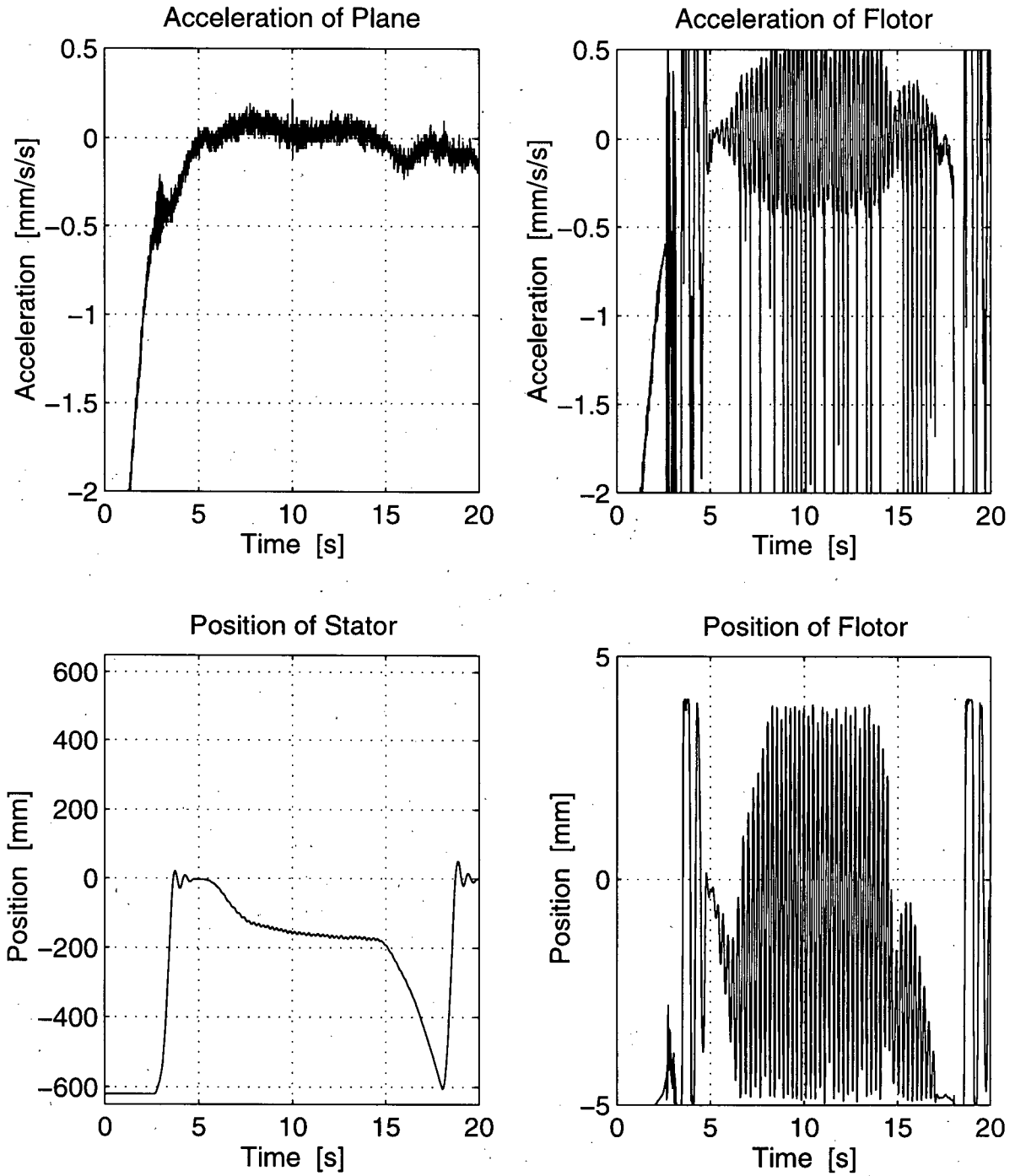


Figure E.47: Data plots for control when the dead band was not removed. It is possible to see the coarse stage vibrations in the Position of Stator plot. $k_{p_crse_iso} = 80$, $k_{v_crse} = 1$, $f_n = 0.2$.

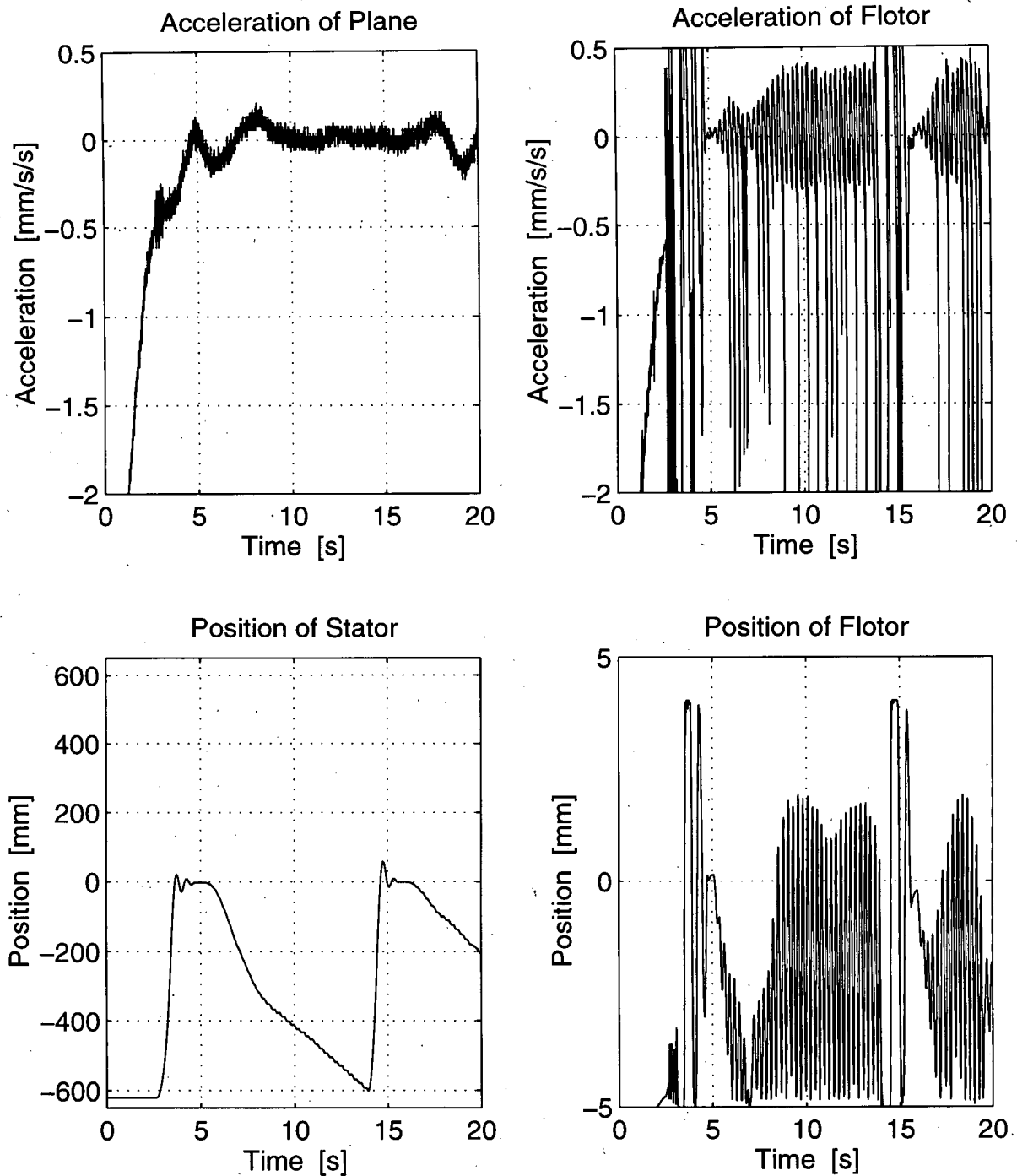


Figure E.48: Data plots for control when the dead band was not removed. It is possible to see the coarse stage vibrations in the Position of Stator plot. $k_{p_crse_iso} = 80$, $k_{v_crse} = 1$, $f_n = 0.2$.

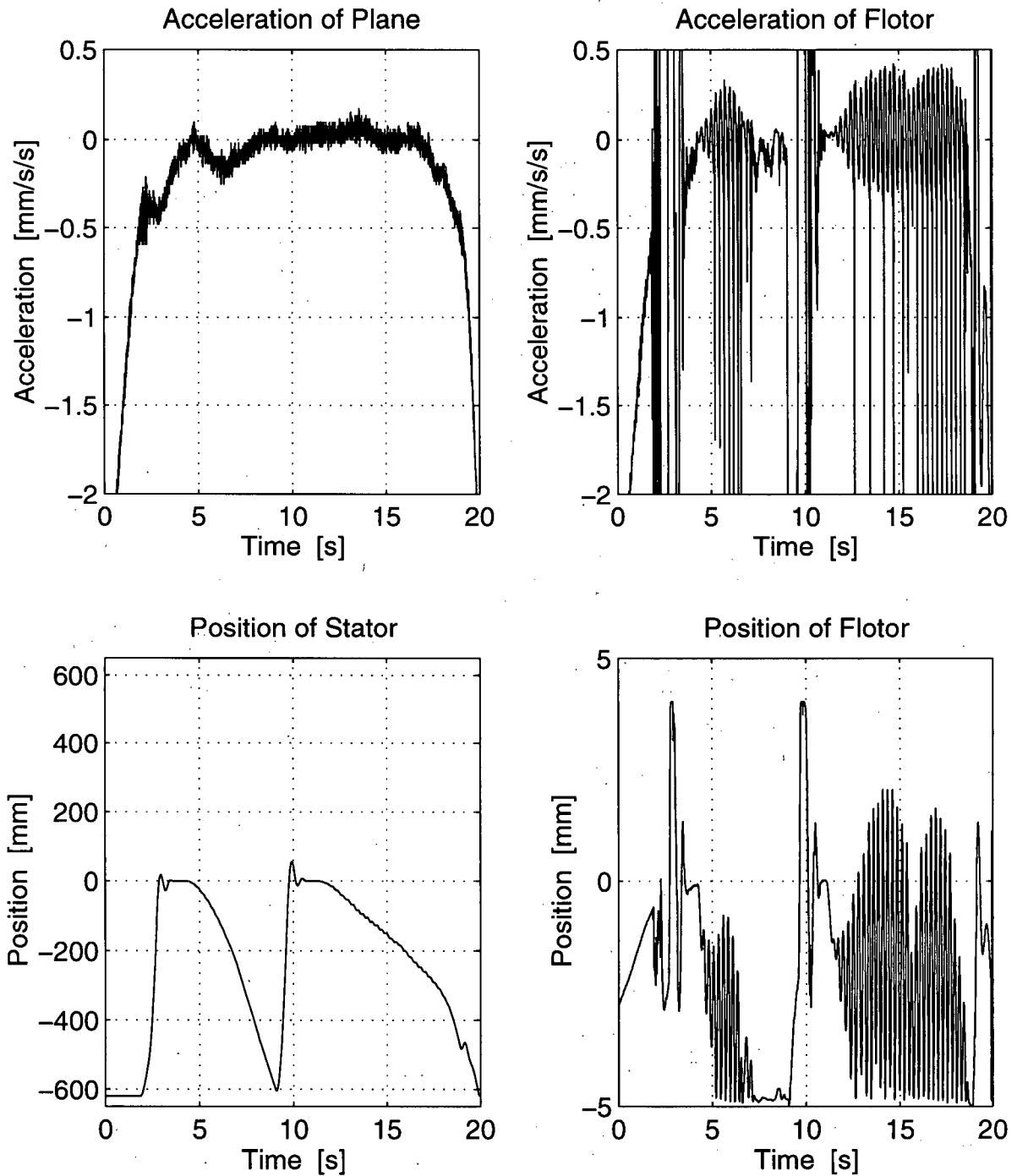


Figure E.49: Data plots for control when the dead band was not removed. It is possible to see the coarse stage vibrations in the Position of Stator plot. $kp_{crse_iso} = 80$, $kv_{crse} = 1$, $f_n = 0.2$.

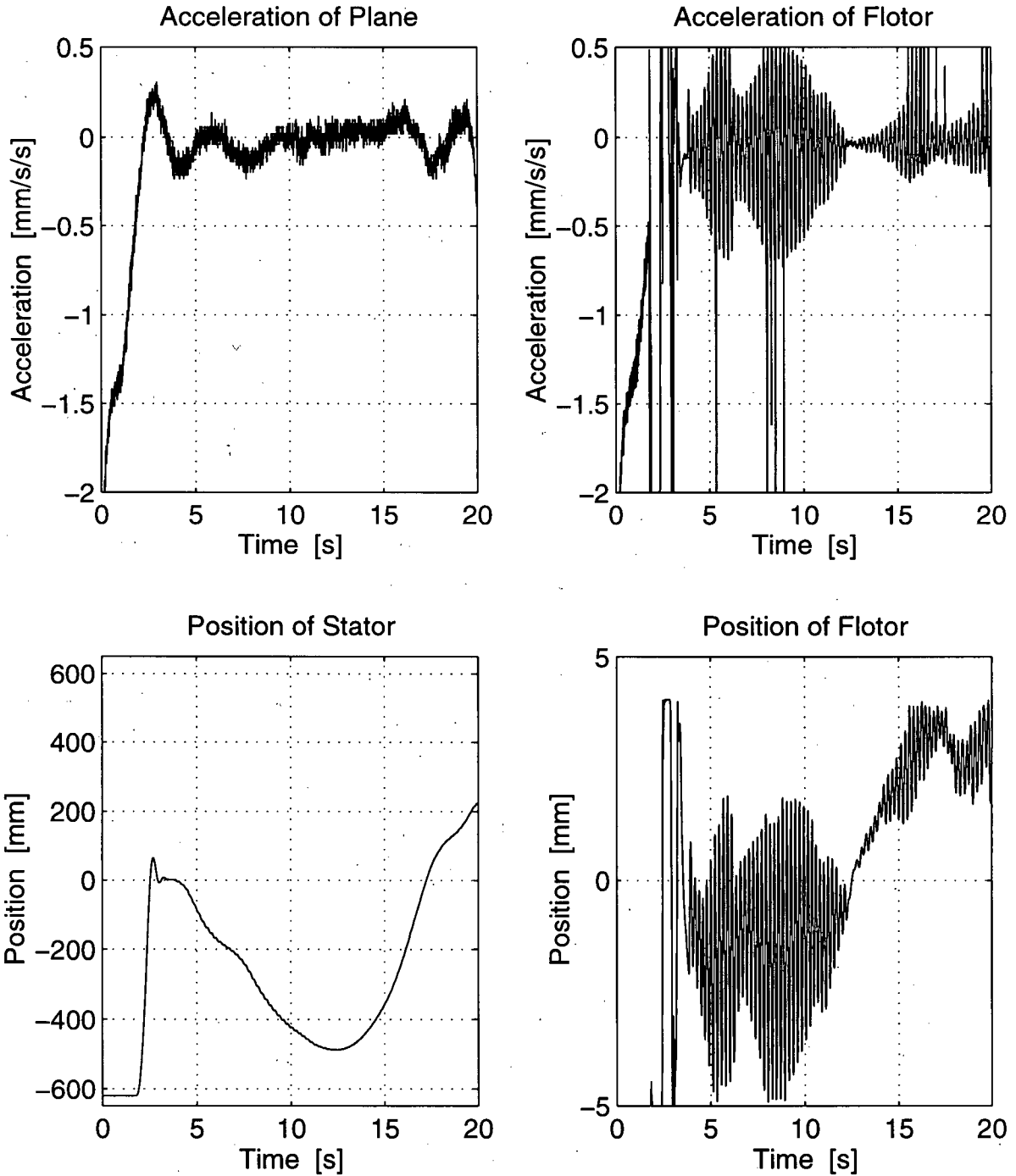


Figure E.50: Data plots for control with no dead band but with a velocity variable causing vibrations. Less coarse stage noise is seen in Position of Stator plot but acceleration of flotor remains poor. $k_p_{crse_iso} = 80$, $k_v_{crse} = 1$, $f_n = 0.2$.

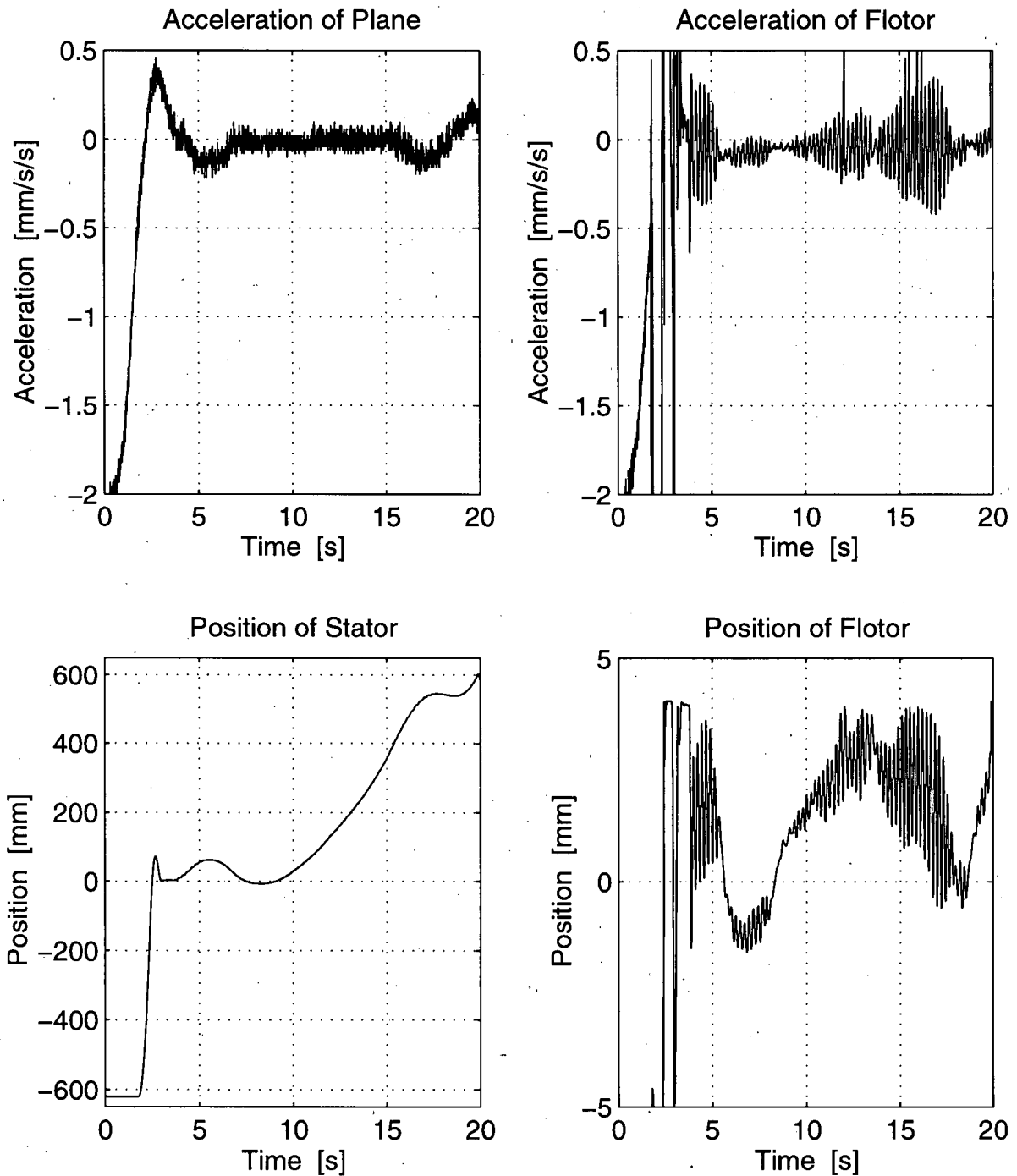


Figure E.51: Data plots for control with no dead band but with a velocity variable causing vibrations. Less coarse stage noise is seen in Position of Stator plot but acceleration of flotor remains poor. $kp_{crse_iso} = 80$, $kv_{crse} = 1$, $f_n = 0.2$.

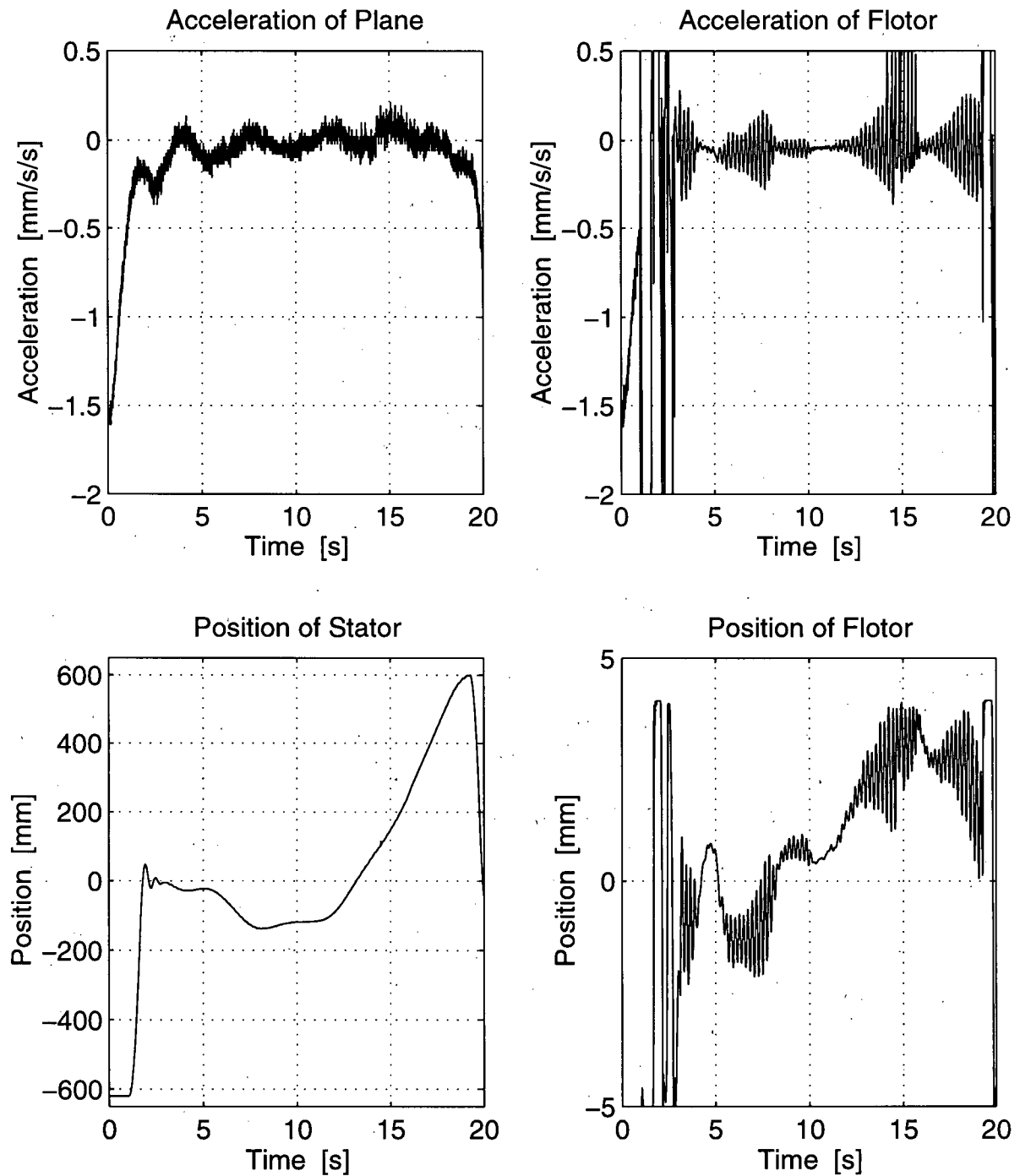


Figure E.52: Data plots for control with no dead band but with a velocity variable causing vibrations. Less coarse stage noise is seen in Position of Stator plot but acceleration of flotor remains poor. $kp_crse_iso = 80$, $kv_crse = 1$, $f_n = 0.2$.

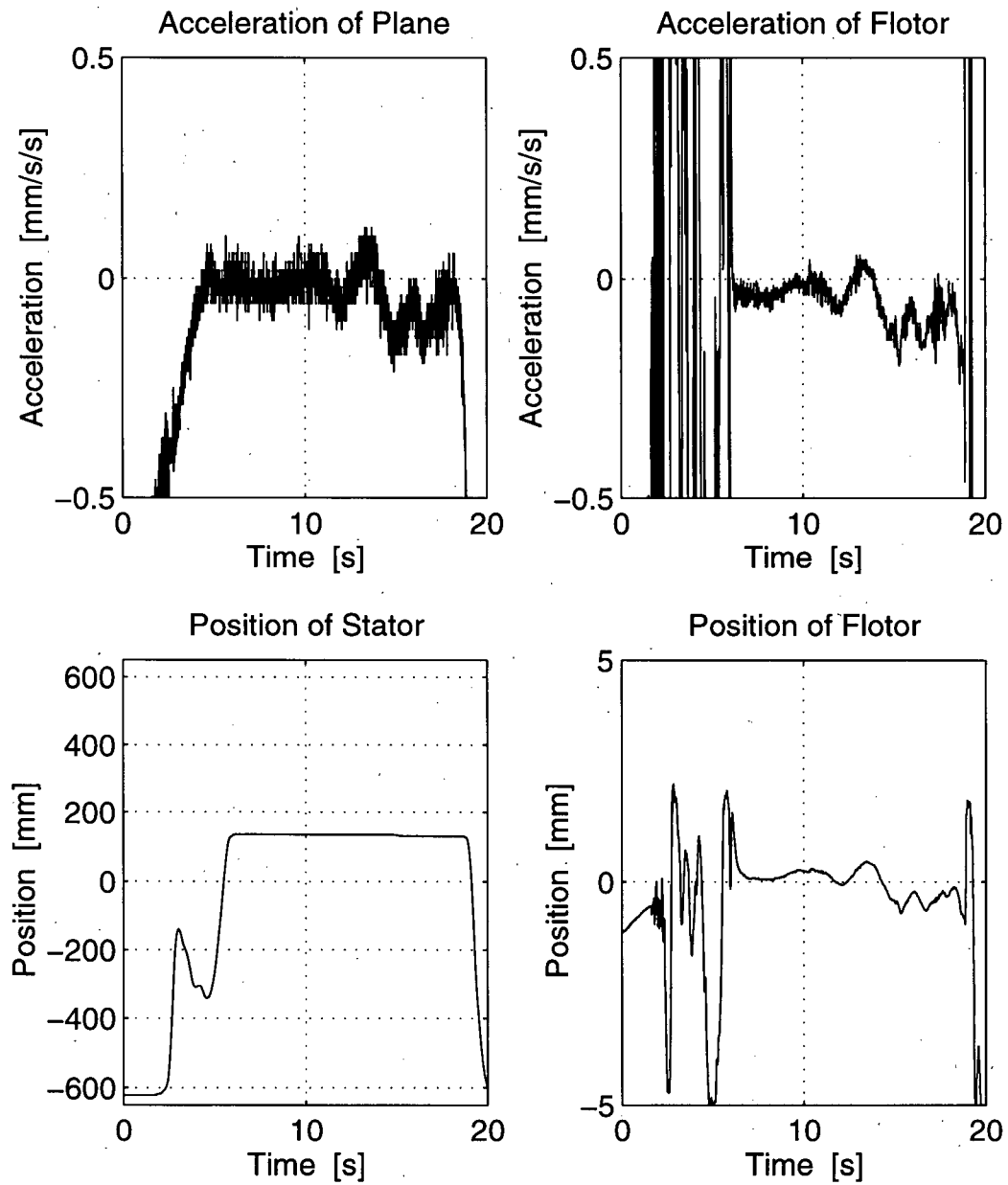


Figure E.53: Data plots for unreliable data obtained when the system was not working properly. There is no velocity damping in ISOLATE state and the acceleration of the flotor is considerably improved. Notice the position of the flotor at the start of the parabola while coarse stage centering is attempted. $kp_crse_iso = 50$, $f_n = 0.1$

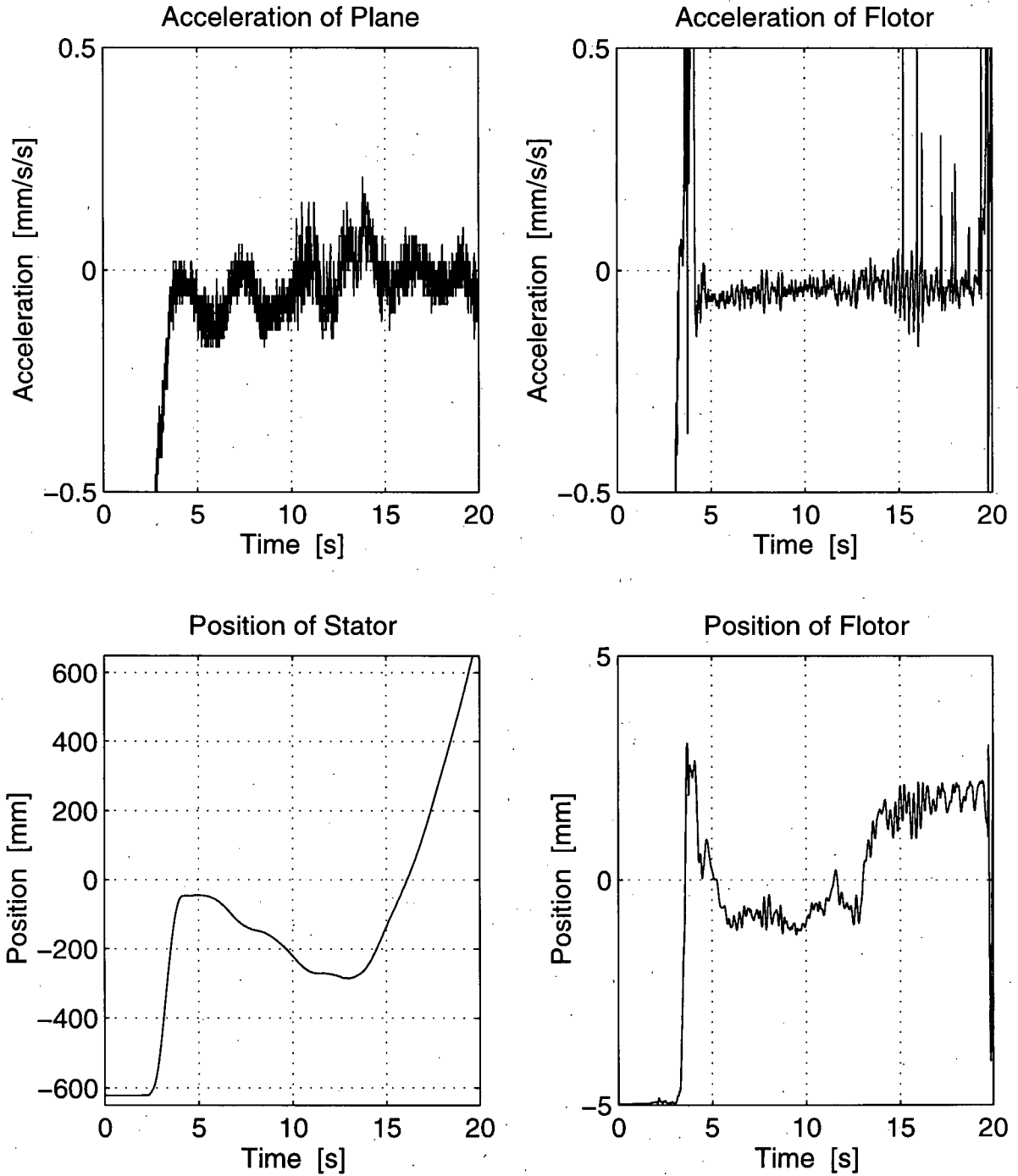


Figure E.54: Data plots for unreliable data obtained when the system was not working properly. There is no velocity damping in ISOLATE state and the acceleration of the flotor is considerably improved. $k_{p_crse_iso} = 50$, $f_n = 0.1$